Applied Physics A (2023) 129:14
https://doi.org/10.1007/s00339-022-06229-x

Applied Physics A
Materials Science & Processing

S.I. : 50TH ANNIVERSARY OF APPLIED PHYSICS

Structuring of thin films by ultrashort laser pulses

Jörn Bonse[1] · **Jörg Krüger**[1]

Received: 27 September 2022 / Accepted: 7 November 2022 / Published online: 8 December 2022

Abstract
Modern life and global communication would not be possible without technologically tailored thin films; they are omnipresent in daily life applications. In most cases, the films are deposited entirely at the carrying substrates in a specific processing step of the device or sample. In some cases, however, removal or modification must be performed locally, i.e., site-controlled and material selective through an additional laser processing step. For that ultrashort laser pulses with durations in the femtosecond and picosecond range can provide unique advantages and capabilities in industrially scalable schemes. This article reviews the current state of the research and corresponding industrial transfer related to the structuring of thin films by ultrashort pulsed lasers. It focuses on the pertinent historic developments, reveals the relevant physical and chemical effects, explores the ultimate limits, and discusses selected industrial and scientific applications.

Keywords Thin films · Laser processing · Ultrashort lasers · Laser damage · Femtosecond laser ablation · Laser-induced forward transfer (LIFT) · Laser-induced periodic surface structures (LIPSS) · Laser cleaning · Photomask repair · Depth-profiling · Incubation effects · Optical coatings · Nonlinear absorption · Material science · Multi-layer · Single-layer

1 Introduction

The structuring of thin films is of paramount importance for many daily life applications, where a local post-processing of functional coatings is required to adapt, adjust or improve their contour to the demands of the devices 2D- or 3D-geometry. Such coatings can enable or control optical, electrical, or mechanical surface properties for applications in semiconductor electronics, the field of renewable energy, friction and wear management, or for surface decoration or protection. Moreover, the laser-induced "structuring" can involve either complete film removal or the modification of its intrinsic structural or electronic state [1]. For all this, laser-processing offers a simple, fast, and reliable technology that allows to re-shape, modify, and tailor even very thin, extremely soft, hard, or brittle film materials in a clean and contactless manner, while featuring lateral and vertical machining precision in the sub-micrometer scale [2, 3].

On the other hands, thin films are the backbone for many optical applications in fields of optical devices, photovoltaics, and modern laser technology. Here, particularly the development of damage resistant optical coatings with anti- or high-reflective performance is desired [4]. For optimizing these optical coatings, a deep understanding of the manifold linear and nonlinear interaction mechanisms of optical radiation with matter as well as a profound knowledge of the materials solid state physics and chemistry is desired.

In this review article, we present an up-to-date literature overview on the laser processing of thin films. In most cases, the focus is laid on single film layers and the treatment by single or multiple ultrashort laser pulses with durations in the picosecond (ps) and femtosecond (fs) range. For that, the particularities of laser-matter interactions in the presence of additional film- or substrate interfaces are pointed out, the impact of intrinsic optical or adhesional mechanical film properties are revealed, and relevant applications are discussed. Since the literature published in this field over decades is already very exhaustive, our article aims to focus on the groundbreaking early publications, while simultaneously shedding some more light on specific, less known aspects in ultrashort laser processing and their historic development. To aid the reader selecting suitable laser processing conditions, special emphasis will be given to the discussion and

✉ Jörn Bonse
joern.bonse@bam.de

✉ Jörg Krüger
joerg.krueger@bam.de

[1] Bundesanstalt für Materialforschung und -prüfung (BAM), Unter den Eichen 87, 12205 Berlin, Germany

consideration of the intrinsic influence of the film material (metallic, semiconducting, dielectric), the film thickness (in relation to the wavelength and focusing depth), and the physical properties of the substrate material (optical reflectivity, heat conductivity, thermal expansion, etc.).

The article is organized as follows: Sect. 2 briefly recalls the benefits of ultrashort laser pulses (ULP) in material processing. In Sect. 3, the ULP laser structuring is discussed, including possible processing geometries (3.1), interaction mechanisms with films made of metals, semiconductors, or dielectrics (3.2), and relevant transient effects along with their time scales and with a focus on important differences between thin and thick films (3.3). Following the historic developments in the field, Sect. 4 presents selected industrial and scientific applications of ULP processing of single-layers and multi-layer film systems, including photolithographic mask repair (4.1), laser cleaning aspects (4.2), avoiding laser-damage of optical coatings (4.3), laser-printing through laser-induced forward transfer (4.4), and thin-film depth-profiling analyzes for material sciences (4.5). Section 5 provides a brief summary along with an outlook to future developments.

2 Implications of ultrashort laser pulses for materials processing

Before discussing the specifics of thin film processing with ultrashort laser pulses in the following sections, the advantages and implications of using ultrashort laser pulses for materials processing should be briefly reviewed. While the literature on that topic is already mature and very exhaustive, we try to break this down to a few key aspects only. For additional details, the reader is referred to some books and review articles here [1, 6–16].

- Since the pulse duration is small compared to the typical *electron–phonon interaction times* ($\tau_{e\text{-}ph}$), heat diffusion into the material is insignificant during the time scale of the laser pulse [1].
- The extremely rapid energy deposition leads to a high local confinement of the laser pulse energy resulting in reduced threshold fluences of melting and ablation when compared to longer pulse durations.
- The strong energy confinement results in a small *heat affected zone* (HAZ, extent typically ≤ 100 nm [17]) and consequently in a high lateral and vertical machining precision. Compared to the ns-pulse irradiation, the minimal achievable ablation depth per pulse is reduced. Significant smaller features with sizes even below the beam diameter can be generated.
- Nearly every material (metals, semiconductors, ceramics, polymers, dielectrics, and composite materials) can be ablated successfully by employing intensities between 10^{12} and 10^{14} W/cm^2 which are easily obtained for fs-laser pulse durations.
- For all materials, a distinct *damage threshold*, i.e., the minimum fluence F_{th} (areal energy density in J/cm^2) can be observed above which a *permanent material modification* (structural, chemical, or ablative) can be induced upon laser irradiation. For bulk materials, such thresholds are often ruled by specific thermodynamic mechanisms, such as melting, ablation, or oxidation [18–20]. For dielectrics irradiated by femtosecond laser pulses, the damage threshold is more deterministic compared to longer laser pulses since the electrons seeding the avalanche dielectric breakdown are generated by the pulse itself [5, 6]. For dielectrics and semiconductors damage is then initiated when a critical carrier density of the order of 10^{21} cm^{-3} in the conduction band is exceeded.
- For a single-pulse irradiation event, the formation of the ablation plasma occurs *after* the ultrashort laser pulse, i.e., temporally separated from the intra-pulse absorption of the energy in the solid [8, 21, 22]. Due to the lack of plasma-shielding (for low repetition rate laser pulse trains) the ablation rates are less dependent on the focusing conditions (spot size) and the laser pulse energy can be used more efficiently.
- Femtosecond laser pulse irradiation in the ablative regime can lead to a very rapid (<50 ps) disintegration of the excited ablating material into nanometer-sized fragments [23, 24].
- In most materials, two different regimes of *"gentle ablation"* (for fluences below a few J/cm^2) and *"strong ablation"* (for fluences above several J/cm^2) have been observed [25, 26]. For dielectrics and semiconductors *Coulomb-explosion* [27, 28] accounts for the gentle ablation regime, while for all materials the thermodynamic *phase-explosion* [29–32] has been discussed.
- In comparison with longer pulse durations ($\tau \geq$ ns), the expulsion of material and the amount of redeposited material in the surrounding of the irradiated zone is generally reduced.

Particularly the small HAZ along with the reduced threshold fluence and increased ablation precision make ultrashort laser pulses potentially interesting for the processing of thin films. However, care must be taken to avoid or reduce thermal heat-accumulation effects that may destroy the benefits of ultrashort pulse durations at (too) high laser pulse repetition rates exceeding several tens to hundreds of kilohertz.

3 Single-layer structuring

3.1 Processing geometries

The laser-processing of thin films is performed either in the *substrate geometry*, where the laser beam is focused by a suitable optical element (lens, mirror, axicon, diffractive optical element) directly onto the surface of the film that was previously deposited on a carrier substrate or in the *superstrate geometry* where the laser beam is focused through the transparent substrate into the film/carrier interface (Fig. 1).

In the *substrate geometry* (Fig. 1a), the ablation products (atoms, ions, molecules, clusters, nano- and microparticles, fragments) and the incident laser beam are counter-propagating at the same half-space, that my cause detrimental effects such as *plasma-shielding* for long pulse durations [21, 33] or at high laser pulse repetition rates [34]. Moreover, the ablated material can be partly redeposited as debris at the film surface in regions later accessed by the laser-processing.

In the *superstrate geometry* (Fig. 1b), such interactions with the debris can be avoided since the film/carrier-interface is neatly protected from debris through the film itself. Also, plasma-shielding does not occur since the incident laser beam and the ablated material are spatially separated completely through the film. On the other hand, the laser processing in this geometry is only possible for carrier materials being transparent for the laser wavelength. Additional difficulties may arise for ultrashort high-intensity laser pulses, where transient defocusing, self-focusing, or beam-filamentation through nonlinear beam propagation effects (such as the Kerr-effect) can antagonize against a defined localized confinement of the optical energy in the film/carrier-interface region—finally preventing a controlled laser processing then. Thus, the *superstrate geometry* may not be accessible in all laser processing cases.

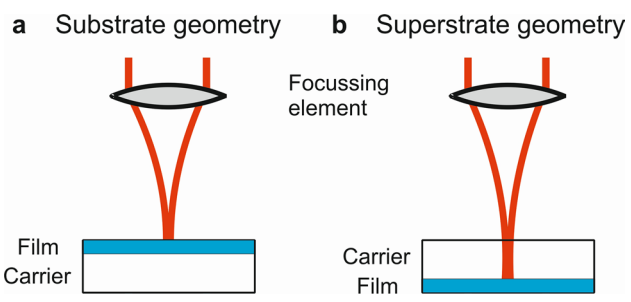

Fig. 1 Approaches for laser processing of thin films on a carrier through a focusing element (e.g., lens, concave mirror, diffractive optical element, etc.). **a** *Substrate geometry*: laser beam is incident to the air/film interface. **b** *Superstrate geometry*: laser beam is incident through the transparent carrier to the carrier/film interface

3.2 Interaction mechanisms

Laser-induced damage is referred to as an irreversible and permanent modification of the film material or surface morphology. Typically, it manifests at laser fluences exceeding a sharply defined threshold value, referred to as damage threshold fluence. The laser-induced damage of thin films can be caused by different physico-chemical *intra-* or *inter-pulse mechanisms*. While the first ones occur already upon irradiation by single laser pulses during the pulse duration, the latter ones manifest on longer time scales and result in changes of the film surface topography, its chemistry, or the intrinsic material structure through multiple laser pulses. Through this, multi-pulse irradiation often involves *damage accumulation* phenomena (often referred to as *incubation*) that can rely on the laser-induced formation of electronic defects in the film material or on *heat accumulation* when the laser-induced surface temperature does not cool down to the environmental temperature between successive laser pulses [1].

The laser-induced damage of single layered films typically can be associated with one of four different scenarios, as sketched in Fig. 2. In the first scenario (Fig. 2a), the film damage occurs at the air/film interface. This usually manifests for materials absorbing strongly the laser radiation, such as for metals. For these materials via linear absorption the absorbed laser intensity decays then exponentially within the film materials according to the Lambert–Beer law, typically at depths of a few tens of nanometers only. Thus, in most cases, the laser radiation does not reach the film/carrier interface.

In the second scenario (Fig. 2b), the laser-induced damage manifests at the film/carrier interface. This often occurs for thin transparent films on strongly absorbing carrier materials or for material combinations, where film and carrier exhibit very different thermal expansion coefficients.

In the third scenario (Fig. 2c), both film interfaces (air/film and film/carrier) become damaged. This may occur for transiently changing optical absorption mechanisms triggered upon irradiation with high-intensity ultrashort laser pulses and for weakly absorbing film materials with moderate and small band gap energies. In such a scenario, the low-intensity rising pulse slope can reach the film/carrier interface, while at the high-intensity pulse maximum, nonlinear absorption reduces the energy deposition depths and transiently confines most of the absorbed optical pulse energy to the air/film interface.

Finally, in the fourth scenario (Fig. 2d), the laser-induced damage occurs within the volume of the film material. Since typically for a given film material the interface damage threshold lies distinctively below the volume damage threshold, this scenario seldomly manifests for homogeneous thin film materials along with low or moderate laser fluences.

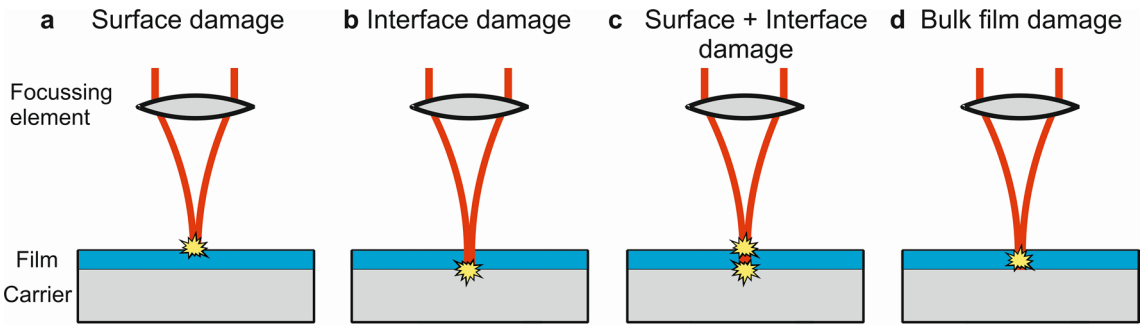

Fig. 2 Four different scenarios of laser-induced film damage. **a** Surface damage: the damage is induced at the air/film interface. **b** Interface damage: the damage is induced at the film/carrier interface. **c** Surface + interface damage: the damage is induced simultaneously at both the air/film and the film/carrier interfaces. **d** Bulk film damage: the damage is induced in the bulk of the film material

At extremely high irradiation intensities, however, the film material may be driven to highly excited thermodynamic states and may undergo *homogeneous melting* or *phase-explosion* [30, 32]. For (semi-)transparent films of medium or large thickness on high-reflecting carrier materials, a less known and often overlooked interference-based mechanism can rule the film damage threshold (see Sect. 3.3.2).

3.2.1 Interaction with metals

We follow the scenario according to Fig. 2a for high absorbing metals. In this chapter, results for gold and nickel films are presented because gold and nickel are excellent examples for materials with weak (gold) and strong (nickel) electron–phonon coupling [1].

In metals, energy absorption is governed by free electron transitions within the conduction band. Within the electron subsystem, the energy is spread on a time scale between tens of femtoseconds up to a picosecond. The thermalization between the electron subsystem and the lattice takes place typically on time scales between one and some tens of picoseconds.

In this paragraph, important findings for nanosecond pulse laser interaction with metal films are briefly described. For gold and nickel films on poorly heat-conductive fused silica substrates, Matthias et al. determined single-pulse ablation thresholds in the thickness range (h) from 50 nm to 7 µm for pulses with a pulse duration of $\tau = 14$ ns at a wavelength of $\lambda = 248$ nm [35]. For small film thicknesses $h < L_{th}$, they found a linear increase of the damage threshold fluence up to $h = L_{th} := (2D\tau)^{0.5}$, with D being the *thermal diffusivity* of the irradiated film material. For thicknesses $h > L_{th}$, the ablation threshold fluence is constant. The *thermal diffusion length* L_{th} was determined to be 1.05 µm for gold and 0.73 µm for nickel, respectively. All thicknesses h investigated were greater than the small-signal *optical penetration depth* α^{-1}. Here, α denotes the linear absorption coefficient. The investigations demonstrated that for material removal a certain minimal energy per unit volume must be deposited in the material. For a thermally well conductive material, F_{abl}/L_{th} is decisive and not the quotient F_{abl}/α^{-1}, because energy dissipates out of the excited volume element already during the nanosecond laser pulse. The characteristic scaling of the ablation threshold with $\tau^{0.5}$ for pulses with durations exceeding the electron–phonon relaxation time $\tau_{e\text{-}ph}$ is just a consequence of intra-pulse 1D heat transport into the bulk of the material [1]. For layer thicknesses $h < L_{th}$ the ablation threshold fluence F_{abl} is, thus, reduced by the factor h/L_{th} since the heat reaches the film/substrate interface already during the laser pulse and stays widely confined within the thin film due to the inefficient cooling by the underlying, poorly heat conductive dielectric substrate. For such thin films the deposited optical energy is restricted to the film and gives rise to a more efficient heating of the film material compared to films of thicknesses h exceeding L_{th}, thus reducing the ablation threshold fluence. For both metals (Au, Ni), it was found that the single-pulse ablation threshold fluence increases linearly with film thickness up to the thermal diffusion length of the film. Beyond this point, it remains independent of film thickness [35] since the additional film thickness can then support the normal "bulk cooling mechanism" via 1D heat (phonon) transport into depth.

In the femtosecond time domain, light absorption through valence electrons and succeeding hot electron diffusion govern the energy deposition. The electron gas is practically thermally insulated from the lattice of the solid. That means that the lattice initially stays “cold”, while the electrons may be heated by ultrashort pulsed laser radiation [36]. Depending on the strength of the electron–phonon coupling, hot electrons can penetrate deeply (compared to the optical penetration depth) into the material before any interaction with the lattice takes place. When an electron temperature (T_e) is established, the heat transport inside the metal can be described by the *two temperature model* (TTM) [36–38]. It consists of a set of two partial differential equations for the electron and the lattice temperature (T_l), coupled by a

term describing the strength of the electron–phonon interaction (electron–phonon coupling constant g) multiplied by the temperature difference (T_e–T_i). Hence, any temperature difference between the electrons and the lattice drives an energy exchange among both sub-systems until a thermal equilibrium is reached. Along with suitable boundary conditions (laser, sample geometry, material properties, etc.) the TTM equations can be solved numerically to gain temporal solutions of the temperature fields of the electrons and the lattice, respectively.

The TTM is the backbone of most computational studies of the interaction of ultrashort laser pulses with solids and has been combined already with other advanced numerical simulations (in 2D and 3D), such as *molecular dynamics* (MD) or *finite-difference time-domain* (FDTD) calculations. Explicit representations of the TTM along with numerical solutions can be found in the persistent literature [1, 25, 36–46]. Here, selected results applying the TTM are shown in the following. The time dependence of the electron and the lattice temperatures predicted by the TTM for gold and nickel films are depicted in Fig. 3 [38]. Absorption of a single laser pulse with a duration of 200 fs at 400 nm wavelength and a laser fluence of 0.023 J/cm^2 is sufficient to reach the melting temperature (T_m) of the lattices in both cases. The electron and lattice temperatures at the front and rear surfaces of the 100 nm thick films on fused silica substrates are plotted for both metals through solid or dashed lines, respectively. The transfer of energy to the lattice proceeds about ten times faster for nickel due to a much stronger electron–phonon coupling in nickel compared to gold. It is obvious that no significant heat transport through the nickel film to the rear surface takes place, where nearly no temperature difference to the initial sample temperature is calculated even when the front surface reaches the melting point (see the bottom part of Fig. 3). In contrast, for gold (top part of Fig. 3), front and rear surface temperatures are indistinguishable. In this case, the absorbed optical energy can quickly spread through the ballistic transport and diffusion of electrons through the entire 100 nm thick gold film, being confined to it through the poorly electrically conductive fused silica substrate, before the excited electron's energy can be converted to heat via the release of phonons through electron–phonon scattering. Thus, both the front and the rear surface exhibit the same temperature. Figure 3 shows very clearly that the equilibration time for electrons and lattice depends on the electron–phonon coupling constant g [38] explaining the large differences between Ni (g(Ni) = 3.6×10^{17} W/(m^{3}K) [1]) and Au (g(Au) = 2.1×10^{16} W/(m^{3}K) [1]).

Corkum et al. [37] demonstrated in a fundamental work that for bulk metals a critical laser pulse duration τ_c, above which the damage threshold fluence shows the usual $\tau^{0.5}$ dependence for longer (picosecond and nanosecond) pulses, is inverse proportional to the electron–phonon coupling

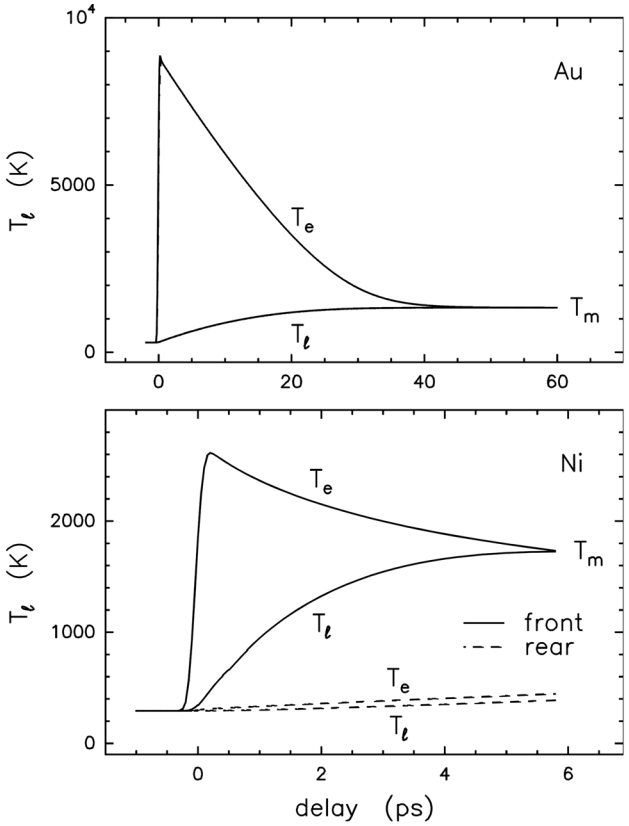

Fig. 3 Time dependence of the electron (T_e) and lattice (T_l) temperatures of 100 nm thick gold (top panel) and nickel (bottom panel) films on a fused silica substrate upon irradiation with single fs-laser pulses (400 nm, 200 fs, 0.023 J/cm^2) as calculated by the two-temperature model [38]. The laser pulse hits the surface at the delay time zero. Solid lines represent the temperatures at the air/metal interface, while the dashed lines display the values at the metal/silica interface. Note the different scaling of the abscissa. Reprinted by permission from Springer-Verlag: Applied Physics A **69** [Suppl.]: S99–S107 (The role of electron–phonon coupling in femtosecond laser damage of metals, Wellershoff, S.-S. et al.), Copyright (1999)

constant g. For laser pulse durations below τ_c, the damage threshold remains constant due to linear absorption and energy confinement during the pulses.

Multi-pulse damage threshold fluences of gold films were investigated by Stuart et al. for a 200 nm thick gold grating with 600 pulses per spot at 1053 nm wavelength and pulse durations in a range from 140 fs to 1 ns [6]. The damage threshold was detected by scanning electron microscopy. Later, Wellershoff et al. presented a TTM fit to the experimental data of Stuart et al. [38] (see Fig. 4). In addition to the "standard" TTM, they considered transient absorption due to a change of reflectivity with electron temperature. A good agreement between experimental data and the TTM prediction is found in the entire range of pulse durations if transient optical absorption is included. An arrow indicates

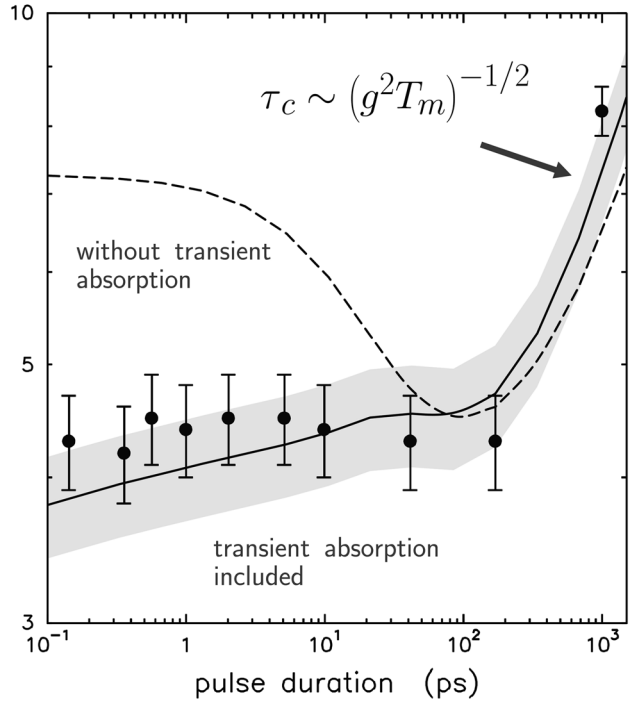

Fig. 4 Pulse duration (FWHM) dependence of the melting threshold fluence of a 200 nm thick gold coated optical grating upon irradiation with single fs-laser pulses (1053 nm). The data points (full circles) are measured by Stuart et al. [6]. The solid line with the gray shaded band results from TTM calculations, including uncertainties of material parameters and considering transient changes of the surface reflectivity with the electron temperature [38]. The dashed line results from TTM calculations assuming constant absorption. The arrow marks the critical pulse duration τ_c above which 1D heat transport with equilibrium thermal diffusion causes a $\tau^{0.5}$-scaling of the melting threshold. T_m denotes the melting temperature. Reprinted by permission from Springer-Verlag: Applied Physics A **69** [Suppl.]: S99–S107 (The role of electron–phonon coupling in femtosecond laser damage of metals, Wellershoff, S.-S. et al.), Copyright (1999)

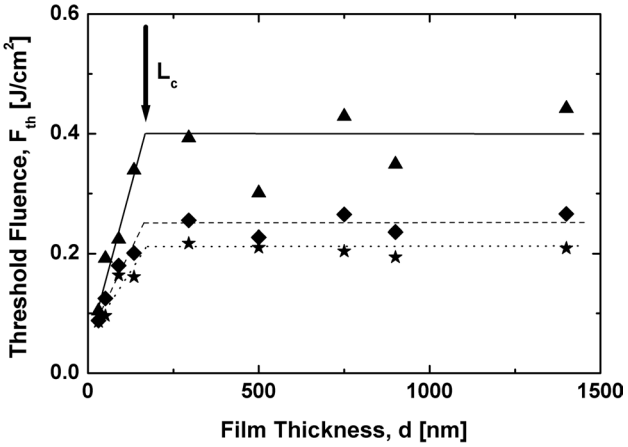

Fig. 5 Film thickness dependence of the ablation threshold fluence of gold films on BK7 glass upon multi-pulse fs-laser irradiation (793 nm, 28 fs; $N = 100$: ▲ and solid line; $N = 1000$: ◆ and dashed line; $N = 10{,}000$: ★ and dotted line) [47]. The arrow labeled with L_c marks the energy penetration depth into the material. The lines guide the eye. Reprinted from [47], Appl. Surf. Sci., Vol. **253**, Krüger, J. et al., Femtosecond laser-induced damage of gold films, 7815–7819, Copyright (2007), with permission from Elsevier

the time τ_c. For pulse durations longer than τ_c, the damage threshold fluence scales with $\tau^{0.5}$.

Single- and multi-pulse ablation threshold values were investigated for 28-fs laser treatment at 793 nm wavelength [47]. Gold films with different thicknesses between 31 and 1400 nm were deposited on BK7 glass substrates. Damage (ablation) was detected by means of an optical microscope.

Figure 5 gives ablation threshold values in dependence on the gold film thickness for multi-pulse laser treatment ($N = 100$, 1,000, and 10,000 pulses per spot) [47]. For films with thicknesses smaller than 180 nm, increasing threshold values with rising thickness are observed. For thicker films (> 180 nm), the ablation threshold value is constant and remains at its bulk value. A characteristic penetration depth of the pulse energy into the material of $L_c \approx 180$ nm is observed. Here, L_c exceeds the optical penetration depth α^{-1} of about 12 nm by more than one order of magnitude. This is a direct consequence of the weak electron–phonon coupling in the case of gold discussed above. The resulting electron thermal diffusion length (before interaction with the lattice) is the crucial quantity for fs-laser material processing, especially for the damage threshold.

The specification of multi-pulse damage threshold fluences is suitable particularly for industrial users, since this definition includes the amplification and visualization of small (single-pulse-induced) defects and also includes possible incubation phenomena. Incubation means that for a fixed laser fluence one or more pulses can be applied to the material without macroscopic material removal. After these (few) incubation pulses, which irreversibly modify the material (chemically, surface properties, color center generation, etc.), the material removal starts with the following laser pulses. Incubation effects are well known for many materials and a large variety of laser parameters. It was also observed in the context of the above-mentioned ablation of gold films. The ablation threshold fluence changed between 0.7 J/cm^2 (single pulse) and 0.2 J/cm^2 (10,000 pulses per spot) [47].

The pulse number (N) dependence of the laser-induced damage threshold fluence of (bulk) metals can be described by a power law [48]

$$F_{th}(N) = F_{th}(1) \cdot N^{\xi - 1}, \quad (1)$$

with $F_{th}(1)$ and $F_{th}(N)$ are the single- and multi-pulse damage threshold fluences, respectively, and ξ is a material-dependent incubation parameter. The model considers mechanical fatigue damage caused by repetitive stress-induced strain and has been found to successfully describe

the laser treatment of gold films in a thickness range from 90 nm to 1.5 µm (on fused silica substrates) with femtosecond laser pulses ($\tau = 200$ fs, $\lambda = 400$ nm). $\xi = 0.92$ was calculated [49]. In another femtosecond laser investigation ($\tau = 28$ fs, $\lambda = 793$ nm) of gold films, $\xi = 0.87$ was found [47].

In addition to the investigations on metal films described above, an important experimental finding, which was determined on bulk material, completes this section. Nolte et al. described multi-pulse experiments on the ablation of copper targets with laser pulse durations between 150 fs and 30 ps [25]. For laser pulses shorter than 1 ps and at low laser fluences (close to the ablation threshold), a "gentle ablation regime" was found. Here, the average ablation rate is determined by the optical penetration depth α^{-1}. For higher fluences, "strong ablation" is observed, where the effective heat penetration depth determines the average ablation rate. For laser pulses with durations longer than 1 ps, the "gentle regime" is not present [25]. It should be noted that the electron–phonon coupling constant of copper amounts to $g = (0.9 \pm 0.1) \times 10^{17}$ W(m^{3}K) [50] which indicates a strong coupling of the electrons to the lattice.

Apart from the already discussed optical constraints and influence of the electronic properties of the irradiated solids, also thermophysical effects that determine the relaxation dynamics of fs-laser excited metal films, e.g., via interfacial mechanical stress, hydrodynamic melt flows of the film material, or even substrate de-wetting effects, may have to be considered [51]. In this context, the irradiation of several tens of nanometer thin gold films upon single, tightly focused fs-laser pulses should be illustrated. That topic gained attention around 2004, when a Japanese and a German group independently reported the formation of submicrometric nanojet-like morphologies frozen at the surface of thin gold films [52, 53].

Figure 6 assembles a series of side-view scanning electron micrographs of a 60 nm thick magnetron sputtered gold film on a quartz glass substrate after exposure to single Ti:sapphire laser pulses ($\tau = 30$ fs, $\lambda = 800$ nm) of varying energies (fluences) that were focused by a 36 × Schwarzschild microscope objective (NA = 0.5) in substrate geometry [53]. For all laser pulse energies between 6 and 13 nJ a pedestal bump with heights up to ~ 800 nm is seen at the film surface. At pulse energies exceeding 7–8 nJ, an additional central protruding nanojet-feature manifests at the surface, exhibiting a pulse energy dependent aspect ratio along with heights up to 1–1.5 µm.

These publications have triggered further systematic theoretical and experimental research, including thermoelastic continuum modeling [54] and atomistic molecular dynamics simulations [55, 56], as well as time-resolved measurements [57, 58]. The numerical modeling revealed that the bump is caused by thermoelastic stress causing a delamination of the metal film from the dielectric substrate, while the nanojet itself forms from molten film material through intertia accompanying the hydrodynamic melt dynamics and is limited in its height by surface tension effects through the Rayleigh-Plateau instability of the melt [54, 56, 58]. Side-view shadowgraphic measurements indicated that the complete melting and re-solidification dynamics is terminated withing ~ 250 ns [58]. From their experiments, the authors have drawn the following physical scenario: approximately 5 ns after the impact of the fs-laser pulse, the thin gold film bulges and exhibits a bump of ~ 2.4 µm in height and of ~ 4.5 µm in diameter. At a delay time of ~ 35 ns, the bulge structure collapses and a jet of molten material starts to emerge at its center. While the bump height further decreases, the central jet grows to a length of ~ 4 µm and is continuously expanding until a delay time of ~ 125 ns. After ~ 150 ns, the jet detaches from the bump. Caused by the Rayleigh-Plateau instability the jet disintegrates into two components, i.e., into a small spherical droplet at its tip followed by a larger elongated droplet. Upon detachment, a very thin sub-micrometric spike remains at the base of the structure. At even larger delay times, the shape of the droplets turn spherical through the surface tension of the molten gold, while they are moving away from the substrate at velocities between 20 and 30 m/s [58]. This dynamic evolution explains the strong fluence dependence of the remaining nanojet-like surface spikes observed in Fig. 6.

In view of these time-resolved shadowgraphy experiments and the molecular dynamics simulations, the formation of the permanent nanojet surface features shown in Fig. 6 can be seen as the residuals of a laser-induced film material transfer that is similar to the laser-induced forward transfer (LIFT, see Sect. 4.4 below), with the only difference that here the irradiation is performed in substrate geometry and not in superstrate geometry (as for the LIFT).

3.2.2 Interaction with semiconductors and dielectrics

For "weakly" absorbing materials such as dielectrics or even semiconductors, whose band gap E_g (minimum energy difference between valence band (VB) and conduction band (CB)) is larger than the energy $h\nu$ of the irradiating photons, a different concept for describing material destruction has proven successful: in many of such materials, free charge carriers in the conduction band are present only in small numbers under normal conditions (typically 10^8–10^{10} cm^{-3}), but can be generated by photo-excitation. This is done for high intensities in the range between 10^{11} and 10^{14} W/cm^2 on the one hand by (1) nonlinear *multi-photon absorption* (MPA) or on the other hand by (2) absorption of the radiation by electrons already being present in the CB (*free-carrier absorption*), followed by *impact ionization*. In this context, "ionization" means the generation of an electron–hole pair. The mechanism (2) can lead to an avalanche-like increase of

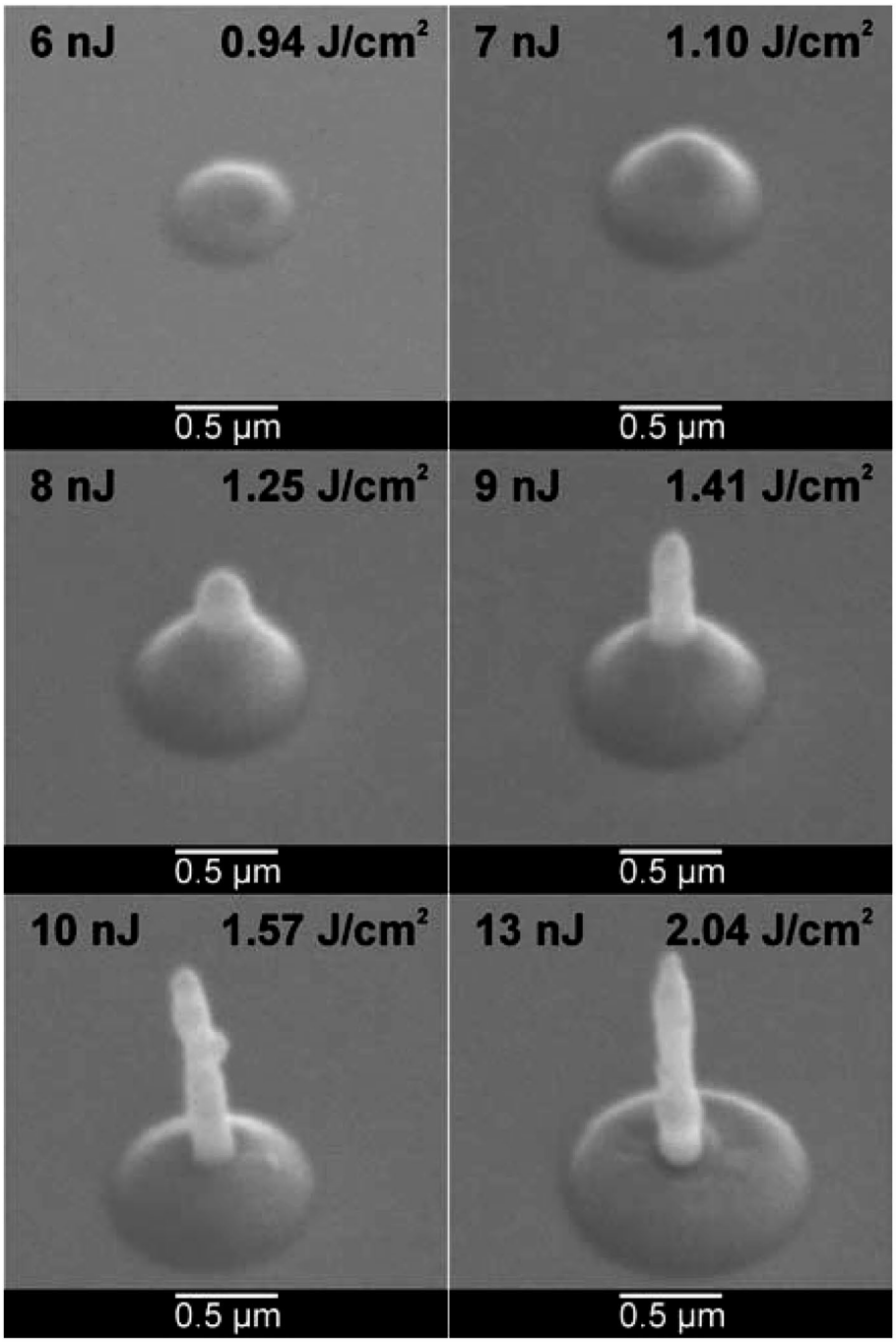

Fig. 6 Side-view scanning electron micrographs of sub-wavelength surface structures generated on a gold film ($h = 60$ nm) on a quartz glass carrier upon irradiation by single, tightly focused fs-laser pulses of different pulse energies varying between 6 and 13 nJ (800 nm, 30 fs) [53]. Reprinted by permission from Springer-Verlag: Applied Physics A **79**:879–881 (Formation of microbumps and nanojets on gold targets by femtosecond laser pulses, Korte, F. et al.), Copyright (2004)

the number of electrons in the CB still during the laser pulse excitation and is, therefore, also called *avalanche ionization* (AI). An optical breakdown ("*laser-induced breakdown*") manifests when a critical electron density N_e^{cr} is exceeded in the conduction band of the solid as a result of the irradiation which then ultimately leads to material destruction [5]. This characteristic charge carrier density is material dependent and typically lies between 10^{19} and 10^{21} cm^{-3} [1].

For a quantitative understanding of these effects, the time evolution of the charge carrier density N_e of the electrons in the conduction band as consequence of the exposure to a laser pulse with an intensity profile $I(t)$ can be described by a single differential rate-equation which takes into account the charge carrier generation in the conduction band by AI (first term) as well as by MPA (second term) [6]

$$\frac{dN_e}{dt} = \Xi_{av} \cdot I(t) \cdot N_e(t) + \gamma_m \cdot I^m(t), \quad (2)$$

Ξ_{av} denotes the avalanche coefficient and γ_m the coefficient for the absorption of m photons. Here, m is the minimum number of photons required for a transition between valence and conduction bands ($m \cdot h\nu \geq E_g$). In the rate equation, loss mechanisms (e.g., carrier diffusion or recombination) have been neglected, which is specifically justified for ultrashort laser pulse durations. It is very instructive to analyze separately the two limiting cases of pure AI or pure MPA. Equation (2) can then be solved analytically by separating the variables. This procedure allows in both cases a statement about the scaling behavior of the materials damage threshold fluence F_{th} with the laser pulse duration τ. However, for high laser intensities, the two effects (AI and MPA) often occur simultaneously, so that the rate equation must then be solved numerically. In particular, for large bandgap materials such as fused silica (SiO_2: $E_g \sim 8.3$ eV), MPA at very small pulse durations ($\tau \sim 10$ fs) provides an efficient mechanism to generate seed electrons for the subsequent avalanche process. Note that for such short pulse durations and at high intensities also *tunnel ionization* effects may have to be considered [59].

In the first limiting case of pure avalanche ionization ($\gamma_m = 0$), the expression $N_e(\tau) = N_0 \cdot \exp\left\{\Xi_{av} \cdot \int_0^\tau I(t)\mathrm{d}t\right\}$ is obtained immediately after laser pulse excitation, i.e., an avalanche-like (exponential) increase of the electron concentration occurs, explaining the name of this intra-pulse ionization process. The quantity N_0 is the number of electrons already being present in the CB at the beginning of the laser pulse. The expression $\int_0^\tau I(t)\mathrm{d}t$ represents, by its definition, the fluence F of the laser pulse. Thus, the critical electron density N_e^{cr} is just reached at the fluence threshold

$$F_{th}(\tau) = \frac{1}{\Xi_{av}} \cdot \ln\left(\frac{N_e^{cr}}{N_0}\right) = \text{Const.} \tag{3}$$

In the case of pure AI, the damage threshold fluence is, therefore, independent of the laser pulse duration.

In the second limiting case of pure m-photon absorption ($\Xi_{av} = 0$), rate Eq. (2) yields the solution $N_e(\tau) = N_0 + \gamma_m \cdot \int_0^\tau I^m(t)\mathrm{d}t$. If one assumes a temporal rectangular pulse of intensity I_0 to simplify the mathematical analysis, there is a linear relationship between fluence F and intensity I_0 of the pulse ($F = F_0 = I_0\tau$). Thus, the pulse duration dependence of the damage threshold can be directly derived:

$$F_{th}(\tau) = \gamma_m^{-1/m} \cdot \left[N_e^{cr} - N_0\right]^{1/m} \cdot \tau^{\frac{m-1}{m}}. \tag{4}$$

Thus, the damage threshold fluence F_{th} scales with a power law $\tau^{(m-1)/m}$. For $m = 1$ (linear absorption) the threshold is independent of the pulse duration (consistent with the results gained for metals in the frame of the TTM [37], see Sect. 3.2.1). This result is also in line with the above result for pure AI, which is also based on a cascade of linear absorption processes. It is interesting to note at this point that pure two-photon absorption ($m = 2$) also leads to the characteristic $\sqrt{\tau}$ scaling law as it is also obtained by the distinct physical process of 1D heat transport for longer ps- to ns-pulse durations. In case that several different orders m of nonlinear absorption simultaneously contribute to the carrier generation in the CB, Eq. (2) may be solved numerically but some general trends may be summarized as follows: linear absorption mechanisms produce a constant damage threshold, while multi-photon absorption leads to decreasing thresholds for shorter laser pulses with durations below the electron–phonon relaxation time. Larger values of m manifest in a stronger reduction of the damage threshold fluence with decreasing τ. Therefore, an experimental measurement of $F_{th}(\tau)$ with ultrashort laser pulses allows conclusions to be drawn about the physical damage mechanisms being involved [6, 19, 60, 61].

Mero et al. studied the single-pulse damage threshold of five different ion beam sputter-coated oxidic thin dielectric films with band gap energies E_g between 3.3 and 8.3 eV (TiO_2, Ta_2O_5, HfO_2, Al_2O_3, SiO_2; film thickness h ranging between 500 and 800 nm) on fused silica substrates employing Ti:sapphire ultrashort laser pulses with durations between 25 fs and 1.3 ps [62]. Figure 7a plots the corresponding data of the damage threshold fluence F_{th} as function of the pulse duration τ, while in Fig. 7b the damage threshold fluences of $\tau = 30$ fs (full circles) and 1.2 ps (open circles) laser pulses are plotted vs the band gap energy E_g of the film materials. The pulse duration scaling in Fig. 7a suggest the significant involvement of multi-photon absorption processes, whereas a strictly linear dependence on the band gap energy is evident from Fig. 7b. Thus, the damage threshold is determined by intrinsic material properties rather through defects and impurities caused by imperfections in the film deposition process.

Combining their measurements of the pulse duration and the band gap scaling with a rate-equation model extended from the damage models of Stuart et al. [6] and Keldysh [59] by adding a carrier density decay term considering relaxation and re-absorption effects through electronic defects, such as *self-trapped excitons* (STEs), the authors proposed a phenomenological damage scaling law $F_{th}(\tau, E_g)$ according to

$$F_{th}(\tau, E_g) = \left(c_1 + c_2 E_g\right) \cdot \tau^{\kappa}, \tag{5}$$

where c_1, c_2 and κ are fitting parameters [62]. Values of the exponent κ ranging between 0.27 and 0.33 were found for all five oxidic film materials—rather independent of the actual band gap energy. Based on their retrieved values of the fit parameters to this model, the authors attributed this observation to a significant contribution of AI to the carrier

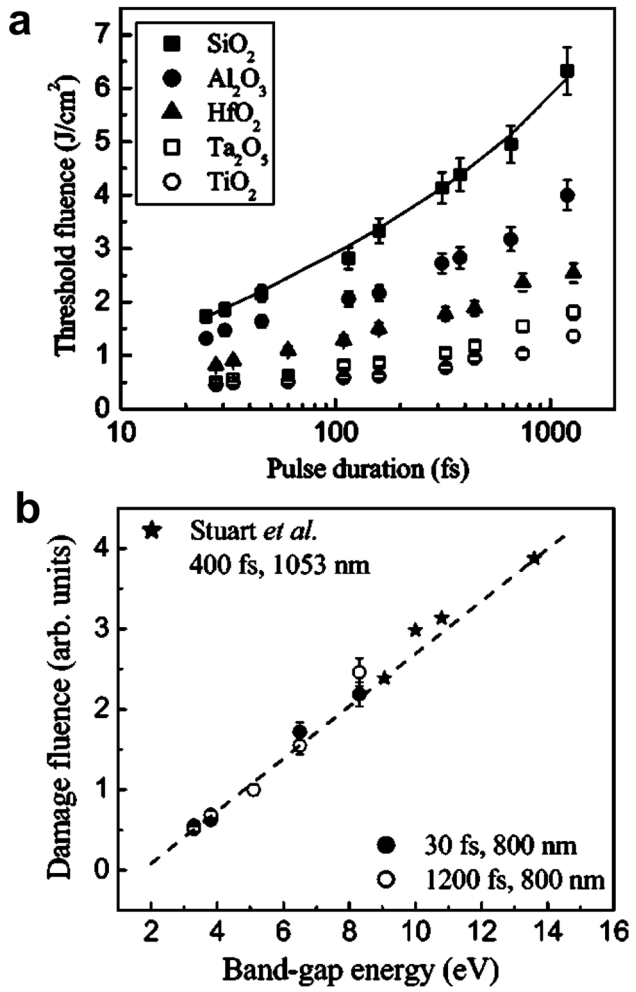

Fig. 7 Damage threshold fluence of oxidic dielectric films (TiO_2, Ta_2O_5, HfO_2, Al_2O_3, SiO_2; film thickness $h = 500$–800 nm) on fused silica substrates upon irradiation with single fs-laser pulses (800 nm) [62]. **a** Scaling with pulse duration. **b** Scaling with band gap energy for two pulse durations of $\tau = 30$ fs (full circles) and 1.2 ps (open circles). The data points are normalized to the damage threshold fluence at $E_g = 5.1$ eV. The data points encoded by asterisks are taken from [6]. Reprinted figures with permission from Mero, M. et al., Phys. Rev. B, **71**, 115109, 2005. Copyright (2005) by the American Physical Society

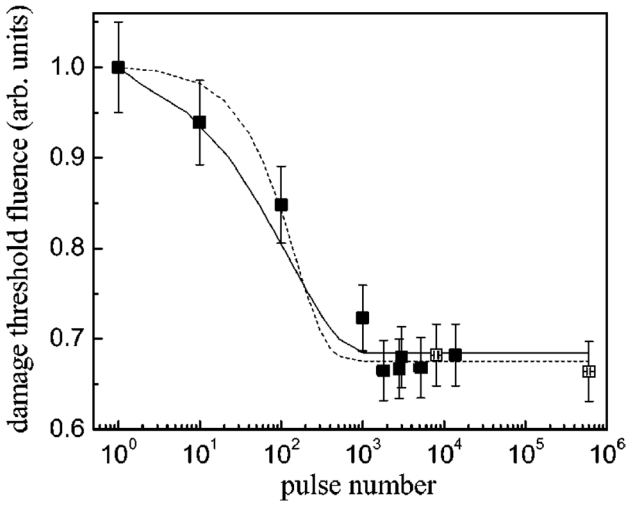

Fig. 8 Normalized damage threshold fluence of a ~ 550 nm thick Ta_2O_5 film on a fused silica substrate as a function of the number of irradiating fs-laser pulses (800 nm, 30 fs, 1 kHz) [63]. The experimental data points (full squares) are normalized with the single-pulse damage threshold value $F_{th}(1) = 0.6$ J/cm^2. The lines represent least-square fits (for details see the text). Reprinted from [63], Optical Engineering Vol. **44**, Mero, M. et al., On the damage behavior of dielectric films when illuminated with multiple femtosecond laser pulses, 051107, Copyright (2005), with permission from SPIE

excitation—even at pulse durations as short as a few 10 fs. As consequence, the power law (Eq. (5)) and the exponent κ are rather insensitive to the specific values of the multiphoton and avalanche coefficients. At constant pulse duration the damage threshold fluence exhibits an approximately linear scaling with the band gap energy, pointing toward photoionization as process controlling this behavior [62].

An extended consortium around these researchers studied also the pulse-number (N) dependence of the same set of single-layer film materials, having a special focus on the reduction of the damage threshold for multiple fs-laser pulses (780–800 nm, 13–150 fs, 1 Hz–1 kHz), i.e., incubation effects [63]. The decrease of the damage threshold with N was explained with the accumulation of STEs having a lifetime exceeding tens of minutes. The formation of STEs occurs on a time scale much faster than 1 ms and explains the observation of the independence of the damage threshold on the pulse repetition frequency in the range from 1 Hz to 1 kHz. The authors developed a detailed rate equation model for the CB electron density that includes STEs and shallow traps as electronic inter-band defect states. The corresponding set of two coupled differential rate equations was solved numerically to explain the multiple-pulse damage behavior. According to this incubation model, the STEs control the dependence of the damage threshold fluence on N, while the shallow traps are involved in thermal heating effects at low laser fluences.

Figure 8 exemplifies the capabilities of this incubation model for a ~ 550 nm thick Ta_2O_5 film on fused silica upon irradiation at 1 kHz pulse repetition rate (800 nm, 30 fs) [63]. The data points (full squares) were obtained in experimental N-on-1 measurements of the damage threshold fluence, normalized to the single-pulse threshold value that accounts to $F_{th}(1) = 0.6$ J/cm^2 here. The solid line represents a numerical fit to the complete set of the two rate equations (for details see [63]), while the dashed line is based on a least-squared-fit to the approximating analytical model presented in Eq. (6):

$$F_{\mathrm{th}}(m,N) = F_{\mathrm{th}}^{\mathrm{m}}(\infty) + \left[F_{\mathrm{th}}^{\mathrm{m}}(1) - F_{\mathrm{th}}^{\mathrm{m}}(\infty)\right]\left(1 - \frac{\tau_1}{\tau_2}\cdot\frac{n_1}{n_2}\right)^{N-1}. \quad (6)$$

In this power law, m is again the order of the MPA process and accounts to $m=3$ for the Ta_2O_5 material. The last term in round brackets on the right-hand side controls the asymptotic approach to the value $F_{\mathrm{th}}^{\mathrm{m}}(\infty)$ at a very large number of laser pulses. It is determined by the ratio of the band-to-band relaxation time τ_1 and the creation time τ_2 of the absorbing inter-band electronic states, as well as by the ratio of the electron density n_1 generated by a single laser pulse and the maximum density of trap states n_2.

In 2015, Sun et al. introduced a generalized incubation model for the irradiation of film and bulk materials that is based on two physical mechanisms, i.e., (i) laser pulse induced change of the optical absorption and (ii) the laser-induced decrease of the specific energy that is required to damage the sample [64]. Given the very general nature of these mechanisms, the model is applicable to a broad class of materials (metals, semiconductors, dielectrics) and can explain changes of the damage threshold fluence as a function of the laser repetition rate. Details about the mathematical implementation of the model and a software to fit experimental data can be found online [65].

Driven by the potential of industrial applications, large-area surface structuring by lasers is continuously moving into the focus of scientific and technical investigations. For dielectric materials, this is complicated due to the large band gap energies, typically requiring nonlinear laser-matter interactions for material excitation when the single photon energy is significantly smaller than the band gap energy. Along with the material-specific incubation effects discussed above, this makes a homogeneous large-area surface structuring very challenging and highly dependent on the laser processing parameters, such as the spatial beam shape, peak fluence, pulse repetition frequency, laser scanning velocity (both define the spot-overlap within a scan line), and the inter-line separation. One way to overcome this difficulty can lie in adding a very thin but strongly absorbing cover-layer on the surface of the transparent dielectric to facilitate resonant coupling effects of the laser radiation into the material underneath the cover-layer.

As an example, Kunz et al. [66] demonstrated that through this approach employing a 20 nm thick gold cover-layer large surface areas can be laser-processed by near-infrared fs-lasers (1025 nm, 300 fs, 100 kHz) on fused silica glass samples to be homogeneously covered by sub-wavelength surface nanostructures, so-called *laser-induced periodic surface structures* (LIPSS, for more details on their formation and applications the reader is referred to [67–70]). A scheme of their approach is shown in Fig. 9a along with the generated HSFL in Fig. 9b.

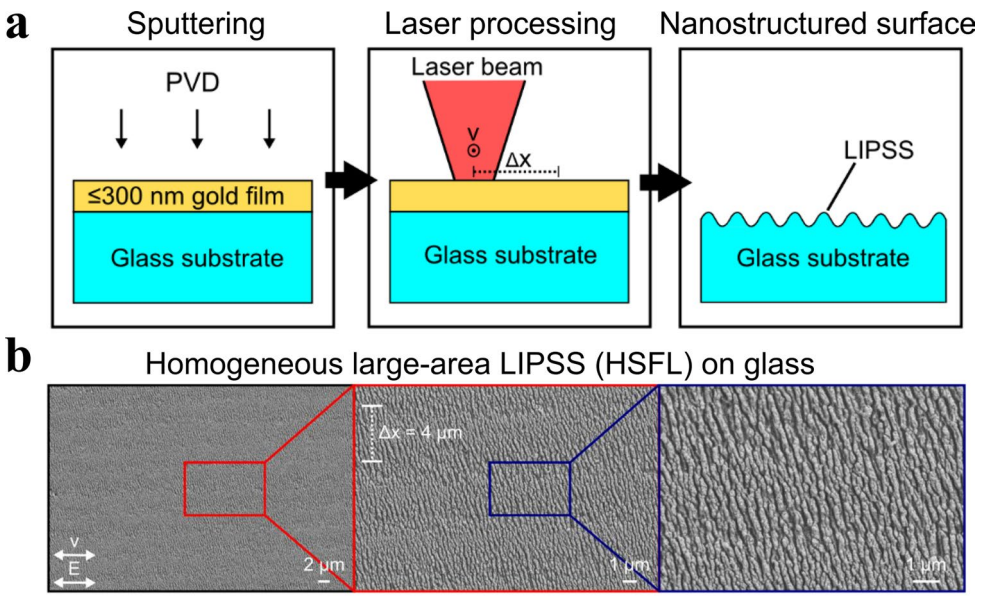

Fig. 9 Thin Au-film mediated surface nanostructuring of fused silica glass samples by sub-wavelength LIPSS (HSFL-type) [66]. **a** Scheme of the process conducted in *substrate geometry*. **b** Zoom-series of top-view SEM micrographs after the laser processing (1025 nm, 300 fs, 100 kHz, $F_0=4.5$ J/cm^2, $v=0.15$ m/s). The scan direction (v) and polarization direction (E) are indicated in the left image. $\Delta x=4$ µm denotes the inter-line separation. Reprinted (adapted) from [66], Kunz, C. et al., Large-area fabrication of laser-induced periodic surface structures on fused silica using thin gold layers, Nanomaterials (Basel, Switzerland) **10**:1187, Copyright 2020 under Creative Commons BY 4.0 license. Retrieved from https://doi.org/10.3390/nano10061187

3.3 Transient effects

In this section, complex transient phenomena are pointed out that may affect the film processing with ultrashort laser pulses. This includes extremely fast (non-thermal) *intra-pulse* effects that can occur already during the laser pulse, but also slower *inter-pulse* processes that are just initiated by the laser pulses but may occur on much longer time scales up to the microsecond range. This manuscript part is divided in two sub-sections, where specific effects of "thin film" laser-matter interaction are discussed (Sect. 3.3.1) and complemented to effects being relevant for "thick films" (Sect. 3.3.2).

3.3.1 Thin films: surface ablation and interfacial spallation

For thicknesses $h < \lambda <$ Rayleigh length (DOF) films will be considered as "thin" here. As already discussed in Sect. 3.2.1, for strong absorbing materials such as metals there may be a characteristic linear dependence of the ablation threshold fluence on the film thickness if h is smaller than the thermal diffusion lengths of the electrons. However, for transparent films that are deposited on strongly absorbing carriers, the sample damage typically follows other pathways. This originates from the fact that the laser radiation is not significantly absorbed or scattered in the transparent film before being deposited in the carrier material close to the film/substrate interface. Additionally, the transparent film may act as classical Fabry–Perot resonator that is affecting the amount of back-reflected radiation via the coherent superposition and interference of the Fresnel reflections occurring at the air/film and film/substrate interfaces. Moreover, the presence of the transparent thin films may hinder the excited substrate material from being ablated by covering the laser-excited material, leading to a situation of *"frustrated ablation"*. As a consequence, for a sufficiently thick transparent film, the ablation threshold fluence of such a film-substrate combination may be even higher than the threshold value of the strong absorbing substrate material itself.

The dynamics of laser ablation by single fs-laser pulses has been studied by McDonald et al. through complementary fs-time-resolved pump-probe side-view shadowgraphy and top-view microscopy on the ps–ns time scale for a set of silicon wafer samples covered by different thermally grown oxide thicknesses varying between a few tens of nanometers up to $h = 1.2$ µm [71]. Figure 10a compiles the corresponding side-view shadowgraphy images for five selected pump-probe delays Δt (columns) of 0.21 ns, 2.35 ns, 5.01 ns, 7.68 ns, and 10.35 ns as well as for five different oxide layer thicknesses (rows) of 20 nm, 54 nm, 147 nm, 300 nm, and 1,200 nm, respectively, upon irradiation with

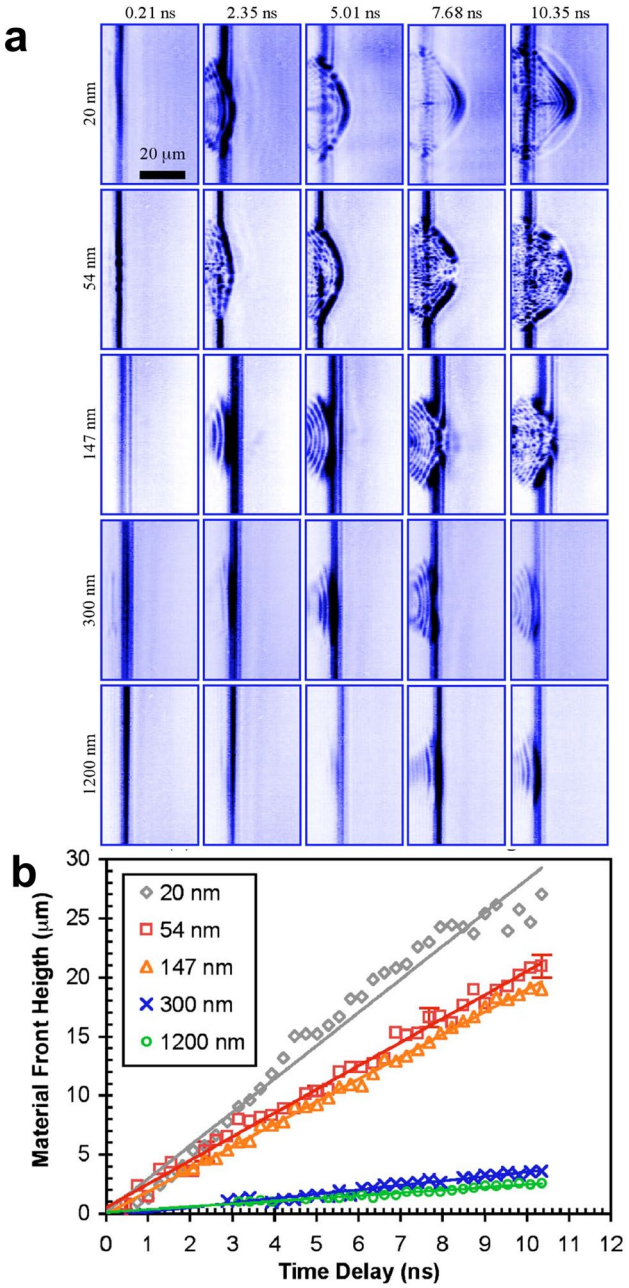

Fig. 10 Single fs-laser pulse ablation (775 nm, 150 fs, 1.3 J/cm^2) of thermally grown SiO_2-oxide layers of different thicknesses ($h = 20$ nm, 54 nm, 147 nm, 300 nm, 1,200 nm; rows) from (100)-silicon wafers [71]. **a** Pump-probe side-view shadowgraphic images for five selected delay times $\Delta t = 0.21$ ns, 2.35 ns, 5.01 ns, 7.68 ns, 10.35 ns (columns). The laser is incident from the right. All images share the same scale bar provided in the top left image. **b** Extracted position (height, *MFH*) of the ablating material front vs the time delay. The solid lines represent linear least-squares-fits to the equation $MFH = v_{film}\Delta t$. **a**, **b** are reprinted from McDonald, J.P. et al., Pump-probe imaging of femtosecond pulsed laser ablation of silicon with thermally grown oxide films, J. Appl. Phys. **102**:063109 (2007), with the permission of AIP Publishing

single Ti:sapphire fs-laser pulses at a fluence of 1.3 J/cm^2 (775 nm, 150 fs).

The dark/blue regions represent ablating material as well as the sample surface. The vertical fringes around the surface are caused by edge diffraction of the probe beam radiation. For the 20 nm thin oxide film sample, at large delays (10 ns) the front of a shock wave formed in air is visible as a bright semi-circular boundary. It can be distinguished from the dark appearing material front that lags behind. For medium oxide film thicknesses of ~ 50 nm to ~ 150 nm, the ablated material front appears fractured at that time delay. For even larger film thicknesses (300 nm, 1,200 nm), the spatial expansion of the material is strongly reduced. From these side-view shadowgraphy measurements, for each oxide layer thickness, the position of the material front was extracted and plotted as a function of the time delay Δt (Fig. 10b). For all data sets, a linear scaling with Δt can be seen that allows to quantify the velocity of the ablating material as the slope of the least-squares-fits. Values ranging between $v_{\mathrm{film}} = 3010 \pm 360$ m/s ($h = 20$ nm), exceeding the speed of sound in air by a factor of ~ 10, down to 200 ± 20 m/s ($h = 1200$ nm) were obtained [71].

In 2013, Rapp et al. extended the studies of the same material system (SiO_2 films of different thickness on Si wafers) to the earlier (ps–ns) and later (10–100 ns) ablation stages through fs-time-resolved pump-probe top-view microscopy of the surface reflectivity upon single fs-laser pulse irradiation [72]. This technique was initially developed by Downer et al. in 1985 [73] and further improved by Sokolowski-Tinten and von der Linde [74]. This led to a significantly improved understanding of the physical processes involved in ultrashort pulsed laser ablation, including the transient appearance of Newton-fringes caused by the formation of a stress-related *rarefaction wave* [8]. Meanwhile, fs-time resolved microscopy (fs-TRM) has been extended into many different powerful imaging modalities (see Refs. [75–77] and references therein).

Figure 11a presents a collage of brightfield fs-TRM images of spots at SiO_2-film covered (100)-silicon wafer surfaces upon irradiation by single fs-laser pulses (1053 nm, 660 fs, 1.0 J/cm^2) [72]. For two samples of different oxide film thicknesses (upper row $h(SiO_2) = 100$ nm; lower row: $h(SiO_2) = 500$ nm), the images were acquired after ten specific delay times Δt of the illuminating probe pulses ranging between 0 ps and 100 ns. The right image in each row labeled with "∞" displays the permanent laser-induced surface modification for comparison.

At a delay time of ~ 1 ps the reflectivity of the laser-irradiated spot appears bright due to the melting of the silicon (Fig. 11a). After ~ 10 ps, the reflectivity in the center of the spots drops again and develops into a transiently changing ring pattern that is persistent between several hundreds of picoseconds and a few nanoseconds. It is caused by interference effects through Newton fringes. The general principle of their formation through the interference of a reflection at the ablation front and a reflection by the sample surface after passing twice through the semi-transparent ablating material is sketched in Fig. 11b (taken from [8]). Note that the characteristic Newton ring pattern develops later for the thicker oxide layer, which indicates that a thickness (and fluence) dependent bulging of the oxide layer occurs here. After several nanoseconds, the Newton rings disappear due to the fragmentation of the ablated SiO_2 layer into flying particles and fragments.

Based on these results, Fig. 12 sketches the temporal evolution of the single fs-laser pulse induced ablation of thermally grown transparent SiO_2 layer from the underlying silicon carrier [72].

An important remark must be made here for the case of fs-laser ablation of extremely thin (native) oxide layers

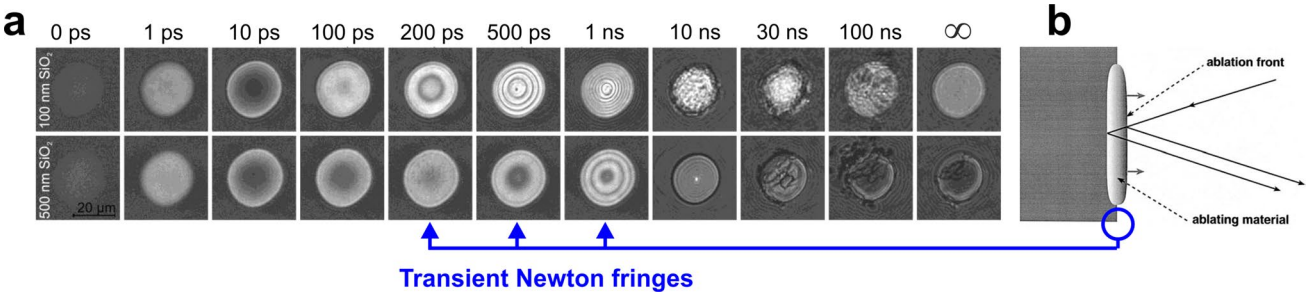

Fig. 11 Single fs-laser pulse ablation (1053 nm, 660 fs, 1.0 J/cm^2) of thermally grown SiO_2-oxide layers of different thicknesses ($h = 100$ nm, 500 nm; rows) from (100)-silicon wafers. **a** Pump-probe top-view brightfield reflectivity images (527—532 nm) of irradiated spots imaged for ten selected delay times $\Delta t = 0$ ps–100 ns as specified on top (columns) [72]. All images share the same scale bar provided in the bottom left image. Reprinted from [72], Physics Procedia, Vol. **41**, Rapp, S. et al., Physical mechanisms during fs laser ablation of thin SiO_2 films, 727–733, Copyright (2013), with permission from Elsevier. **b** Scheme of a semi-transparent laser-induced ablation layer with pronounced interfaces, giving rise to optical interference in the form of transient Newton fringes [8]. Reprinted from [8], Appl. Surf. Sci., Vol. **154–155**, von der Linde, D. and Sokolowski-Tinten, K., The physical mechanisms of short-pulse laser ablation, 1–10, Copyright (2000), with permission from Elsevier

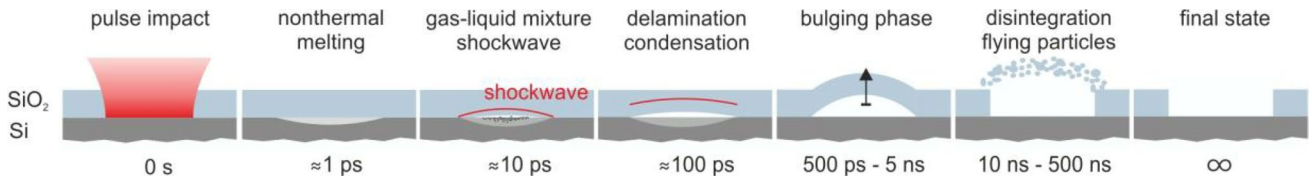

Fig. 12 Temporal evolution of physical processes during single fs-laser pulse ablation of a thin transparent oxide layer (SiO_2) from a semiconductor surface (Si wafer) [72]. Reprinted from [72], Physics Procedia, Vol. **41**, Rapp, S. et al., Physical mechanisms during fs laser ablation of thin SiO_2 films, 727–733, Copyright (2013), with permission from Elsevier

usually being present on semiconductor wafers, where a distinct fs-laser-induced ablation behavior is observed. Such native oxide layers typically exhibit a few nanometer thickness only. For silicon, they grow once the material is exposed to the ambient air environment and are self-limiting in thickness ($h \sim 3$ nm). Detailed post-irradiation analyses by *atomic force microscopy* (AFM) and *spectroscopic imaging ellipsometry* (SIE) proved that the single fs-laser pulse destruction threshold of the native oxide layers on silicon lies above the melting threshold of the semiconductor but below its ablation threshold [20, 78]. The effect is fully in line with thermodynamic considerations, where the enthalpy of decomposition of the native oxide layer lies above the enthalpy of melting of the semiconductor but below its enthalpy of evaporation [78]. In other words, the native oxide layer is thermally removed via indirect heating of the semiconductor underneath. This scenario was also directly confirmed by fs-TRM for germanium wafers through the observation of low-contrast transient Newton fringes manifesting at peak fluences $F_m \leq F_0 \leq F_{abl}$ below the ablation threshold of the semiconductor [79] and will be illustrated in the following.

Th effect is demonstrated in Fig. 13, which reveals the removal of the native oxide layer from a germanium wafer surface in the fluence regime of thermally melting the germanium through fs-TRM performed at delay times $\Delta t = 1$ ns and $\Delta t = 10$ ns (Fig. 13a) [79]. In this sub-ablative fluence range no crater is formed permanently at the germanium surface, in contrast to peak fluences F_0 exceeding the ablation threshold (Fig. 13b, compare the images labeled by "∞"). For both cases (fluences), Newton fringes can be seen at $\Delta t = 1$ ns. At the lower fluence ($F_0 = 0.63\ F_{abl}$, Fig. 13a) in the melting regime, re-solidification occurred almost completely after 10 ns, while at the higher fluences ($F_0 = 2.35\ F_{abl}$, Fig. 13b) the ablated material still reduces the reflectivity by screening the probe radiation from the surface. However, interference in the form of Newton fringes does not occur anymore since the layer initially ablated with sharp interfaces (Fig. 13c, 1 ns) started to disintegrate at the longer delay times (Fig. 13c, 10 ns). The disappearance of the spatial fringes in fs-TRM for high fluences and long delays can be attributed to the modification of the mass density profile of the ablating layer that is then featuring a decreased sharpness of the interfaces [79, 80], preventing the interference effect to occur.

The intrinsic geometrical asymmetry of a thin film-coated transparent carrier allows to distinguish between the two scenarios of fs-TRM in which the fs-laser excitation of the film by the pump beam is carried out through the air environment or through the transparent substrate, while the probe beam path is kept identical. Such a complementary approach, where the film is excited either through the air/film or the substrate/film interface, can reveal the dynamics of differences in the reflectivity contrast and through that allows to distinguish ultrafast (non-thermal) electronic material changes from significantly slower thermal modification effects or even from mechanical deformation, e.g., through thermal melting, shock wave propagation, blister formation, etc. Moreover, the substrate-side irradiation geometry is relevant for applications such as *laser-induce forward transfer*, LIFT (see Sect. 4.4).

For this reason, Domke et al. studied in detail the ablation of 470 nm thick, highly absorbing metal (Mo) films on transparent glass substrates through fs-TRM upon both, film-side and substrate-side fs-laser pulse excitation (1053 nm, 660 fs) employing peak fluences between 0.5 and 1.0 J/cm^2 [81]. Their time- and space-resolved observations in the glass-side irradiation scenario revealed *phase-explosion*, generating a liquid–gas mixture in the Mo/glass interface approximately ten picoseconds after the impact of the pump laser pulse, as the driving mechanism behind the lift-off of a coin-shaped Mo-film disk. Subsequently, a shock wave and gas expansion cause the Mo-film to bulge and form a blister at the Mo/glass interface, while the enclosed liquid–gas mixture cools and may condense at delay times in the hundreds of picosecond range. The bulging of the Mo-film to heights up to ~ 1.4 µm emerges for approximately twenty nanoseconds, until an intact Mo disk of a few tens of micrometers in diameter shears and lifts off at a velocity of ~ 70 m/s, leaving behind a pronounced hole in the film, without significant debris or any substrate material damage [81].

Except transient non-thermal, subsequent thermodynamic, or mechanical effects, also active optical emission may transiently occur in thin films during its

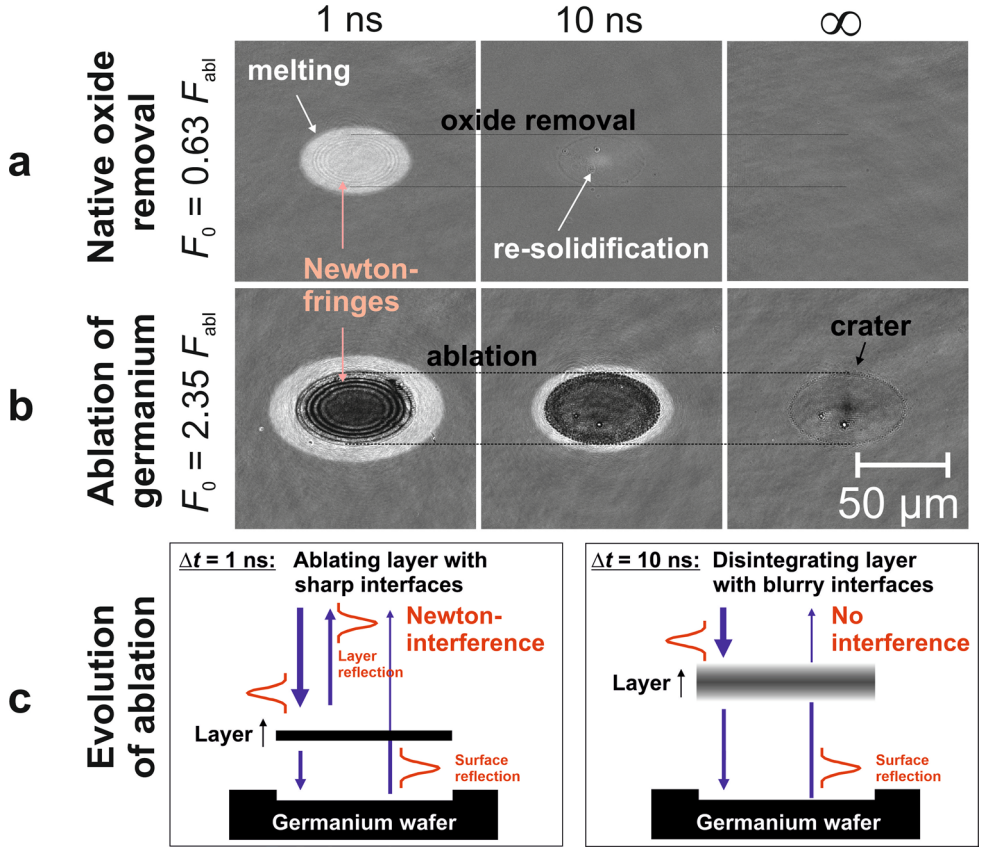

Fig. 13 Single fs-laser pulse irradiation (800 nm, 130 fs) of a germanium wafer surface. **a** Pump-probe top-view brightfield reflectivity images (400 nm) taken at delay times of 1 ns and 10 ns for spots irradiated at a peak fluence ($F_0 = 0.63\ F_{abl}$) sufficient to melt the material and to remove the oxide layer but not for ablative crater formation. **b** Pump-probe top-view brightfield reflectivity images (400 nm) taken at delay times of 1 ns and 10 ns for spots irradiated at a peak fluence ($F_0 = 2.35\ F_{abl}$) sufficient to ablate the germanium, eventually leading to a permanent crater at the surface (∞). Data in (**a**,**b**) are taken from [79] and share the same reflectivity (greytone) scale and the scale bar provided in the bottom right image. Characteristic processes are marked by arrows and horizontal lines. Reprinted figures (**a**, **b**) with permission from Bonse, J. et al., Phys. Rev. B, **74**, 134106, 2006. Copyright (2006) by the American Physical Society. **c** Scheme of the dynamics of fs-laser ablation, visualizing the state of the ablating layer and the implications for Newton interference effects at delay times of 1 ns and 10 ns, respectively. Layer dimensions, positions, and the spatial pulse extent in (**c**) are not to scale

ultrashort-pulsed removal. This was demonstrated by Sokolowski-Tinten et al., who studied optical damage and *fracto-emission effects* upon irradiation of 60 nm thick amorphous diamond-like carbon films on glass or silicon wafers upon irradiation with single fs-pulses of an amplified colliding-pulse mode-locked rhodamine 6G dye laser (620 nm, 120 fs) [82]. The effect is exemplified in Fig. 14 via a collage of top-view brightfield optical micrographs (left column) and corresponding wavelength integrated self-emission images (right column) assembled for irradiation at four different peak fluences ranging between 0.27 J/cm^2 (top) and 0.35 J/cm^2 (bottom). At higher peak fluences exceeding 0.4 J/cm^2, no fragmentation or fracto-emission was observed in the center of the laser-excited region [82], but instead the material-independent universal ablation behavior previously described in Fig. 13b.

It is evident that the laser-irradiated but non-removed film fragments still attached in border of the ablated hole area exhibit a strong optical emission. Optical filters indicated broadband emission from the blue into the near infrared spectral range. The temporal evolution of the optical emission was analyzed by replacing the imaging CCD-camera with a spatially integrating photodiode-oscilloscope detection system. The measurements (data not shown here for brevity) identified a weak but "fast" emission on the 100–200 ns time scale followed by a much stronger but "slower" main emission peaked around 0.5–1 µs that can be associated with ~ 90% of the totally emitted light [82]. The results revealed that the optical emission occurs mainly after fracture of the thin film and the re-arrangement of its fragments. Emission from a laser-generated free-electron plasma or ablation plasma could be safely excluded. Instead, the authors proposed that the optical emission can be explained

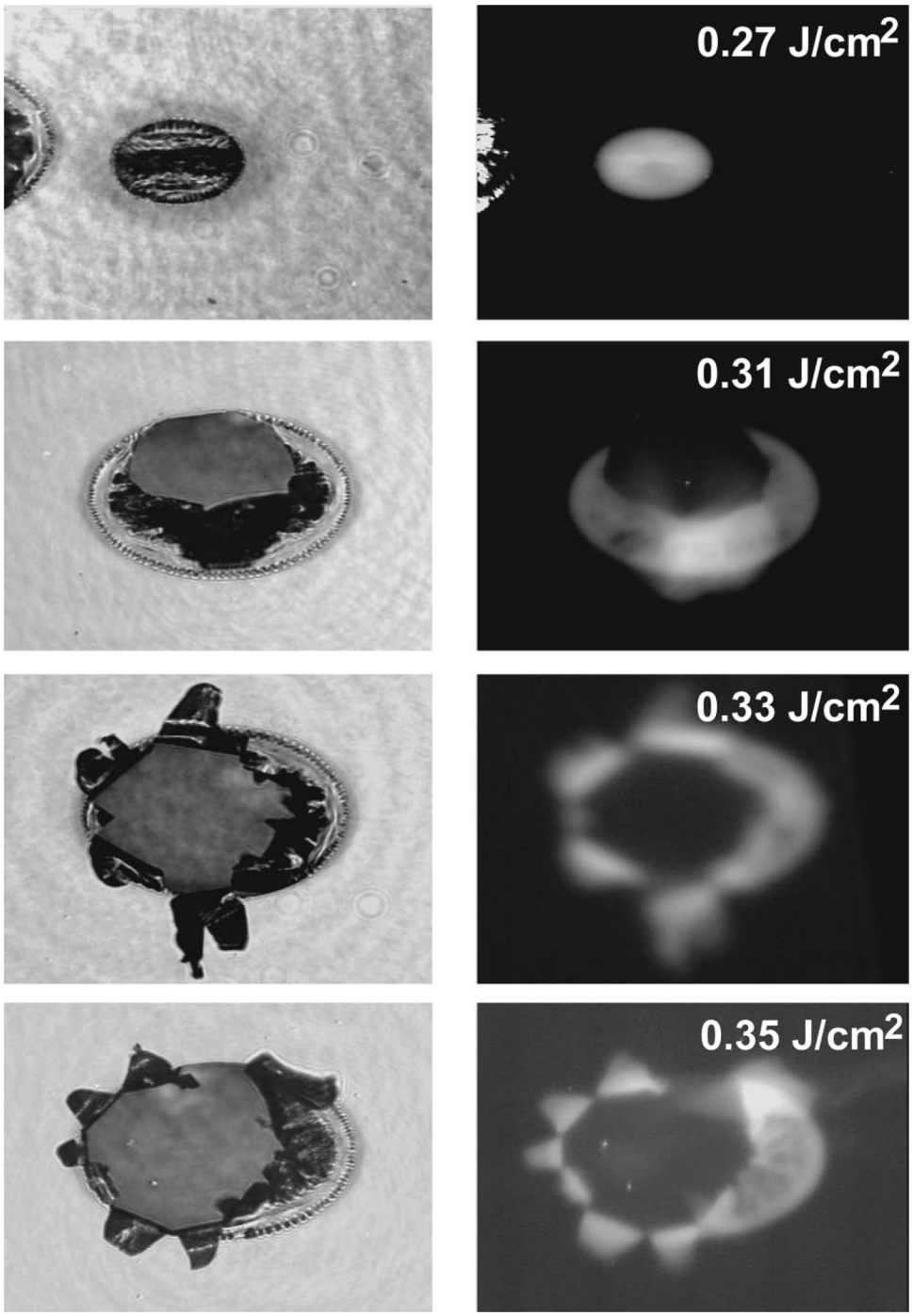

Fig. 14 Single fs-laser pulse ablation (620 nm, 120 fs) of a 60 nm thick amorphous diamond-like carbon layer [82]. Left panel: Top-view brightfield optical micrographs of spots irradiated at peak fluences of 0.27 J/cm^2, 0.31 J/cm^2, 0.33 J/cm^2, and 0.35 J/cm^2, respectively. Right panel: Corresponding wavelength-integrated self-emission images of a CCD-camera. All frames represent 270 × 190 µm^2 surface areas. Reprinted from Sokolowski-Tinten, K. et al., Short-pulse-laser-induced optical damage and fracto-emission of amorphous, diamond-like carbon films, Appl. Phys. Lett. **86**:121911 (2005), with the permission of AIP Publishing

by the high internal compressive stress of the order of a few GPa in the films caused by the employed pulsed laser deposition process. The fs-laser-induced impulsive and isochoric heating sufficiently reduces the adhesion forces to the substrate and, thus, the film is removed from the substrate without transition to the gas phase. The internal mechanical stress causes also the destruction of the film and the ejection of its fragments. The authors suggested that the early emission peak can be associated with the initial detachment and breakup of the film, while the slower emission component may be related to the final relaxation of the internal stress after the formation of the individual film fragments [82].

Except transient non-thermal, subsequent thermodynamic, or mechanical effects, also active optical emission may transiently occur in thin films during its ultrashort-pulsed removal. This was demonstrated by Sokolowski-Tinten et al., who studied optical damage and *fracto-emission effects* upon irradiation of 60 nm thick amorphous

diamond-like carbon films on glass or silicon wafers upon irradiation with single fs-pulses of an amplified colliding-pulse mode-locked rhodamine 6G dye laser (620 nm, 120 fs) [82]. The effect is exemplified in Fig. 14 via a collage of top-view brightfield optical micrographs (left column) and corresponding wavelength integrated self-emission images (right column) assembled for irradiation at four different peak fluences ranging between 0.27 J/cm^2 (top) and 0.35 J/cm^2 (bottom). At higher peak fluences exceeding 0.4 J/cm^2, no fragmentation or fracto-emission was observed in the center of the laser-excited region [82], but instead the material-independent universal ablation behavior previously described in Fig. 13b.

These examples show that a plethora of complex physical processes can transiently manifest during the structuring of thin films by ultrashort laser pulses. However, additional chemical or structural changes of the films may take place between successive laser pulses hitting the irradiated material. An obvious inter-pulse *chemical effect* is the laser-induced oxidation that may occur if the fs-laser irradiation is conducted in the ambient air since the laser-heated surface meets a reactive chemical environment. Such laser-induced effects were explored in detail around the turn of the millenium for the fs-laser irradiation of TiN hardcoatings as used for improving the lifetime of mechanical tools [3, 17, 18]. It was found that a specific sub-ablative laser fluence range exists in which the TiN is transferred into sub-stoichiometric TiO_{2-x}. Ion-sputter depth-profiling revealed in combination with *X-ray photo-electron spectroscopy* (XPS) [17] and spectroscopic *Auger electron microscopy* (AEM) [17, 18] that the TiN film material may be chemically altered up to a depth of a few hundreds of nanometers below the residual film surface upon multi-pulse fs-laser processing.

In the following, we want to exemplify another inter-pulse *structural effect* that was observed upon single fs-laser pulse irradiation (790 nm, 35 fs) of ~ 0.9 µm thick hydrogenated amorphous carbon films (a-C:H) that were deposited by chemical vapor deposition on 300 µm thick (111)-silicon wafer substrates [83]. Such a-C:H films typically contain 15—20% (at.) of sp^3 hybridized carbon. The optical penetration depth at the laser wavelength was evaluated through ellipsometric measurements and accounts to $1/\alpha \sim 380$ nm for the pristine a-C:H films. A series of irradiation spots was generated at the film using different peak laser fluences between ~ 0.2 and ~ 0.4 J/cm^2 and subsequently characterized by *optical microscopy* (OM), *white light interference microscopy* (WLIM), *micro Raman spectroscopy* (µ-RS), and microscale mechanical indentation tests for evaluating the microscopic, topographical, structural, and mechanical properties after the fs-laser treatment.

Figure 15 demonstrates by combining results of OM, WLIM, and µ-RS that structural changes can be generated through laser-induced graphitization in the film material at

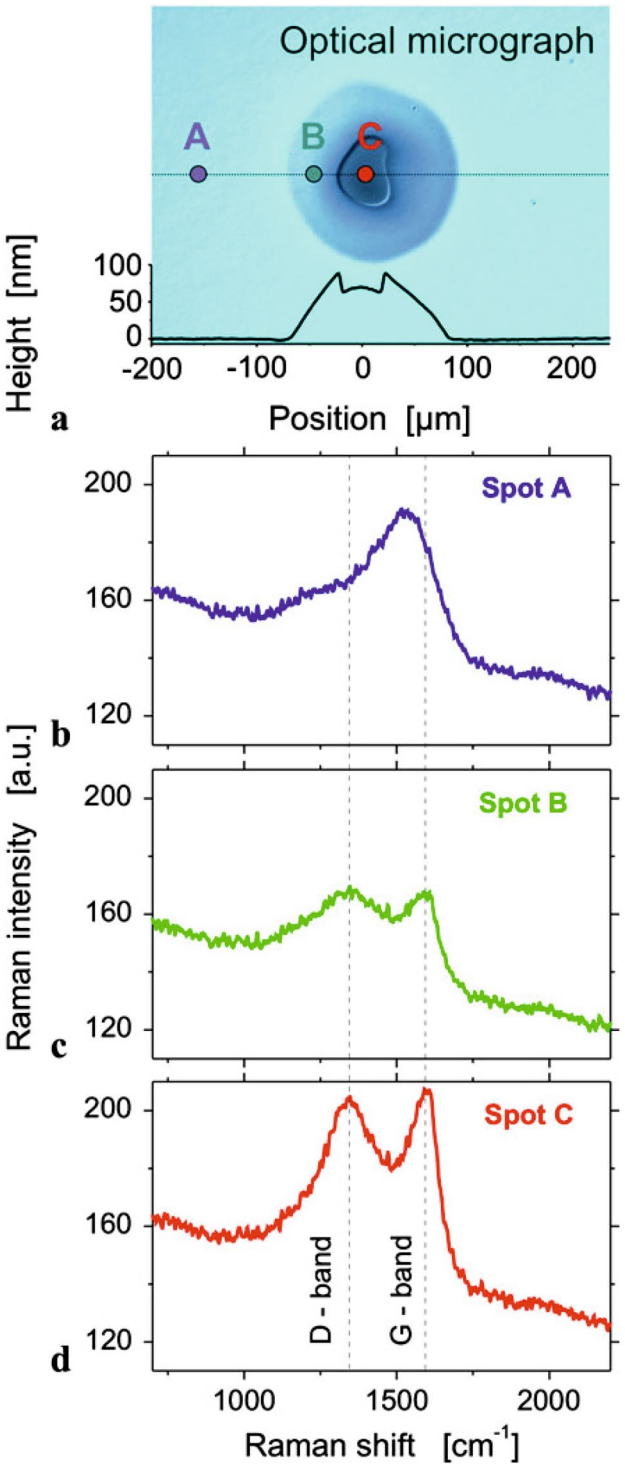

Fig. 15 Single fs-laser pulse irradiation of a surface spot (peak fluence $F_0 = 0.29$ J/cm^2) on a ~ 0.9 µm thick a-C:H film on silicon [83]. **a** Top-view optical micrograph with the corresponding white light interference microscopy surface height profile. **b** Reference spectrum from the non-irradiated surface location (A). **c**, **d** Micro Raman spectra obtained from different locations (B and C) within the fs-laser-irradiated spot. The positions of two characteristic Raman bands (D: "disorder" and G: "graphite") are indicated as vertical dashed lines. Reprinted from [83] by permission from Springer-Verlag: Applied Physics A **112**:9–14 (Femtosecond laser pulse irradiation effects on thin hydrogenated amorphous carbon layers, Bonse, J. et al.), Copyright (2012)

laser fluences below the ablation threshold. In Fig. 15a, a top-view differential interference contrast optical micrograph is provided along with a superimposed cross-sectional WLIM topography profile at the bottom. An ablation depth of ~ 25 nm of the film material is evident in the center of the irradiated spot, surrounded by a region that is protruding up to ~ 90 nm above the original film surface plane. Figure 15c, d provides μ-RS spectra taken at different locations in the fs-laser-irradiated spot (labeled "B" and "C" in Fig. 15a) along with a reference spectrum of the non-irradiated surface (Fig. 15b, recorded at spot "A").

The characteristic signature of the so-called D- and G-bands of the nanocrystalline carbon system is visible in all Raman spectra, with broad peaks located around ~ 1350 cm^{-1} (D) and ~ 1600 cm^{-1} (G) here. Due to the fs-laser irradiation, the Raman signal intensity ratio I(D)/I(G) of the two bands increases toward the center of the fs-laser-irradiated spot (see Fig. 15c, d). At the same time, the spectral width of both bands decreases, indicating a higher degree of structural order in the laser-modified areas. Both is indicative of a fs-laser-induced graphitization of the a-C:H material, i.e., a decrease of the sp^3 and an increase of the sp^2 fraction in the films. This explains also the swelling of the film material observed in the WLIM topography through a reduced specific mass density. A breakage of the sample through a suitable spot and subsequent cross-sectional inspection in SEM confirmed that no delamination occurred at the film/substrate interface in the laser-irradiated regions here. Thus, a blister formation could be ruled out and it was concluded that the elevated film surface topographies were solely generated by structural material changes in the film material [83]. The fs-laser-induced graphitization was further confirmed by complementary mechanical indentation measurements that indicated a significantly reduced material hardness (~50%) in the irradiated regions, as expected by a reduced content of sp^3 hybridized carbon [83].

3.3.2 Thick films: bulk damage through interference effects

The ablation of thick films is usually dominated by other effects if $h >$ Rayleigh length (DOF) $> \lambda$ is fulfilled. Particularly for strong absorbing materials such as metals and semiconductors, it is clear that in the limit of very thick films ($h \gg \lambda$, DOF) the processing/ablation must be identical to that of the corresponding bulk material (as already revealed in Sect. 3.2). However, for (semi-)transparent materials, if the film thickness is of the order of the wavelength and smaller than the Rayleigh length (DOF $> h \geq \lambda$), another often neglected intra-film interference effect may affect and limit the film ablation for specific film/substrate combinations, as it will be detailed in the following.

To the best of our knowledge, the intra-film interference effect was reported first in the context of laser-material processing in 2001 in post-irradiation experiments of a Japanese group studying the single-pulse ablation of ~ 15 μm thick organic m-MTDATA films (amorphous substituted triphenylamine: 4,4′,4″-tris(3-methylphenyl phenylamino) triphenylamine) being transparent for the laser irradiation wavelength (780 nm, 170 fs) from the surface of quartz substrates [84]. In stylus-profilometric measurements, the authors observed fluence dependent step-like crater profiles as reprinted in Fig. 16a. The authors proposed an interference effect, where the front part of the fs-laser pulse is partially reflected at the interface between the organic film and the quartz substrate and can interfere with its following tail. Hence, a standing light wave is formed transiently within the film along the light propagation direction, exhibiting maxima at a spatial separation of $d = \lambda/(2n)$. For the refractive index $n \sim 2$ of the m-MTDATA polymer film material, d is expected to be ~ 195 nm here, reasonably supported by the step-height data derived from the crater profiles presented in Fig. 16b.

About four years later, the same standing light-wave based mechanisms was identified to manifest in *in-situ*

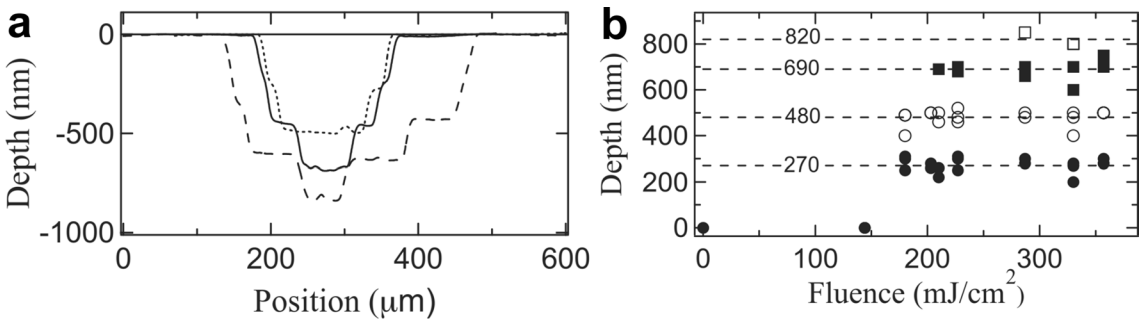

Fig. 16 Stylus profilometric measurements of single-pulse irradiation of organic m-MTDATA films by Ti:sapphire fs-laser pulses [84]. **a** Cross-sectional profiles at three different fluences of 0.20 J/cm^2 (dotted line), 0.23 J/cm^2 (solid line), and 0.29 J/cm^2 (dashed line). **b** Depth of ablation steps as a function of the peak fluence. Reproduced from Hosokawa, Y. et al. [84], with permission from Japan Laser Processing Society

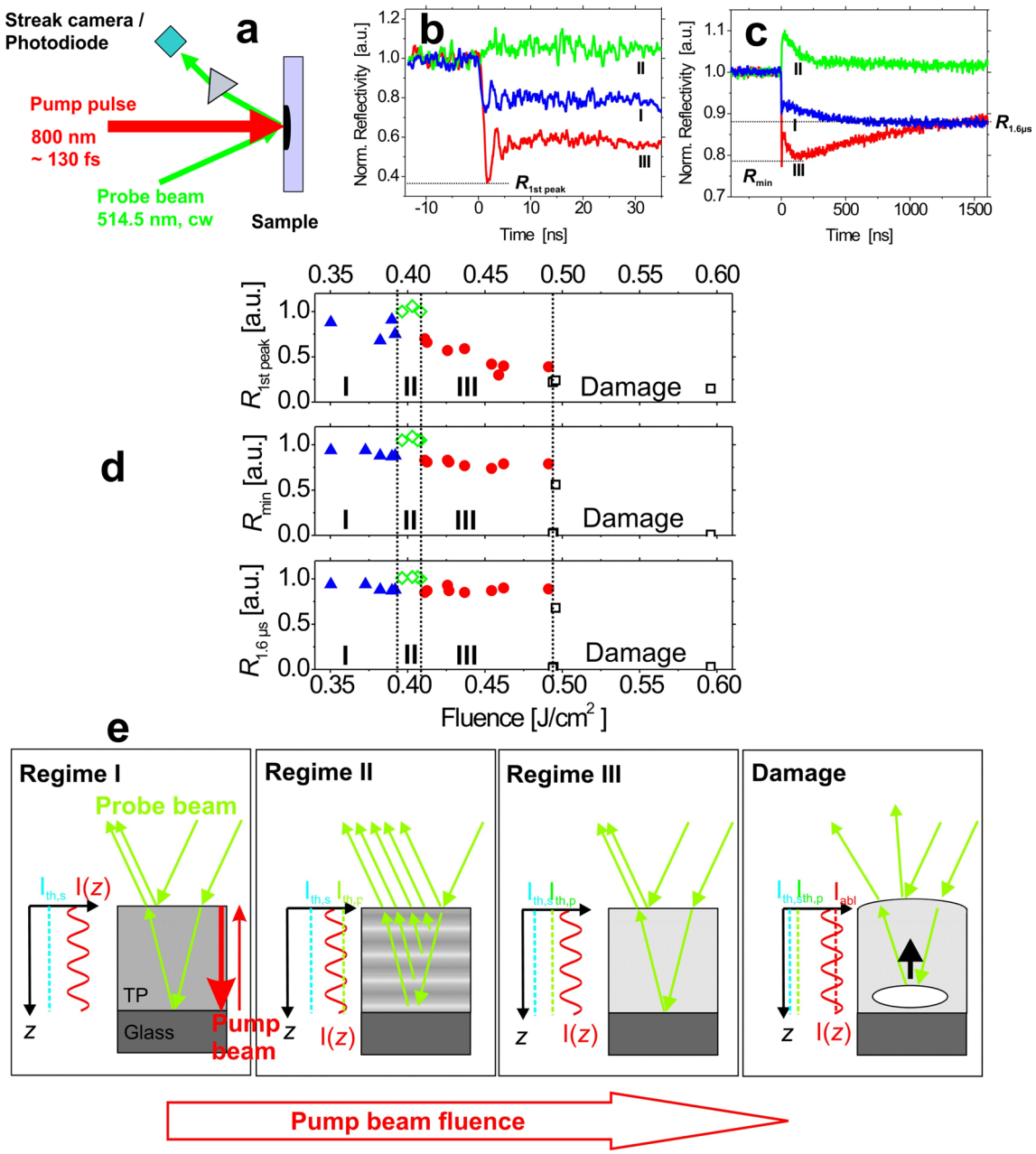

Fig. 17 Time-resolved reflectivity measurements during single-pulse fs-laser irradiation of ~ 1 µm thick triazenepolymer films [61, 86]. **a** Experimental setup. **b**, **c** Normalized reflectivity transients recorded at three different peak fluences below the damage threshold: I – 0.39 J/cm^2 ≈ 0.79 × F_{th}, II – 0.40 J/cm^2 ≈ 0.81 × F_{th}, III – 0.49 J/cm^2 ≈ 0.98 × F_{th}. **d** Normalized reflectivity of the first peak ($R_{1st\ peak}$, streak camera), minimum (R_{min}, photodiode), and value after 1.6 µs ($R_{1.6\ µs}$, photodiode) as function of the fs-laser fluence. **e** Interference-based intra-film laser damage model. The fluence of the irradiating (pump) fs-laser beam increases from the left to the right. Reprinted from Bonse, J. et al. [86], Damage mechanisms in polymers upon NIR femtosecond pulse laser irradiation: sub-threshold processes and their implications for laser safety applications, AIP Conf. Proc. **1278**:56–64 (2010), with the permission of AIP Publishing

time-resolved reflectivity measurements during the fs-laser irradiation of ~ 1 µm thick triazenepolymer (TP) films on glass substrates [61, 85]. The effect is responsible for the intricate reflectivity behavior observed only in a very narrow fluence range below the permanent film damage threshold, as detailed in the following. Figure 17a sketches the experimental setup of the real-time resolved reflectivity measurements. Single fs-laser pulses (800 nm, 130 fs) are focused under normal incidence to the TP-films in *substrate geometry* to a beam spot diameter ($1/e^2$) of ~ 100 µm [86]. The probing cw-radiation of a single-mode 514.5 nm Ar-ion laser is focused to a ~ 30 µm spot in the center of the

fs-laser-irradiated spot at an angle of incidence of θ = 18°. The reflected and re-collimated and spectrally cleaned probe beam is simultaneously monitored on short and long time scales via a combination of a streak-camera (time window 50 ns, sub-ns resolution) and a photodiode (time window 2 µs, few ns resolution).

Figure 17b, c exemplify three typical transients of the normalized reflectivity change $\Delta R/R_0$ (normalized with the reflectivity value R_0 of the non-excited film) for three different peak fluences below the value of the single-pulse damage threshold of the film ($F_{th} = 0.5$ J/cm^2). Above that threshold fluence complex and rather chaotic transient reflectivity changes are emerging (data not shown here; for details see [61, 85]). Below the damage threshold, generally the reflectivity rapidly drops to a minimum ($R_{1st\ peak}$, see curves I to III in Fig. 17b) before recovering to the initial surface reflectivity ($\Delta R/R_0 = 0$) on the microsecond and millisecond time scale. For peak fluences close to the damage threshold, a second reflectivity minimum (R_{min}, see curve III in Fig. 17c) may be observed on the sub-microsecond time scale. Interestingly, in a very narrow fluence range, the reflectivity is transiently increased (see curves II). This becomes visible when plotting the three characteristic normalized reflectivity values $R_{1st\ peak}$, R_{min}, and $R_{1.6\ \mu s}$ as a function of the peak laser fluence in Fig. 17d, see regime II. The reflectivity increase can be explained by a transient intra-film Bragg-grating that is formed at a suitable fluence when the standing light wave modifies the refractive index of the polymer just at its intensity maxima being spaced at $d = \lambda/(2n)$, see the explanatory scheme in Fig. 17d [86]. The coherently superimposed Fresnel reflections from the equidistant spatial refractive index modulations can then constructively interfere in the direction of the probe beam featuring a transient Fabry–Perot mirror effect here.

In 2014, a Canadian group transferred this concept of *"light sheet ablation"* (see Fig. 18) to inorganic materials and systematically explored the effect for SiN_x films with thicknesses varying between 0.02 and 1.5 µm deposited on silicon wafers and for various ultrashort-laser wavelengths [87, 88]. Remarkable narrow intra-film damage regions of a few tens of nanometers depth only can be reached through the involvement of nonlinear absorption effects triggered by the ultrashort laser pulses (522 nm, 200 fs) along with a few micrometer confined circular top-hat profile (Fig. 18).

Finally, some general aspects of the interference-based intra-film structuring mechanism should be summarized: (i) Only films with thicknesses $h > \lambda/(2n)$ are showing this effect. (ii) Spatial confinement of the standing light wave pattern must be supported by a suitable ratio between the Rayleigh length and the film thickness (DOF > h). (iii) Temporal confinement must be enabled, i.e., the coherence of the laser beam should be sufficiently large to allow forming the intra-film standing light wave. (iv) The effect manifests only in specific fluence windows, where material modifications form selectively at the maxima of the standing light wave. In case the ablation threshold is locally exceeded, the film can disintegrate through the removal of some of the topmost intra-film segments, potentially leaving behind some blistered sub-surface regions. (v) A highly reflective substrate material and a spatial top-hat laser beam profile may help

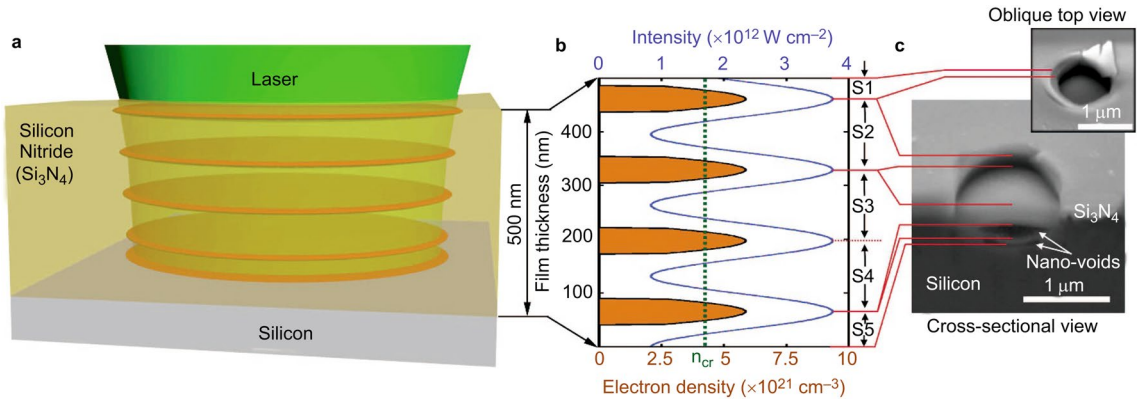

Fig. 18 **a** Scheme of light sheet ablation of a 500 nm thick transparent silicon nitride film on silicon, sketching the segmentation of the focal interaction volume of the incident 522 nm laser radiation through several thin interaction zones (orange discs) as a result of the interference of Fresnel reflection of the incident light from the film/substrate interface. **b** The modulated intensity profile (solid line) calculated for a Gaussian-shaped beam of ~ 1 µm (1/e^2) diameter along with the electron density profile (orange shaded) expected inside the film at the exposure of 9 × 10^{12} W/cm^2 average incident intensity. The electron density exceeds the critical plasma density (n_{cr}) at the interference maxima positions, manifesting in the intra-film structuring simultaneously observed in scanning electron micrographs in **(c)**. The irradiation results in the ejection of film segments S1 and S2, and the blistering of the segments S3 and S4 to form a nanovoid at the fourth fringe maximum, and blistering of segment S5 overlying a second nanovoid. As indicated by red lines, the positions of the cleavage planes align with the fringe maxima positions [87]. Reprinted from [87] by permission from Springer Nature: Light: Sci. Appl. **3**:e157 (Quantized structuring of transparent films with femtosecond laser interference, Kumar, K. et al.), Copyright (2014)

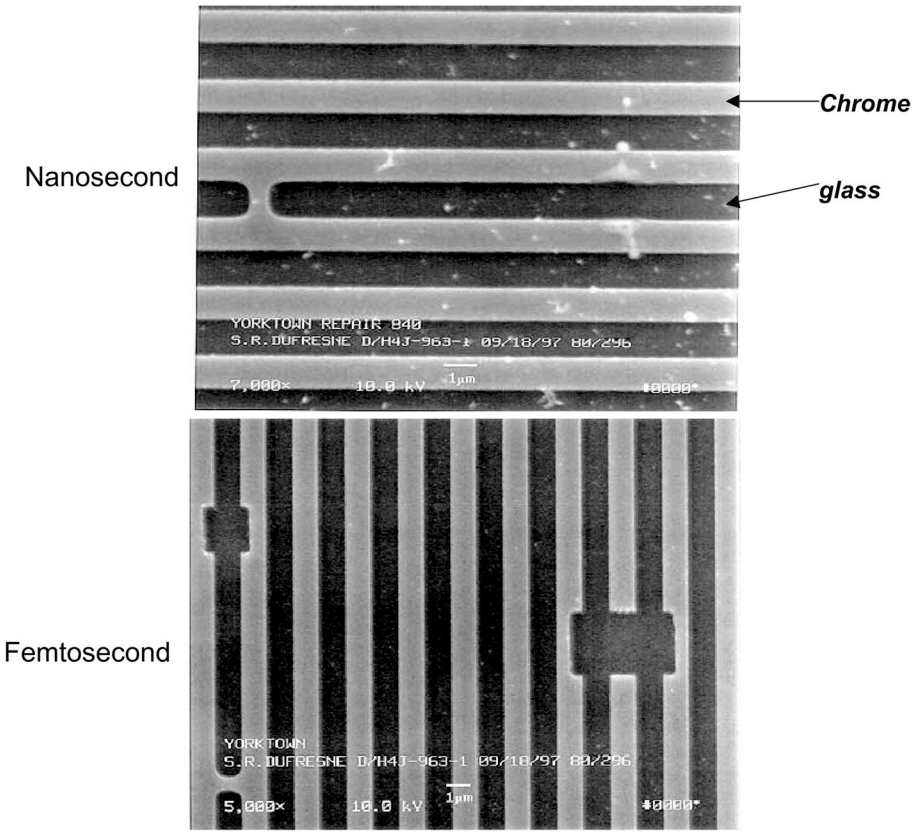

Fig. 19 Top-view SEM micrographs of IBM photomasks repaired with ns-laser pulses (top) and fs-laser pulses (bottom) using the MARS I system [89], High resolution material ablation and deposition with femtosecond lasers and applications to photomask repair, Haight, R. et al., J. Mod. Opt. **51**:2781–2796 (2004), reprinted by permission of the publisher (Taylor & Francis Ltd, http://www.tandfonline.com)

to optimize the interference contrasts and, thus widen the observed fluence window. (vi) The effect occurs only if a sufficient part of the laser pulse energy is being reflected at the film/substrate interface. Thus, the linear transparency regime of the film material is favored but an interplay with nonlinear absorption or incubation effects at the intensity maxima may help to confine the damage regions to very thin "light sheets". (vii) The intra-film interference effect may prevent that the films can be completely ablated from the substrate material [85].

4 Applications

4.1 Repair of photolithography masks

Due to an increasing demand of highly integrated semiconductor circuits and the simultaneous decrease of their structural sizes, suitable tools for photolithographic mask repair are needed by the semiconductor industry. Binary photolithographic masks are typically consisting of metallic chromium (Cr) films of ~ 100 nm thickness on quartz substrates. Defects on the photolithographic masks often manifest in the form of excess absorber (Cr). A transfer of the pattern to the wafer would then result in wafer-level wiring errors which render the integrated circuit inoperative. Since the manufacturing process of a photolithographic mask is very expensive, a defect removal is highly desirable [89] and the relatively high cost for a fs-laser system can be afforded.

Usually, the repair of these binary photomasks is done by the focused ion beam (FIB) technique which has a high lateral resolution but is limited by the ion-induced damage of the quartz substrate. To overcome this drawback, two concepts of fs-laser-based optical mask-repair systems have been realized first by two companies in 1998/1999, employing a *far-field* [90] and a *near-field* [91] based structuring technique. Both methods take benefit from the substantially different ablation threshold fluences of chromium films and the underlying dielectric material, i.e., F_{abl} (Cr) < F_{abl} (quartz).

The *near-field structuring* of chrome films was realized by Liebermann et al. (Nanonics Lithography Ltd.) by coupling the third harmonic of Ti:sapphire femtosecond laser pulses (260 nm) into a light guiding hollow, micropipette (chromium coated fused silica, aperture diameter ~ 400 nm) which was used then in the scanning near-field mode [91]. Laterally protruding excess chrome defects with sizes of 3 μm were carved-off from a 100 nm thick Cr-layer with an accuracy of approximately 50 nm.

The *far-field structuring* technique was realized by Haight et al. (IBM) imaging a movable rectangular aperture (projection mask) placed in the beam of a femtosecond oscillator

(800 nm, 100 fs) directly to the sample surface (photomask: Cr on glass) [90, 92]. For that purpose, a high numerical aperture objective was used (projection mask demagnification factor 100). Sub-diffraction limited ablation spot sizes were realized capable to remove 600 nm wide mask defects. The first generation of this device (Mask Repair System, MARS I) was installed in April 1998 in IBM's Burlington Mask House for routine manufacturing operation [92]. Figure 19 compares the repair of a 100 nm thick Cr-film on glass based binary mask with nanosecond laser pulses (top micrograph) and with fs-laser pulses (bottom micrograph) employing the MARS I system [89]. In the top SEM micrograph (ns-repair), a bridge of chromium connecting two horizontal chromium lines was removed, resulting in some redeposited chromium particles evident throughout the entire picture. For direct comparison, the bottom SEM micrograph (fs-repair) displays a photomask region that was ablated with a 100-fs laser in a square-shaped and a rectangular area. Very sharp chromium edges and no debris or metal splatter are evident, demonstrating the superior quality of the mask repair through ultrashort fs-laser pulses compared to longer ns-laser pulses.

The second generation of the mask repair system (MARS II) has been installed in late 2001 as IBM's primary repair tool for 248 nm and 193 nm wavelength chrome on glass phase shift photolithographic masks [93]. In this system, a frequency-tripled Ti:sapphire femtosecond laser beam (260 nm, 100 fs, 1 kHz) is focused to a diffraction limited 150 nm Gaussian spot and scanned over the defect to remove it. An ablation resolution of 80 nm together with an increased flexibility in ablating complex structures were demonstrated. Mask features were trimmed to a root-mean-square precision of ~ 5 nm [93].

Later, the experiments at IBM were extended to generate sub-200-nm fs-laser radiation, using a regeneratively amplified Ti:sapphire system (800 nm, 30 fs pulses 1 mJ, 1 kHz) [94]. After frequency-doubling the fundamental Ti:sapphire laser radiation to 400 nm, the laser pulses passed through an appropriate delay line and were mixed with remaining 800 nm light in a hollow-core glass fiber resident inside an argon-gas-filled cell, finally converting the ultrashort pulsed input radiation via sum- and difference-frequency mixing into wavelengths around 160 nm, 193 nm, and 266 nm. After spectral separation, pulse energies up to 0.5 µJ were realized at 193 nm wavelength, confined in ~ 30 fs pulse duration. As for the ablation using 266 nm wavelength (100 fs) pulses, the chromium layer was completely removed without any observable damage to the underlying fused silica substrate, while the shorter 193 nm wavelength bear the potential of further improved laser processing precision [94].

4.2 Laser cleaning

Laser cleaning with the aim of removing an (unwanted) thin (or even thick) film or contaminants from a surface without damaging the latter was already reported about 50 years ago. In this context, questions of the restoration of cultural assets were addressed [95]. This seems surprising only at first glance. Due to possible aggressive environmental conditions, the preservation of cultural assets is often a race against time. Hence, a reliable non-contact method like laser processing is highly welcome [96]. Thin films in that respect have thicknesses up to the order of 100 µm as in the case of total paint film thicknesses in the aircraft and automotive industry. In restoration, e.g., aged varnishes, overpaintings, or encrustations are typically involved. Here, the thickness range covers both thin (< 100 µm) and thick films (> 100 µm) up to the millimeter domain.

The general principle of laser cleaning to uncover buried surfaces by means of laser radiation is based on the selective absorption of laser radiation in the surface-covering layer to be removed (compare *substrate geometry* in Fig. 1a). Cleaning is possible if the applied laser fluence can cause an ablation process of the layer. This happens when the energy absorbed per unit volume minus the losses (e.g., due to heat conduction for longer laser pulses) is above a material-dependent fluence threshold value. For thin films, the ablation threshold might depend on the film thickness (see Sect. 3.2.1).

A promising situation for laser cleaning is when the optical and thermal properties of the contamination layer and the object to be preserved are very different. This is the case, for example, when an absorbent (black) film should be removed from a highly reflective (white) substrate, e.g., for contaminated paper or parchment. Ideally, the object to be preserved should have significantly greater thermal resistance to the laser radiation than the film. The benefit of using lasers results from the facts that processing is done in a contact-less and site-controlled manner. The laser parameters (wavelength, pulse duration, repetition rate, focusing conditions, fluence) can be adapted to the specific laser cleaning application. Moreover, often there is the possibility of self-limiting of the process, i.e., one can reach an "etch stop" at the interface to the object. When applying a scan-processing approach, where a (focused) laser beam is moved across the sample surface, large surface areas can be cleaned from contaminants. Up-to-date laser and scanner technology enables efficient laser cleaning rates at the m^2/s level in an industrial environment [97].

Laser cleaning is not limited to cultural assets. It plays an important role for many technical applications when contaminations are to be removed or when the surface of workpieces must be prepared for further processing. Up to now, a large variety of objects and technical surfaces consisting

of diverse basic materials were treated with lasers emitting at various wavelengths in different pulse duration regimes. Here, only an excerpt from the extensive literature that is considered as representative can be briefly discussed.

Metal surfaces were cleaned from organic contaminants [98–101] and from paint coatings [102–104]. The latter has great application potential in the aircraft, automotive, and shipbuilding industry. The removal of a 20 µm thick zinc coating from steel was also reported [105]. And vice-versa, the cleaning of surfaces to allow for subsequent painting is discussed too, e.g., to prepare *carbon fiber reinforced polymer* (CFRP) surfaces [106].

Nowadays, laser cleaning can be considered as a well-established technique in the field of stone conservation. Cooper et al. demonstrated the capabilities of Nd:YAG nanosecond laser radiation to remove the black crust from a historic limestone sculpture. They also showed that the addition of a water layer prior to laser irradiation might be helpful for the removal of material [107]. The potential for practical laser graffiti-removal systems on the basis of Nd:YAG lasers was shown [108]. Undesired graffiti—as a cultural side effect—is a growing problem worldwide, affecting a large number of buildings and monuments worthy of conservation. Recently, femtosecond pulse laser cleaning was discussed in this context [109].

During the "early phase" of the application of laser cleaning, excimer lasers played an important role, e.g., for the restoration of paintings [110] and the processing of organic materials such as parchment [111] and paper [112]. However, the high photon energies of UV emitting lasers can lead to photochemical degradation of the cleaned objects [113] that often must be prevented. Hence, lasers emitting in the optical or infrared spectral range moved into the focus, particularly when the low-repetition rate gas-laser technology was replaced by high-repetition rate solid-state laser systems.

Since the turn of the millennium, also femtosecond lasers were explored for cleaning purposes. Initially, a specific problem within painting conservation, namely the removal of glue-paste adhesive from the reverse side of a painting on canvas, was addressed [114]. Ultrafast laser pulses in the femtosecond range, in some cases also with ultraviolet wavelength, were used for cleaning on a variety of objects from very different material classes, e.g., metals [115, 116], painted artifacts [117–119], granite [120], parchment [121], paper [122, 123], and wooden artworks [124].

Despite the multitude of options in the choice of laser irradiation parameters, including the availability of ultrashort laser pulse durations that enable a highly localized and precise material treatment, the surface cleaning of cultural heritage objects is still a delicate and often irreversible process. The optimization of the laser cleaning parameters for the object to be treated plays a major role to avoid any undesired side effects like, e.g., yellowing, discoloration or darkening [113, 125–127].

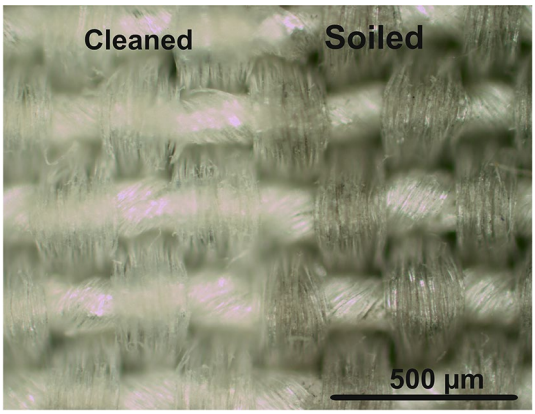

Fig. 20 Laser cleaning of soiled silk fabric (532 nm, 8 ns, 0.5 J/cm.^{2}, 500 Hz, ~ 2,500 pulses per spot). Optical micrograph of original area (right, soiled) and nanosecond laser-treated area (left, cleaned) [128]. Reprinted by permission from Springer-Verlag: Springer Proceedings in Physics **116**:321 (Determination of a working range for the laser cleaning of soiled silk, Krüger, J. et al.), Copyright (2007)

Generally, laser damage threshold fluences are higher for longer laser pulses, regardless of the irradiated type of object (compare Sects. 3.2.1 and 3.2.2). For a fixed laser wavelength, then the laser cleaning thresholds for the removal of the soiling or contamination should be lower than the damage thresholds for the objects independently on pulse duration. The “cleaning window”, i.e., the working range with respect to the laser fluence, for a successful laser cleaning procedure might be larger for longer (nanosecond) pulses than for ultrashort (femtosecond) laser pulses [122]. When the cleaning efficiency and quality is comparable in both cases (or even better for higher usable laser fluences in the nanosecond case and below the corresponding damage threshold of the object), then also the application of the longer laser pulses can be more reasonable. Figure 20 demonstrates the capabilities of laser cleaning through an optical micrograph that allows directly comparing an untreated soiled silk fabric region (right) with a Nd:YAG ns-laser cleaned silk area (left) [128].

A complementary “cleaning application” is enabled by the precision and minimal thermal damage (heat-affected zone) to the material in ultrashort pulse laser processing (see Sect. 2): often the precise cutting of cross-sections through delicate paint layers of artworks poses a major problem when using mechanical scalpels that are resulting in crumbling, delamination and compression of the paint layer. A Japanese group has demonstrated that this obstacle can be overcome when using a femtosecond laser to create controlled cross-sections of paint layers with minimal damage to the surrounding artwork [129]. The selection of the laser source for restorative applications should be based on

the principle that the cleaning success is also accompanied by a minimization of undesirable side effects. In individual cases, this may also mean that longer laser pulses are the better choice.

Finally, the question should be answered, where the ultimate limits are with respect to the laser-induced removal of extremely thin films and how small a laser-induced film perforation can be made? Here, we consider the thin films as "closed", i.e., a continuous layer of a certain material that is covering another material. Note that this situation is distinctively different from the *laser-induced desorption* of single atoms, molecules, or clusters from a bulk material surface through electronic excitation and sputtering effects [1, 130].

The above-mentioned question was addressed by Hartmann and co-workers within the frame of the DFG Priority Programme SPP 1327 *"Optically generated sub-100 nm structures for biomedical and technical applications"* of the German Research Foundation (DFG) [131]). The authors explored the nonlinear processing and multiphoton ablation of *self-assembled monolayers* (SAMs) for application as ultrathin resists and in biochemical sensors [132].

Figure 21 (top panel) summarizes their results obtained for the fluence dependence of the fs-laser-induced diameters d_{Si}, d_{rim}, $d_{ripples}$, and d_{SAM} of different surface topographic features observed at the sample surface for an octadecylsiloxane (ODS) self-assembled monolayer deposited on surface-oxidized silicon wafers after irradiation with single focused fs-laser pulses (800 nm, < 30 fs) [133]. The laser pulses were focused tightly to the sample in *substrate geometry* according to Fig. 1a using a Schwarzschild microscope objective with a numerical aperture $NA = 0.5$. Out of the different listed characteristic surface topography diameters,

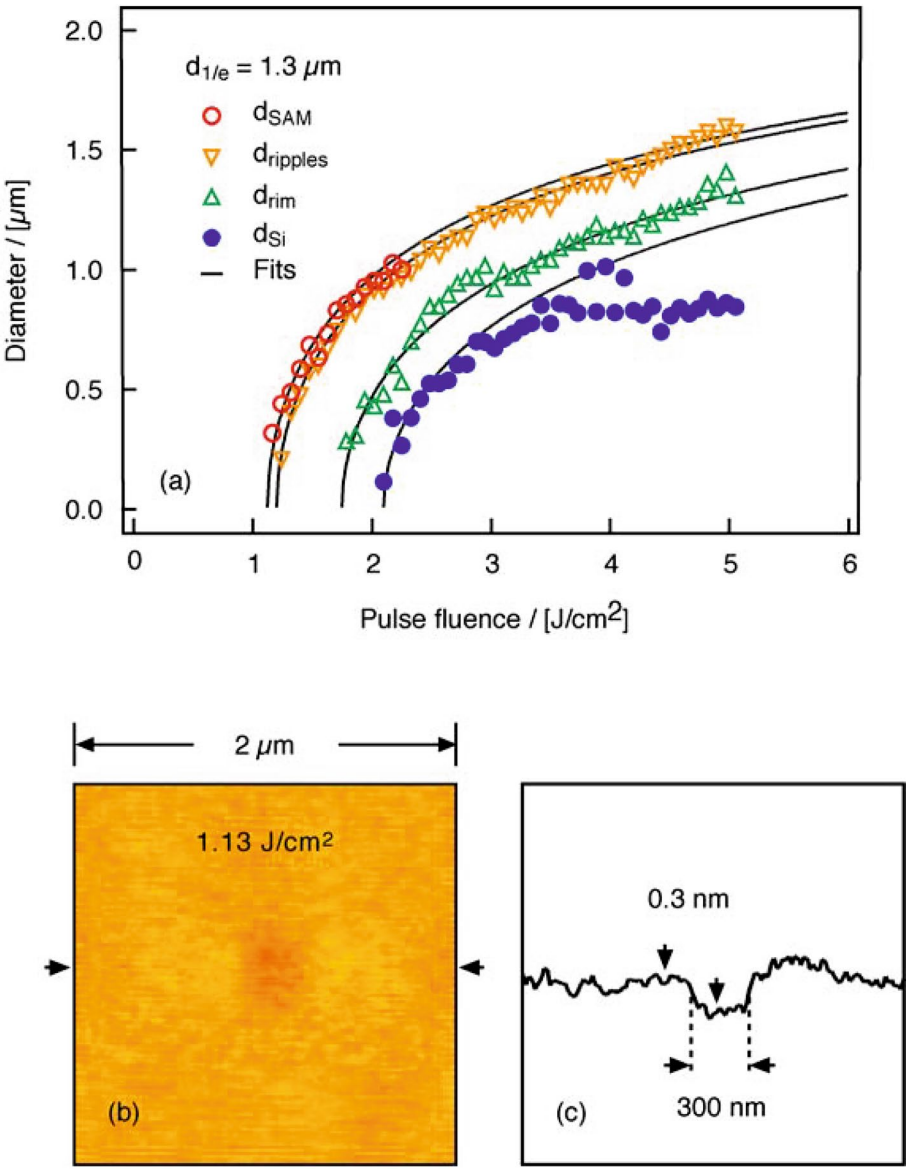

Fig. 21 Patterning of a self-assembled monolayer of octadecylsiloxane on surface-oxidized silicon substrates with single Ti:sapphire laser pulses (800 nm, < 30 fs) [133, 134]. **a** Variation of characteristic morphological diameters d_{Si}, d_{rim}, $d_{ripples}$, and d_{SAM} with the average laser fluence F. The black solid lines represent least-squares-fits to the function $d = d_{1/e} \times \sqrt{(F/F_{th})}$. **b** AFM-topography image at $F = 1.13$ J/cm^2. **c** Corresponding cross-sectional profile along the line marked by black arrows in **b**. Reprinted from [133] with permission

d_{SAM} denotes the ablation threshold of the ODS-SAM film, here. Minimum diameters for the selective laser processing of the ODS layer are ~ 300 nm, i.e., a direct sub-wavelength patterning close to λ/3 is feasible. Corresponding surface height profiles taken by *atomic force microscopy* (AFM) reveal crater depth of only 0.3 nm below the thickness of the ODS-SAM of typically h_{SAM} ~ 2 nm.

It can be concluded that under optimum conditions, a remarkable precision with sub-wavelength and sub-monolayer film alteration is feasible for thin film processing by ultrashort laser pulses.

4.3 Avoiding laser-damage of optical coatings

Another obvious application of thin films in interaction with laser pulses is the development of damage resistant optical coatings. The topic is as old as the experimental realization of the laser itself, since in 1960 Maiman used silver-coated ruby rods as laser resonator (see the introducing historical note of Soileau in Chapter 1 of Ref. [4]). Nowadays, in most cases the coatings consist of multi-layer stacks made of dielectric materials that are tailored for the targeted application, e.g., acting as high-reflective mirrors, for compensation of spectral phase shifts (chirp) for ultrashort pulses, etc. Such optimized coatings are key for the development of modern high-power laser systems on scientific or industrial levels. With meter-scale dimensions [135] they may be of relevance for peta- and exawatt large-scale laser facilities [136] and in future laser-fusion experiments.

Given this high technological relevance of the subject, a whole scientific community is studying the laser-induced damage of optical coatings for more than five decades already, as reflected through the traditional annual *Boulder Laser Damage Symposium*, first time organized in 1969 in the USA. Since 1984 *Round-Robin* laser damage test sequences are being organized and measurement methods for quantifying laser damage and its standardization are actively improved, as reflected through the international standards ISO 11254 developed in the 1990s [137, 138] and the more recent ISO 22154 dated from 2011 [139, 140].

The state-of-the-art knowledge about laser-induced damage in optical materials until the year 2015 was summarized in a comprehensive reference book edited by Ristau [4]. In the following section, we just highlight specific aspects being relevant for the ultrashort pulsed laser damage of thin film based optical coatings. For more details, the reader is referred to that book reference.

In various aspects, the damage of optical coatings upon ultrashort pulsed laser radiation (fs-ps duration) differs from that of short pulsed laser radiation with nanosecond durations or even longer. One reason lies in the high peak intensities that can be easily reached for ultrashort laser pulses at quite moderate pulse energies. Secondly, optical absorption, interference, and scattering effects take place on time scales before significant thermal processes and heat flows can manifest (see Sect. 3). Thus, two demands can be formulated as requirements for ultrashort pulsed laser radiation [4]:

i. The optical component has to be capable to handle peak powers up to the petawatt range. This refers to its damage threshold fluence but also to potential nonlinear effects triggered by the large peak powers/intensities.
ii. The optical components often require special optical properties, which are usually not necessary for longer pulse durations or continuous wave radiation. One important requirement is related to the ultrashort pulse durations that, according to the Fourier-transform limit, come with a certain minimum spectral bandwidth. Thus, the optical element must be able to properly manage all spectral components in a controlled manner. Important examples are pulse stretching or compressing elements, such as chirp-mirrors, or coated prisms, or gratings. Moreover, the large spectral bandwidth of fs-laser pulses generates additional difficulties for the design of non-phase-sensitive optical components like mirrors or windows.

According to Jupé et al. [141], the calculation of the damage threshold fluence of a complex multi-layer stack is based on three different and inter-dependent physical entities:

(1) The intrinsic damage threshold of the layer material. This material-specific threshold can be determined from the threshold $F_{th,layer}$ of a single layer and then be normalized by the electric field strength $|E|$ inside the single layer, according to: $F_{th,layer} \times |E| = \text{const.}$
(2) The sequence of layers and the electric field strength have to be considered. Note that both entities are influencing each other.
(3) The energy flux has to be considered for the calculation of the threshold characteristics in the layered stack and is affected by its refractive index profile.

Figure 22 exemplifies the energy flux (solid line, left abscissa) vs the thickness of the multi-layer system along with the refractive index profile of a standard high-reflective (HR) mirror made of alternating quarter-wave (λ/4) layers of SiO_2 (refractive index n ~ 1.5) and TiO_2 (n ~ 2.35) [141]. The laser-induced damage threshold (LIDT) of the entire optical coating is determined by the lowest internal LIDT. Damage is then observed at the interface between the first and second layers on the TiO_2 side, where the energy flux is maximum.

For the improvement of the damage threshold fluence of optical coatings for ultrashort laser pulses, different approaches have been developed. One relies on the use of

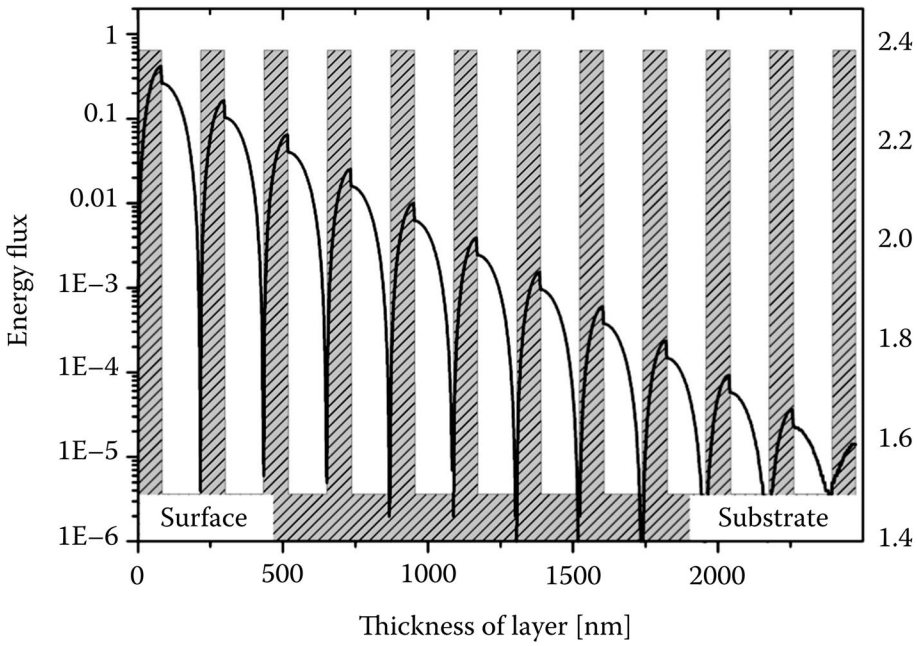

Fig. 22 Energy flux within a standard HR780 mirror coating consisting of a quarter-wave stack made of alternating TiO_2- and SiO_2-layers [141]. Copyright (© 2014) From (Laser-Induced Damage in Optical Materials) by (Ristau, D.). Reproduced by permission of Taylor and Francis Group, LLC, a division of Informa plc

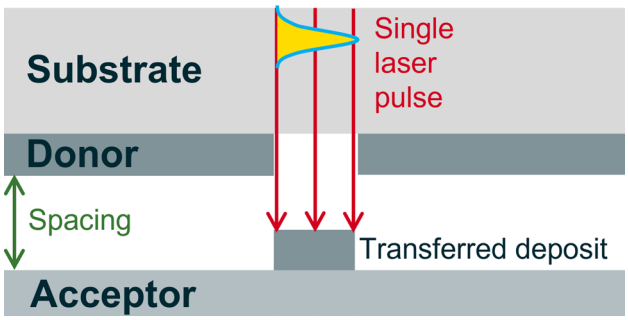

Fig. 23 Scheme of LIFT

ternary oxides instead of binary oxides, allowing for a band gap engineering resulting in more flexibility in the coating designs. Another approach is referred to as the *refractive index steps down* (RISED) concept [142]. Here, ternary oxides (e.g., $TiO_{1-x}Si_xO_2$) and SiO_2 may be used for deposition of stacks of alternating layers, where the refractive index of the $TiO_{1-x}Si_xO_2$ layers are continuously reduced with depth below the coating surface via the titanium oxide content ranging from 85% at the surface to 5%. This RISED approach allowed to increase the LIDT by more than a factor of two [142]. For more details on the engineering of damage resistant coatings for ultrashort laser pulses, the reader is referred to that reference.

4.4 Laser-induced forward transfer (LIFT)

LIFT is a method using the *superstrate geometry* according to (Fig. 1b). It was first demonstrated by Bohandy et al. in 1986 [143] and represents an additive direct-write technique: single excimer laser pulses at 193 nm wavelength were used to irradiate copper layers on fused silica substrates through the transparent dielectric. The distance between the copper donor layer and the silicon acceptor was below 10 µm. For suitable laser pulse energies, small copper deposits were transferred onto the silicon in vacuum. Two years later, Bohandy et al. demonstrated the process also in air environment for copper and silver layers transferred by 532-nm-pulses of a Nd:YAG laser and fused silica substrates as acceptor [144].

Figure 23 shows a scheme of the basic LIFT-setup. The incident laser pulse propagates through the transparent substrate (ideally without losses) and is absorbed at the backside of the donor layer that was previously deposited on the substrate material. When the laser fluence exceeds a material-specific threshold fluence, material is ejected from the donor film and moves to the acceptor substrate, resulting in a "laser-printed" deposit. The aim of the process is a localized deposition of the donor material on an acceptor substrate with spatial "resolution" in the micrometer range. For avoiding disintegration of the transferred deposits, the use of a top-hat spatial beam profile may be beneficial compared to a Gaussian beam, keeping the initial velocity of the ablating material widely constant.

LIFT is a powerful and flexible technique that is capable to transfer solid layers as well as "soft materials" (including liquid phases). LIFT of metals (e.g., aluminum [145], chromium [146–148], gold [149], nickel [150], platinum [151], titanium [146], tungsten [152], and vanadium [153]), semiconductors [154], dielectrics (Al_2O_3 [155], InO_x [156], V_2O_5 [157], ZnO [158]), and high-temperature superconductors [159] was reported. The method was also used for

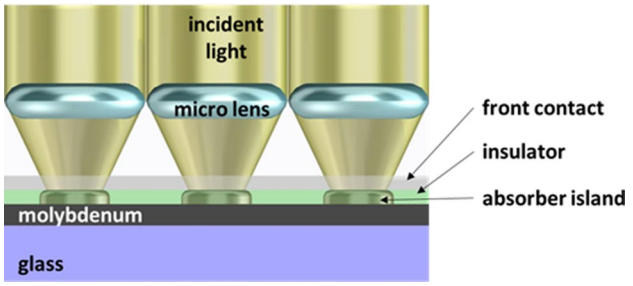

Fig. 24 Scheme of micro-concentrator solar cell concept [177]

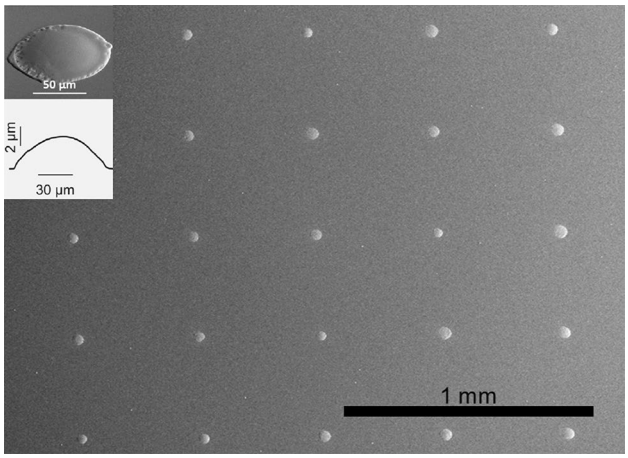

Fig. 25 Top-view optical micrograph of an array of indium islands on molybdenum-coated glass fabricated with site-selective shallow fs-laser ablation of the molybdenum layer surface (on glass substrate) and subsequent PVD of indium nucleating at the laser processed spots [177]. Insets: Tilted-view SEM of a typical indium droplet (top) and corresponding stylus profilometric scan through the center of the droplet (bottom) [179]. Insets reprinted from [179], Appl. Surf. Sci., Vol. **418**, Ringleb, F. et al., Growth and shape of indium islands on molybdenum at micro-roughened spots created by femtosecond laser pulses, 548–553, Copyright (2016), with permission from Elsevier

the printing of organic thin-film transistors [160], organic micro-capacitors [161], and organic light-emitting diodes [160, 162]. Even living biological cells [163, 164], DNA [165, 166], and proteins [167, 168] were successfully transferred via LIFT. It is worth mentioning that the first publication of the LIFT process using femtosecond laser pulses was by Bähnisch et al. in 2000 demonstrating the transfer of gold/tin disks [169]. The Au/Sn disks had good adhesion to the silicon substrate and a well-defined micrometric pad geometry. For review articles on LIFT, the reader is referred to the pertinent literature, e.g., [170–173] and very recently [174, 175].

The capabilities of LIFT will be demonstrated in the following by an example. In thin-film photovoltaics, micro-concentrator solar cells [176] are a promising approach to improve the efficiency of solar energy conversion. The photovoltaic active area is realized as an array of miniaturized, sub-millimeter-sized solar cells. The incident sunlight is focused on these cells via micro-lenses. The principle of this concept is shown in Fig. 24. The cells consist of solar absorber islands on a metallic back contact (here a thin Mo film that is mechanically stabilized by a glass substrate), embedded in an electrical insulator (green). The solar cells electric front contact layer (gray) covers both the insulator and the absorber islands.

Here, the case is to be considered, that the absorber islands are made of copper-indium-gallium-diselenide (CIGSe) on a molybdenum back contact on a glass substrate. Two different femtosecond laser-based methods to produce such micro-sized precursors of CIGSe solar absorber islands on molybdenum back contacts were investigated.

Method 1 (Laser-induced nucleation of indium): In a "classical" direct-focusing procedure, multiple pulses of a 30-fs laser at 790 nm center wavelength were used for subtle structuring (roughening) of the molybdenum film surface (320–420 nm thickness). A subsequent physical vapor deposition (PVD) of indium was utilized for the site-selective nucleation of indium droplets at the laser-ablated surface spots, serving as precursors for the production of CIGSe absorbers [178, 179]. Figure 25 visualizes a regular array of such indium droplets on a molybdenum back contact exclusively grown by the PVD at the laser-induced surface modifications. The inset of the figure shows a scanning electron micrograph (SEM) of a typical indium island along with a stylus profilometric scan across the center of the indium droplet.

Method 2 (LIFT of metallic precursors): Using the same fs-laser system, LIFT was performed with single laser pulses. Donor films consisting of both, indium and copper layers were utilized. Arrays of combined Cu-In-precursors of micro-absorbers were site-controlled deposited on the molybdenum back contact by moving the sample relative to the laser beam [180]. In a later work, even complete Cu-In-Ga layered stacks were successfully LIFTed as donor material [181].

The application potential of the LIFT deposition technique can be seen in Fig. 26a, where a 5×5 array of solar micro absorber islands is depicted. The micro absorbers were produced by subjecting the LIFTed Cu-In-Ga-precursor deposits to selenization through rapid thermal processing [182]. Figure 26b shows a top-view *energy dispersive X-ray* (EDX) analysis of one of these micro absorbers, visualizing the spatial distribution of the involved elements. It is obvious that all absorber components like indium, gallium, copper, and selenium are present in the micro absorber, while the molybdenum signal is reduced through the covering absorber island. Additionally, Fig. 26c presents a cross-sectional SEM and an EDX analysis of a micro absorber after deposition of the solar cell ZnO front contact layer. As

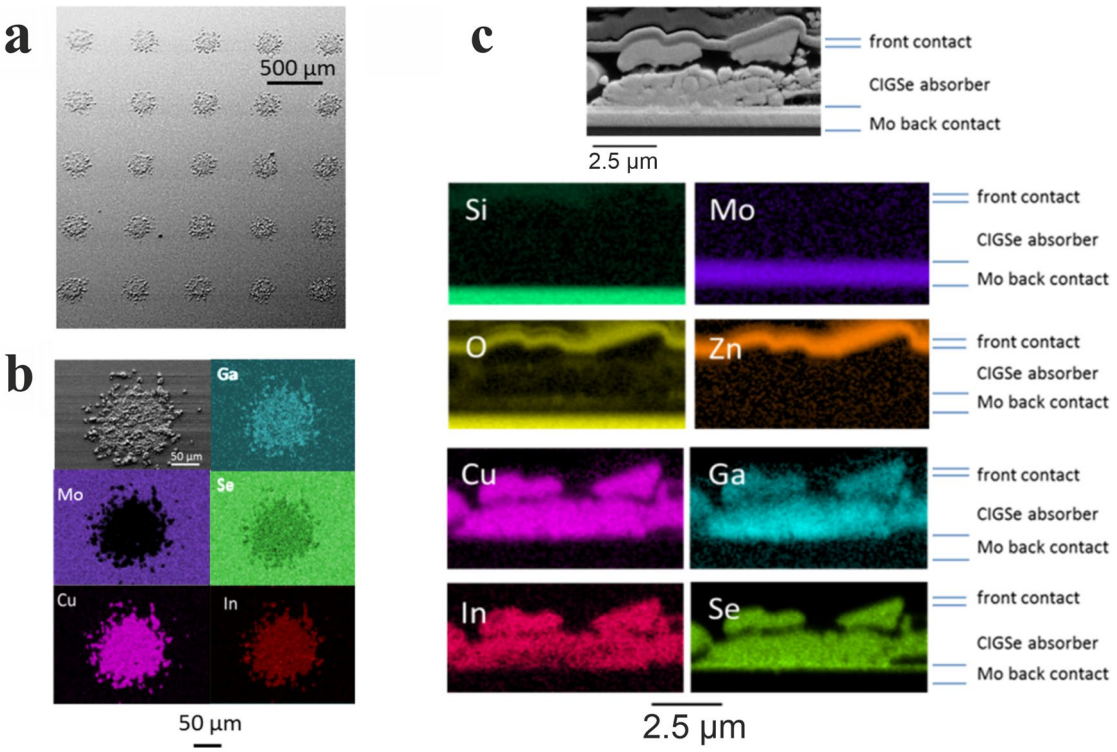

Fig. 26 Post-processed LIFT deposits of metallic Cu-In-Ga precursor layers on Mo-coated glass – after transformation into CIGSe micro absorber islands and solar cells. **a** Top-view SEM image of a 5×5 array of CIGSe micro absorber islands. **b** Top-view SEM image and EDX elemental distributions of a single micro absorber. **c** SEM and EDX cross-sections of a CIGSe micro absorber with additional ZnO front contact layer [182]. Reprinted (adapted) with permission from [182], Heidmann, B. et al., Fabrication of regularly arranged chalcopyrite micro solar cells via femtosecond laser-induced forward transfer for concentrator application, ACS Appl. Energy Mater. **1**:27–31 (2018). Copyright 2017 American Chemical Society

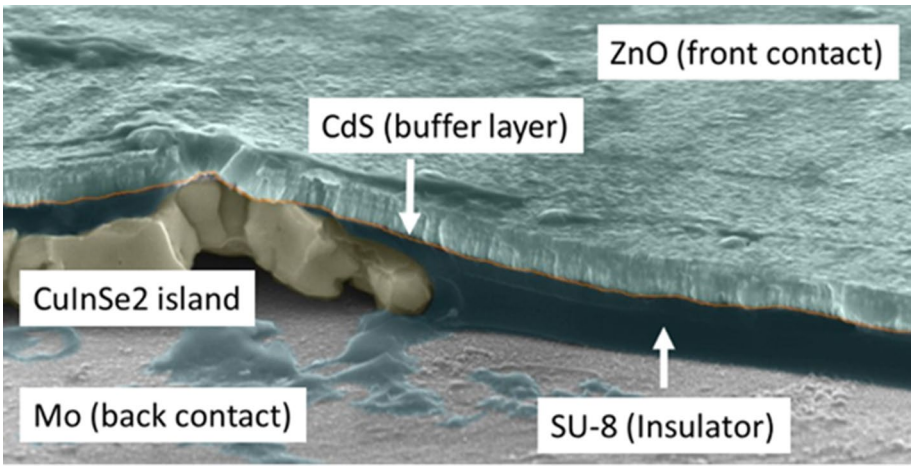

Fig. 27 Tilted-view SEM image of a breakage through a single $CuInSe_2$ micro solar cell produced by the indium-nucleation approach (Method 1). Reprinted (adapted) from [183], Ringleb, F. et al., Femtosecond laser-assisted fabrication of chalcopyrite micro-concentrator photovoltaics, Beilstein J. Nanotechn. **9**:3025–3038, Copyright 2018 under Creative Commons BY 4.0 license. https://doi.org/10.3762/bjnano.9.281

expected, zinc and oxygen are found at the top and molybdenum in the back contact, respectively. The copper signal is homogeneously distributed across the micro absorber, while indium is depleted in proximity to the back contact and gallium toward the front contact. The control of stoichiometry of the chalcopyrite materials is challenging. Here, the advantage of the LIFT technique may lie in the flexibility to tailor the precursor composition by adequate choice of the donor layer(s) and the sequence of transfer. Additionally, the number of processing steps for manufacturing micro solar cells can be reduced. Moreover, LIFT is a single-pulse process while the alternative strategy of In-island growth bases on a multi-pulse laser treatment of the molybdenum back

contact layer. Thus, the laser processing time is in favor of the LIFT-process here.

For both fs-laser processes discussed above (Methods 1 & 2), an efficient and material saving bottom–up fabrication step of precursors for fully functional and working micro-concentrator solar cells was successfully demonstrated [183]. Figure 27 depicts a cross-section of a breakage through a single $CuInSe_2$ (CISe) micro solar cell produced by the In-nucleation approach of Method 1. The main components are labeled and marked by arrows. The polycrystalline grain structure of the CISe Island sandwiched between the ZnO front and Mo back contact is evident.

The CISe micro absorber cells (Fig. 27) were electrically connected in a parallel manner and conversion efficiencies between 0.15% and 2.9% under 1 sun illumination strength were demonstrated. Under concentrated illumination conditions exceeding this value, significant efficiency enhancements could be achieved [183].

4.5 Thin-film depth-profiling for material analyses

The idea to characterize materials by removing and analyzing a microscopic part of a sample through focused laser radiation is almost as old as the laser itself [184]. Since that time several concepts and variants of laser ablation based chemical analysis methods, such as *laser-induced breakdown spectroscopy* (LIBS) or *laser ablation mass spectrometry* (LA-MS), have been developed for solids and liquids were steadily improved during the last decades [185–189]. These approaches are based on the examination of material removed by the laser beam (usually the ablation plasma containing electrons, atoms, ions, clusters, or nano- and microparticles), which is subsequently analyzed in detail either by optical or by mass spectrometric techniques. All of them take benefit from advantages provided by laser ablation process, i.e., allowing to probe microscopically small sample volumes in a contactless and rapid manner. Around the turn of the millennium, these techniques have been successfully combined with femtosecond laser sources since their application seemed to be promising and beneficial with respect to the possible sensitivity, background signal levels, and depth-resolution (for the reasons briefly discussed in Sect. 2).

The specific advantages of fs-laser ablation for application in chemical analysis of solids can be summarized as follows [186, 190, 191]: (1) No sample preparation is needed. (2) Conductive and non-conductive arbitrary shapes can be analyzed directly. (3) Spatial (lateral) resolutions down to a few micrometers or even below can be obtained, controlled via the diameter of the focused laser beam. (4) A rapid analysis of multiple elements is possible. (5) Stoichiometric and very precise lateral and vertical material sampling can be achieved by employing ultrashort laser pulse durations.

However, if the fs-laser ablation is performed in reactive environments, such as air, care must be taken since interpulse chemical reactions (e.g., oxidation) may alter the surface chemistry [17, 18]. Top-hat spatial beam profiles are superior to Gaussian shaped ones for avoiding spectroscopic signal intermixing from different sample ablation depths. Moreover, the laser irradiation conditions must be carefully adjusted to realize small ablation rates of the order of 10 nm/pulse while simultaneously reducing "topographic cross-talk", e.g., potentially arising from self-ordered micro- and nanostructures, such as laser-induced periodic surface structures, micro-grooves or -spikes [19, 67, 70, 192] or surface roughness.

4.5.1 fs-LIBS

In fs-LIBS [193, 194], an ablation plasma is induced by fs-laser irradiation of a solid sample material either in air or an inert buffer-gas environment at atmospheric or reduced pressures. The time-gated and in most cases spatially integrated optical emission of this ablation plasma is used for the analytical proof of elements in the plasma which is related to the local sample composition.

First studies on fs-LIBS were published 2000 and 2001 by different groups in Germany [195–197], the United States of America [198], and Canada [199]. Margetic et al. [195] performed a comparative study of fs- and ns-LIBS of brass samples in Argon inert gas (775 nm, 170 fs/6 ns, max. 10 Hz, 1–1000 mbar). They found significant influences of the buffer-gas pressure and differences in the temporal evolution of the atomic and ionic line intensities for fs- and ns-pulses. The more reproducible fs-laser ablation leads to a reduced ablation threshold fluence, an improved ablation precision and higher sensitivity. In a later study on the same material (brass, 775 nm, 170 fs, max. 10 Hz, 40 mbar Ar) [196], more attention was paid to the nonlinearity of calibration curves as they can be found in ablation measurements in alloys.

Additional work has been performed in this group with respect to the depth-resolved analysis of multi-layer samples. In a comparative study between fs-LIBS (Ar buffer-gas, 1–1000 mbar) and fs-LA-ToF–MS (vacuum $< 10^{-6}$ mbar) samples consisting of 600 nm thick Cu-Ag sandwich layers on silicon could be resolved by the fs-LIBS technique (775 nm, 170 fs, max. 10 Hz) [197]. The spatially Gaussian shaped beam profile limited the contrast of the detected depth profiles. Angel et al. [198] reported about fs-, ps- and ns-LIBS measurements on copper in air at atmospheric pressure (810 nm, 140 fs, 1–1000 Hz). Compared to ns-pulse excitation (1064 nm, 7 ns, 5 Hz), the ultrashort laser pulse generated ablation plasmas showed a much lower background signal and a more rapid decay of atomic line emissions. The authors state that due to the relatively low

background, a temporally non-gated optical signal detection is very effective. High femtosecond laser pulse repetition rates (1000 Hz) were shown to increase the LIBS signal. Le Drogoff et al. [199] performed comparative studies on time-resolved space-integrated fs- (800 nm, 100 fs, 10 Hz) and ns-LIBS (1064 nm, 8 ns) of aluminum alloys in air at atmospheric pressure as well. Besides the observation of the faster decay of continuum and spectral lines and a shorter plasma lifetime in the fs-case, the analytical performance was evaluated. The fs-LIBS detection limits were found to be element dependent. They vary between 2 and 80 parts per million (ppm).

New dual-pulse LIBS geometries combining the material excitation with combinations of fs- and ns-laser pulses (for pre-ablation spark generation or plasma re-heating) are reported by Scaffidi et al. [200]. Large signal enhancements up to 80 were observed for copper and aluminum bulk samples for ablation with 100-fs (800 nm) laser pulses and plasma re-heating with subsequent ns-laser pulses (1064 nm, 7 ns).

Further aspects of fs-LIBS were reviewed in detail by Labutin et al. [194], including reports on depth-resolutions of the order of a few tens of nanometers when employing top-hat spatial beam profiles.

4.5.2 fs-LA-MS

Wechsung et al. [201] presented in 1978 the method of *laser microprobe mass analysis* (LAMMA) that is combining the laser ablation process with mass spectroscopy (LA-MS). Nowadays, *femtosecond laser alation mass spectrometry* (fs-LA-MS) has been developed into three main variants, i.e., the *femtosecond laser ablation inductively coupled plasma mass spectrometry* (fs-LA-ICP-MS), the *femtosecond laser ablation time-of-flight mass spectrometry* (fs-LA-ToF–MS), and as *femtosecond matrix-assisted laser desorption/ionization time-of-flight mass spectrometry* (fs-MALDI-ToF–MS). Since the latter is—by its principle—not made for analyzing thin films, the focus in this review article will lie solely on the first two methods, as briefly discussed in the following.

In fs-LA-ToF–MS [186, 188] the ionic species of the laser-induced plasma are analyzed with respect to their arrival time to a mass sensitive detector. Figure 28 provides a scheme of a fs-LA-ToF–MS presented in Cui et al. [202]. This technique is advantageous compared to the LIBS method with respect to the sensitivity and the simultaneous detection capability of ions of all elements removed from the surface by a single laser shot [188]. In a first study of Margetic et al. [197], a depth-resolved fs-LA-ToF–MS analysis (pressure < 10^{-6} mbar, laser excitation: 775 nm, 170–200 fs, max. 10 Hz) was performed on a TiN-TiAlN layered system deposited on an iron substrate. The layered structure with a thickness of 280 nm of each layer could be clearly resolved.

In a later study of this group, the fs-LA-ToF–MS was successfully applied to the depth-resolved analysis of multi-layer samples (pressure < 10^{-6} mbar, laser excitation: 775 nm, 170–200 fs, max. 10 Hz) [190]. An ion-implanted silicon wafer (150 nm shallow Co-implanted layer, 10^{17} ions/cm^3) and a thin film metal standard (NIST 2135c consisting of alternating Cr and Ni layers, having a thickness of 56 and 57 nm, respectively) have been analyzed. Lateral resolutions of 30 µm – 40 µm and a depth resolution of ~ 10 nm (limited by the pulse-to-pulse energy stability of ±5%) combined with a mass-resolution of $m/\Delta m \sim 300$ were demonstrated in that work. Meanwhile, better lateral resolution, significantly increased mass resolutions exceeding 10,000, and detection limits of a few tens of parts per billion (ppb) or single-pulse detection limits of 10^{-15} g (fg) were demonstrated in selected applications (see Tulej et al. [188] and references therein).

Later, systematic depth-profiling analyses were performed on semiconductor wafers and metal foils [202,

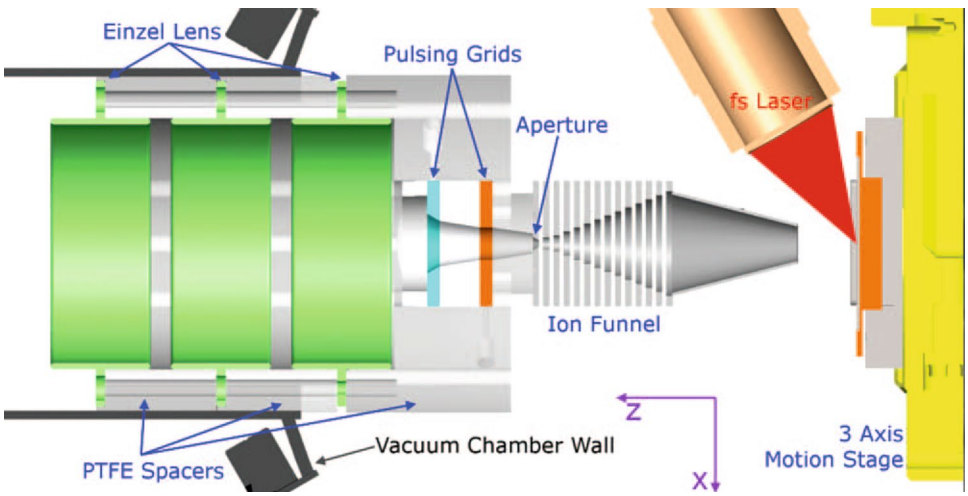

Fig. 28 Illustration of a fs-LA-ToF–MS system [202] consisting of the ion optics, sample stage, laser focusing system, and a vacuum chamber including the differential vacuum wall. Reprinted from Cui, Y. et al., Depth profiling and imaging capabilities of an ultrashort pulse laser ablation time of flight mass spectrometer, Rev. Sci. Instrum. **83**:093702 (2012), with the permission of AIP Publishing

Table 1 Classification of dominant laser-induced film damage mechanisms, ordered according to the material classes (metals, semiconductors, dielectrics) and for small (left column group), medium (middle column group) and large film (right column group) thicknesses

Film material	Small film thickness ($d < \lambda/2$)		Medium film thickness ($\lambda/2 \leq d \leq z_R$)		Large film thickness ($d > z_R$)	
	LR substrate	HR substrate	LR substrate	HR substrate	LR substrate	HR substrate
Metal	SubStr: SD, ID	SubStr: SD, ID	SubStr: SD	SubStr: SD	SubStr: SD	SubStr: SD
	SuperStr: ID, NA	SuperStr: NA	SuperStr: ID, NA	SuperStr: NA	SuperStr: ID, NA	SuperStr: NA
Semiconductor	SubStr: SD, ID	SubStr: SD, ID	SubStr: SD, ID, BD	SubStr: SD, ID, BD	SubStr: SD, ID	SubStr: SD, ID
	SuperStr: ID, NA	SuperStr: NA	SuperStr: ID, NA	SuperStr: NA	SuperStr: ID, NA	SuperStr: NA
Dielectrics	SubStr: SD, ID	SubStr: SD, ID	SubStr: SD, ID, BD	SubStr: SD, ID, BD	SubStr: SD, BD	SubStr: SD, BD
	SuperStr: ID, NA	SuperStr: NA	SuperStr: ID, NA	SuperStr: NA	SuperStr: ID, NA	SuperStr: NA

Each column group is divided into situations with low reflective (LR) substrate materials and high reflective (HR) substrate materials

SubStr: Substrate geometry, SuperStr: Superstrate geometry

SD: Surface damage (heterogeneous melting / ablation);

ID: Interface damage (stress-induced or ablative spallation);

BD: Bulk damage (homogeneous melting / ablation; Interference-induced);

NA: Not accessible (intensity-related defocusing (Kerr effect); opaque substrate)

203]. Although no attempt was made to calibrate the results against the number of applied laser pulses per spot, an estimate of the depth-resolution ranges from a few nanometers to a few tens of nanometers in the laser fluence window between 0.6 and 1 J/cm^2 [188].

In fs-LA-ICP-MS [204, 205] the femtosecond laser generated plasma is injected into a stream of inert gas (e.g., Ar) which transports the ablated species to an inductively coupled mass spectrometer (ICP-MS). When using a fs-laser source, nanoparticles with a size distribution centered around 100 to 200 nm are generated that can be easily decomposed in the ICP-torch. However, since the technique involves this crucial aerosol transport, it requires a very careful adjustment of operation parameters and data evaluation. Some limitations during the aerosol transport, and the partial digestion in the plasma of the Ar torch [206], make this technique at first view more promising for the investigation of bulk samples than for thin film analysis. Nevertheless, high depth-resolutions of several tens of nanometers were demonstrated for metal films studied by fs-LA-ICP–MS with optimized ablation conditions (laser excitation: 400 nm, 150 fs, 1 Hz, homogenized beam) [207], making this method also suitable for depth-profiling applications of thin films [188, 191]. Moreover, a remarkable sensitivity is reached that even allows to identify isotopes and monitor their ratios and, thus, can be used in archaeological and geological investigations [205, 208].

In conclusion, both technologies, fs-LIBS and fs-LA-MS, have reached a mature state and can be routinely used for thin-film depth-profiling for material analyses in specialized laboratories.

5 Summary and outlook

An approach to classify film damage mechanisms by ultrashort laser pulses at the lowest fluence leading to a permanent material alteration regarding possible damage mechanisms is presented in Table 1, ordering for the different film material classes (metals, semiconductors, dielectrics) the possible damage mechanisms regarding to the film thickness (small, medium, large), the carrier substrate materials (low or high reflective at the laser wavelength), and the laser processing geometry (substrate vs. superstrate). The table may aid and guide the reader to identify potentially relevant laser damage scenarios (SD: surface damage, ID: interface damage, BD: bulk damage) for their specific experimental conditions.

In conclusion, ultrashort laser pulses have proven to be a valuable tool for structuring thin and thick films when contactless and precise material removal or surface modification is desired. With very few exceptions, their use is superior to that of laser pulses with longer pulse duration (of the same wavelength and spatial beam profile) by "transcribing" the reduced heat-affected zone or nonlinear absorption mechanisms into an improved sub-micrometer machining precision. Just in very few cases, where detrimental high-intensity-related limiting effects manifest, e.g., through

localized electromagnetic field-enhancement in the bulk of the films or at its surface topography, potential care must be taken. Given these unique advantages and the already broad availability of reliable high-repetition rate sources, ultrashort laser pulses will further conquer industrial thin film processing for tailored scientific and real-life applications.

Funding Open Access funding enabled and organized by Projekt DEAL.

Declarations

Conflict of interest The authors declare that there are no conflicts of interest related to this article.

References

1. D. Bäuerle, *Laser Processing and Chemistry*, 4th edn. (Springer, Berlin, 2011) https://doi.org/10.1007/978-3-642-17613-5
2. M. Lenzner, J. Krüger, W. Kautek, F. Krausz, Precision laser ablation of dielectrics in the 10-fs regime. Appl. Phys. A **68**, 369–371 (1999). https://doi.org/10.1007/s003390050906
3. J. Bonse, M. Geuss, S. Baudach, H. Sturm, W. Kautek, The precision of the femtosecond-pulse laser ablation of TiN films on silicon. Appl. Phys. A **69**, S399–S402 (1999). https://doi.org/10.1007/s003390051425
4. D. Ristau (Ed.), *Laser-induced Damage in Optical Materials*, 1st edn. (CRC Press/Taylor & Francis Group, Boca Raton, 2015) https://doi.org/10.1201/b17722
5. N. Bloembergen, Laser-induced electric breakdown in solids. IEEE J. Quantum Electron. **10**, 375–386 (1974). https://doi.org/10.1109/JQE.1974.1068132
6. B.C. Stuart, M.D. Feit, S. Herman, A.M. Rubenchik, B.W. Shore, M.D. Perry, Optical ablation by high-power short-pulse lasers. J. Opt. Soc. Am. B **13**, 459–468 (1996). https://doi.org/10.1364/JOSAB.13.000459
7. J. Krüger, W. Kautek, The femtosecond pulse laser: A new tool for micromachining. Las. Phys. **9**, 30–40 (1999). https://www.yumpu.com/en/document/read/4252495/the-femtosecond-pulse-laser-a-new-tool-for-micromachining
8. D. von der Linde, K. Sokolowski-Tinten, The physical mechanisms of short-pulse laser ablation. Appl. Surf. Sci. **154–155**, 1–10 (2000). https://doi.org/10.1016/S0169-4332(99)00440-7
9. F. Dausinger, F. Lichtner, H. Lubatschowski (Eds.), *Femtosecond Technology for Technical and Medical Applications*, (Springer, Berlin, 2004) https://doi.org/10.1007/b96440
10. E.G. Gamaly, *Femtosecond Laser-Matter Interaction—Theory, Experiments and Applications* (Taylor & Francis Group, Boca Raton, 2011)
11. R. Osellame, G. Cerullo, R. Ramponi (Eds.), *Femtosecond Laser Micromachining — Photonic and Microfluidic Devices in Transparent Materials*, (Springer, Berlin, 2012) https://doi.org/10.1007/978-3-642-23366-1
12. K. Sugioka, Y. Cheng, Ultrafast lasers—reliable tools for advanced materials processing. Light Sci. Appl. **3**, e149 (2014). https://doi.org/10.1038/lsa.2014.30
13. K. Sugioka, Y. Cheng (eds.), *Ultrafast laser processing: from micro- to nanoscale industrial applications* (Taylor & Francis Group, Boca Raton, 2013)
14. G. Račiukaitis, Ultra-short pulse lasers for microfabrication: a review. IEEE J. Sel. Top. Quantum Electron. **27**, 1100112 (2021). https://doi.org/10.1109/JSTQE.2021.3097009
15. D. Förster, B. Jäggi, A. Michalowski, B. Neuenschwander, Review on experimental and theoretical investigations of ultrashort pulsed laser ablation of metals with burst pulses. Materials **14**, 3331 (2021). https://doi.org/10.3390/ma14123331
16. R. Stoian, J. Bonse (Eds.), *Ultrafast Laser Nanostructuring — The Pursuit of Extreme Scales*, (Springer Nature, Cham, 2023), ISBN 978-3-031-14751-7 (**in press**)
17. J. Bonse, J. Krüger, Probing the heat affected zone by chemical modifications in femtosecond pulse laser ablation of titanium nitride films in air. J. Appl. Phys. **107**, 054902 (2000). https://doi.org/10.1063/1.3311552
18. J. Bonse, H. Sturm, D. Schmidt, W. Kautek, Chemical, morphological and accumulation phenomena in ultrashort-pulse laser ablation of TiN in air. Appl. Phys. A **71**, 657–665 (2000). https://doi.org/10.1007/s003390000585
19. J. Bonse, S. Baudach, J. Krüger, W. Kautek, M. Lenzner, Femtosecond laser ablation of silicon—modification thresholds and morphology. Appl. Phys. A **74**, 19–25 (2002). https://doi.org/10.1007/s003390100893
20. C. Florian, D. Fischer, K. Freiberg, M. Duwe, M. Sahre, S. Schneider, A. Hertwig, J. Krüger, M. Rettenmayr, U. Beck, A. Undisz, J. Bonse, Single femtosecond laser-pulse-induced superficial amorphization and re-crystallization of silicon. Materials **14**, 1651 (2021). https://doi.org/10.3390/ma14071651
21. T. Beuermann, H.J. Brinkmann, T. Damm, M. Stuke, Picosecond UV Excimer laser ablation of $LiNbO_3$. MRS Proc. **191**, 37–42 (1990). https://doi.org/10.1557/PROC-191-37
22. B. Wolff-Rottke, J. Ihlemann, H. Schmidt, A. Scholl, Influence of the laser-spot diameter on photo-ablation rates. Appl. Phys. A **60**, 13–17 (1995). https://doi.org/10.1007/BF01577606
23. T.E. Glover, G.D. Ackerman, R.W. Lee, H.A. Padmore, D.A. Young, Metal–insulator transitions in an expanding metallic fluid: particle formation during femtosecond laser ablation. Chem. Phys. **299**, 171–181 (2004). https://doi.org/10.1016/j.chemphys.2003.11.042
24. S. Amoruso, R. Bruzzese, N. Spinelli, R. Velotta, M. Vitiello, X. Wang, G. Ausanio, V. Iannotti, L. Lanotte, Generation of silicon nanoparticles via femtosecond laser ablation in vacuum. Appl. Phys. Lett. **84**, 4502–4504 (2004). https://doi.org/10.1063/1.1757014
25. S. Nolte, C. Momma, H. Jacobs, A. Tünnermann, B.N. Chichkov, B. Wellegehausen, H. Welling, Ablation of metals by ultrashort laser pulses. J. Opt. Soc. Am. B **14**, 2716–2722 (1997). https://doi.org/10.1364/JOSAB.14.002716
26. D. Ashkenasi, A. Rosenfeld, H. Varel, M. Wähmer, E.E.B. Campbell, Laser processing of sapphire with picosecond and sub-picosecond pulses. Appl. Surf. Sci. **120**, 65–80 (1997). https://doi.org/10.1016/S0169-4332(97)00218-3

27. R. Stoian, D. Ashkenasi, A. Rosenfeld, E.E.B. Campbell, Phys. Rev. B **62**, 13167–13173 (2000). https://doi.org/10.1103/PhysRevB.62.13167
28. R. Stoian, A. Rosenfeld, D. Ashkenasi, I.V. Hertel, N.M. Bulgakova, E.E.B. Campbell, Surface charging and impulsive ion ejection during ultrashort pulsed laser ablation. Phys. Rev. Lett. **88**, 097603 (2002). https://doi.org/10.1103/PhysRevLett.88.097603
29. M.M. Martynyuk, Vaporization and boiling of liquid metal in an exploding wire. Sov. Phys. Tech. Phys. **19**, 793–797 (1974)
30. R. Kelly, A. Miotello, Comments on explosive mechanisms of laser sputtering. Appl. Surf. Sci. **96–98**, 205–215 (1996). https://doi.org/10.1016/0169-4332(95)00481-5
31. N.M. Bulgakova, A.V. Bulgakov, Pulsed laser ablation of solids: transition from normal vaporization to phase explosion. Appl. Phys. A **73**, 199–208 (2001). https://doi.org/10.1007/s003390000686
32. M.V. Shugaev, M. He, Y. Levy, A. Mazzi, A. Miotello, N.M. Bulgakova, L.V. Zhigilei, Laser-Induced Thermal Processes: Heat Transfer, Generation of Stresses, Melting and Solidification, Vaporization, and Phase Explosion. in *Handbook of Laser Micro- and Nano-Engineering,* ed. by K. Sugioka (Springer, Cham, 2021). pp. 83–163 https://doi.org/10.1007/978-3-030-63647-0_11
33. J. Ihlemann, A. Scholl, H. Schmidt, B. Wolff-Rottke, Nanosecond and femtosecond excimer-laser ablation of oxide ceramics. Appl. Phys. A **60**, 411–417 (1995). https://doi.org/10.1007/BF01538343
34. A. Ancona, F. Röser, K. Rademaker, J. Limpert, S. Nolte, A. Tünnermann, High speed laser drilling of metals using a high repetition rate, high average power ultrafast fiber CPA system. Opt. Express **16**, 8958–8968 (2008). https://doi.org/10.1364/OE.16.008958
35. E. Matthias, M. Reichling, J. Siegel, O.W. Käding, S. Petzoldt, H. Skurk, P. Bizenberger, E. Neske, The influence of thermal diffusion on laser ablation of metal films. Appl. Phys. A **58**, 129–136 (1994). https://doi.org/10.1007/BF00332169
36. S.I. Anisimov, B. Kapeliovich, T. Perel'man, Electron emission from metal surfaces exposed to ultrashort laser pulses. Sov. Phys. JETP **39**, 375–377 (1974).
37. P.B. Corkum, F. Brunel, N.K. Sherman, T. Srinivasan-Rao, Thermal response of metals to ultrashort-pulse laser excitation. Phys. Rev. Lett. **61**, 2886–2889 (1988). https://doi.org/10.1103/PhysRevLett.61.2886
38. S.-S. Wellershoff, J. Hohlfeld, J. Güdde, E. Matthias, The role of electron–phonon coupling in femtosecond laser damage of metals. Appl. Phys. A **69**, S99–S107 (1999). https://doi.org/10.1007/s003399900305
39. J. Jandeleit, G. Urbasch, H.D. Hoffmann, H.-G. Treusch, E.W. Kreutz, Picosecond laser ablation of thin copper films. Appl. Phys. A **63**, 117–121 (1996). https://doi.org/10.1007/BF01567638
40. B.N. Chichkov, C. Momma, S. Nolte, F. von Alvensleben, A. Tünnermann, Femtosecond, picosecond and nanosecond laser ablation of solids. Appl. Phys. A **63**, 109–115 (1996). https://doi.org/10.1007/BF01567637
41. E. Carpene, Ultrafast laser irradiation of metals: beyond the two-temperature model. Phys. Rev. B **74**, 024301 (2006). https://doi.org/10.1103/PhysRevB.74.02430
42. Z. Lin, L.V. Zhigilei, V. Celli, Electron-phonon coupling and electron heat capacity of metals under conditions of strong electron-phonon nonequilibrium. Phys. Rev. B **77**, 075133 (2008). https://doi.org/10.1103/PhysRevB.77.075133
43. M. Uehlein, S.T. Weber, B. Rethfeld, Influence of electronic nonequilibrium on energy distribution and dissipation in aluminum studied with an extended two-temperature model. Nanomaterials **12**, 1655 (2022). https://doi.org/10.3390/nano12101655
44. G.D. Tsibidis, E. Stratakis, Damage threshold evaluation of thin metallic films exposed to femtosecond laser pulses: the role of material thickness. Opt. Laser Technol. **156**, 108484 (2022). https://doi.org/10.1016/j.optlastec.2022.108484
45. R. Hayashi, A. Iwasaki, P. Vasa, K. Yamanouchi, Determination of electron and phonon temperatures in gold thin film irradiated with an ultrashort laser pulse. AIP Adv. **12**, 095207 (2022). https://doi.org/10.1063/5.0090466
46. T.J.-Y. Derrien, Y. Levy, N.M. Bulgakova, Insights into laser-matter interaction from inside: wealth of processes, multiplicity of mechanisms and possible roadmaps for energy localization, in *Ultrafast Laser Nanostructuring — The Pursuit of Extreme Scales*, ed. by R. Stoian, J. Bonse (Springer Nature, Cham, 2023), ISBN 978-3-031-14751-7 (**in press**)
47. J. Krüger, D. Dufft, R. Koter, A. Hertwig, Femtosecond laser-induced damage of gold films. Appl. Surf. Sci. **253**, 7815–7819 (2007). https://doi.org/10.1016/j.apsusc.2007.02.164
48. Y. Jee, M.F. Becker, R.M. Walser, Laser-induced damage on single-crystal metal surfaces. J. Opt. Soc. Am. B **5**, 648–659 (1988). https://doi.org/10.1364/JOSAB.5.000648
49. J. Güdde, J. Hohlfeld, J.G. Müller, E. Matthias, Damage threshold dependence on electron–phonon coupling in Au and Ni films. Appl. Surf. Sci. **127–129**, 40–45 (1998). https://doi.org/10.1016/S0169-4332(98)00002-6
50. M.Z. Mo, V. Becker, B.K. Ofori-Okai, X. Shen, Z. Chen, B. Witte, R. Redmer, R.K. Li, M. Dunning, S.P. Weathersby, X.J. Wang, S.H. Glenzer, Determination of the electron-lattice coupling strength of copper with ultrafast MeV electron diffraction. Rev. Sci. Instrum. **89**, 10C108 (2018). https://doi.org/10.1063/1.5035368
51. F. Ruffino, M.G. Grimaldi, Nanostructuration of thin metal films by pulsed laser irradiations: a review. Nanomaterials **9**, 1133 (2019). https://doi.org/10.3390/nano9081133
52. Y. Nakata, T. Okada, M. Maeda, Nano-sized hollow bump array generated by single femtosecond laser pulse. Jpn. J. Appl. Phys. **42**, L1452–L1454 (2003). https://doi.org/10.1143/JJAP.42.L1452
53. F. Korte, J. Koch, B.N. Chichkov, Formation of microbumps and nanojets on gold targets by femtosecond laser pulses. Appl. Phys. A **79**, 879–881 (2004). https://doi.org/10.1007/s00339-004-2590-5
54. Y.P. Meshcheryakov, N.M. Bulgakova, Thermoelastic modeling of microbump and nanojet formation on nanosize gold films under femtosecond laser irradiation. Appl. Phys. A **82**, 363–368 (2006). https://doi.org/10.1007/s00339-005-3319-9
55. D.S. Ivanov, B. Rethfeld, G.M. O'Connor, T.J. Glynn, A.N. Volkov, L.V. Zhigilei, The mechanism of nanobump formation in femtosecond pulse laser nanostructuring of thin metal films. Appl. Phys. A **92**, 791–796 (2008). https://doi.org/10.1007/s00339-008-4712-y
56. D.S. Ivanov, A.I. Kuznetsov, V.P. Lipp, B. Rethfeld, B.N. Chichkov, M.E. Garcia, W. Schulz, Short laser pulse nanostructuring of metals: direct comparison of molecular dynamics modeling and experiment. Appl. Phys. A **111**, 675–687 (2013). https://doi.org/10.1007/s00339-013-7656-9
57. A.I. Kuznetsov, J. Koch, B.N. Chichkov, Nanostructuring of thin gold films by femtosecond lasers. Appl. Phys. A **94**, 221–230 (2009). https://doi.org/10.1007/s00339-008-4859-6
58. C. Unger, J. Koch, L. Overmeyer, B.N. Chichkov, Time-resolved studies of femtosecond-laser induced melt dynamics. Opt. Express **22**, 24864–24872 (2012). https://doi.org/10.1364/OE.20.024864
59. L.V. Keldysh, Ionization in the field of a strong electromagnetic wave. Sov. Phys. JETP **20**, 1307–1314 (1965).
60. M. Lenzner, J. Krüger, S. Sartania, Z. Cheng, Ch. Spielmann, G. Mourou, W. Kautek, F. Krausz, Femtosecond optical breakdown

in dielectrics. Phys. Rev. Lett. **80**, 4076–4079 (1998). https://doi.org/10.1103/PhysRevLett.80.4076
61. J. Bonse, S.M. Wiggins, J. Solis, T. Lippert, Phase change dynamics in a polymer thin film upon femtosecond and picosecond laser irradiation. Appl. Surf. Sci. **247**, 440–446 (2005). https://doi.org/10.1016/j.apsusc.2005.01.125
62. M. Mero, J. Liu, W. Rudolph, D. Ristau, K. Starke, Scaling laws of femtosecond laser pulse induced breakdown in oxide films. Phys. Rev. B **71**, 115109 (2005). https://doi.org/10.1103/PhysRevB.71.115109
63. M. Mero, B. Clapp, J.C. Jasapara, W. Rudolph, D. Ristau, K. Starke, J. Krüger, S. Martin, W. Kautek, On the damage behavior of dielectric films when illuminated with multiple femtosecond laser pulses. Opt. Eng. **44**, 051107 (2005). https://doi.org/10.1117/1.1905343
64. Z. Sun, M. Lenzner, W. Rudolph, Generic incubation law for laser damage and ablation thresholds. J. Appl. Phys. **117**, 073102 (2015). https://doi.org/10.1063/1.4913282
65. See http://www.lenzner.us/incubation [accessed on Sept. 4th 2022]
66. C. Kunz, S. Engel, F.A. Müller, S. Gräf, Large-area fabrication of laser-induced periodic surface structures on fused silica using thin gold layers. Nanomaterials **10**, 1187 (2020). https://doi.org/10.3390/nano10061187
67. J. Bonse, S. Höhm, S.V. Kirner, A. Rosenfeld, J. Krüger, Laser-induced periodic surface structures—a scientific evergreen. IEEE J. Sel. Top. Quantum Electron. **23**, 9000615 (2017). https://doi.org/10.1109/JSTQE.2016.2614183
68. C. Florian, S.V. Kirner, J. Krüger, J. Bonse, Surface functionalization by laser-induced periodic surface structures. J. Laser Appl. **32**, 022063 (2020). https://doi.org/10.2351/7.0000103
69. S. Gräf, Formation of laser-induced periodic surface structures on different materials: fundamentals, properties and applications. Adv. Opt. Technol. **9**, 11–39 (2020). https://doi.org/10.1515/aot-2019-0062
70. J. Bonse, S. Gräf, Maxwell meets Marangoni—a review of theories on laser-induced periodic surface structures. Laser Photonics Rev. **14**, 2000215 (2020). https://doi.org/10.1002/lpor.202000215
71. J.P. McDonald, J.A. Nees, S.M. Yalisove, Pump-probe imaging of femtosecond pulsed laser ablation of silicon with thermally grown oxide films. J. Appl. Phys. **102**, 063109 (2007). https://doi.org/10.1063/1.2778740
72. S. Rapp, M. Domke, M. Schmidt, H.P. Huber, Physical mechanisms during fs laser ablation of thin SiO_2 films. Phys. Procedia **41**, 734–740 (2013). https://doi.org/10.1016/j.phpro.2013.03.141
73. M.C. Downer, R.L. Fork, C.V. Shank, Femtosecond imaging of melting and evaporation at a photoexcited silicon surface. J. Opt. Soc. Am. B **2**, 595–599 (1985). https://doi.org/10.1364/JOSAB.2.000595
74. D. von der Linde, K. Sokolowski-Tinten, J. Bialkowski, Laser-solid interaction in the femtosecond time regime. Appl. Surf. Sci. **109–110**, 1–10 (1997). https://doi.org/10.1016/S0169-4332(96)00611-3
75. A. Horn, *Ultra-fast Material Metrology*, (Wiley-VCH Verlag, Weinheim, 2009) https://doi.org/10.1002/9783527627929
76. J. Bonse, Scattering on scattering. Light: Sci. Appl. **6**, e17088 (2017). https://doi.org/10.1038/lsa.2017.88
77. M. Garcia-Lechuga, J. Solis, J. Siegel, Probing matter by light, In: R. Stoian, J. Bonse (Eds.): *Ultrafast Laser Nanostructuring — The Pursuit of Extreme Scales*, (Springer Nature, Cham, 2023), ISBN 978-3-031-14751-7, (**in press**)
78. J. Bonse, K.W. Brzezinka, A.J. Meixner, Modifying single-crystalline silicon by femtosecond laser pulses: an analysis by micro Raman spectroscopy, scanning laser microscopy and atomic force microscopy. Appl. Surf. Sci. **221**, 215–230 (2004). https://doi.org/10.1016/S0169-4332(03)00881-X
79. J. Bonse, G. Bachelier, J. Siegel, J. Solis, Time-and space-resolved dynamics of melting, ablation, and solidification phenomena induced by femtosecond laser pulses in germanium. Phys. Rev. B **74**, 134106 (2006). https://doi.org/10.1103/PhysRevB.74.134106
80. B. Rethfeld, V.V. Temnov, K. Sokolowski-Tinten, S.I. Anisimov, D. von der Linde, Dynamics of ultrashort pulse-laser ablation: equation of state considerations. Proc. SPIE **4760**, 72–80 (2002). https://doi.org/10.1117/12.482055
81. M. Domke, S. Rapp, M. Schmidt, H.P. Huber, Ultra-fast movies of thin-film laser ablation. Appl. Phys. A **109**, 409–420 (2012). https://doi.org/10.1007/s00339-012-7072-6
82. K. Sokolowski-Tinten, W. Ziegler, D. von der Linde, M.P. Siegal, D.L. Overmyer, Short-pulse-laser-induced optical damage and fracto-emission of amorphous, diamond-like carbon films. Appl. Phys. Lett. **86**, 121911 (2005). https://doi.org/10.1063/1.1888037
83. J. Bonse, A. Hertwig, R. Koter, M. Weise, U. Beck, P. Reinstädt, M. Griepentrog, J. Krüger, M. Picquart, E. Haro-Poniatowski, Femtosecond laser pulse irradiation effects on thin hydrogenated amorphous carbon layers. Appl. Phys. A **112**, 9–14 (2013). https://doi.org/10.1007/s00339-012-7170-5
84. Y. Hosokawa, M. Yashiro, T. Asahi, H. Masuhara, T. Kadota, Y. Shirota, Jpn. J. Appl. Phys. **40**, L1116 (2001). https://doi.org/10.1143/JJAP.40.L1116
85. J. Bonse, S.M. Wiggins, J. Solis, T. Lippert, H. Sturm, Femtosecond laser-induced decomposition in triazenepolymer thin films. Appl. Surf. Sci. **248**, 157–162 (2005). https://doi.org/10.1016/j.apsusc.2005.03.021
86. J. Bonse, J. Solis, C. Spielmann, T. Lippert, J. Krüger, Damage mechanisms in polymers upon NIR femtosecond pulse laser irradiation: sub-threshold processes and their implications for laser safety applications. AIP Conf. Proc. **1278**, 56–64 (2010). https://doi.org/10.1063/1.3507148
87. K. Kumar, K.K.C. Lee, J. Li, J. Nogami, N.P. Kherani, P.R. Herman, Quantized structuring of transparent films with femtosecond laser interference. Light: Sci. Appl. **3**, e157 (2014). https://doi.org/10.1038/lsa.2014.38
88. S. Ho, K. Kumar, K.K.C. Lee, J. Li, P.R. Herman, Interferometric femtosecond laser processing for nanostructuring inside thin film. Adv. Opt. Techn. **3**, 499–513 (2014). https://doi.org/10.1515/aot-2014-0047
89. R. Haight, P. Longo, A. Wagner, D. Lim, High resolution material ablation and deposition with femtosecond lasers and applications to photomask repair. J. Mod. Opt. **51**, 2781–2796 (2004). https://doi.org/10.1080/09500340408231837
90. R. Haight, D. Hayden, P. Longo, T. Neary, A. Wagner, Implementation and performance of a femtosecond laser mask repair system in manufacturing. Proc. SPIE **3546**, 477–484 (1998). https://doi.org/10.1117/12.332872
91. K. Lieberman, Y. Shani, I. Melnik, S. Yoffe, Y. Sharon, Near-field optical photomask repair with a femtosecond laser. J. Microsc. **194**, 537–541 (1999). https://doi.org/10.1046/j.1365-2818.1999.00547.x
92. R. Haight, D. Hayden, P. Longo, T. Neary, A. Wagner, MARS: Femtosecond laser mask advanced repair system in manufacturing. J. Vac. Sci. Technol. B **17**, 3137–3143 (1999). https://doi.org/10.1116/1.590968
93. A. Wagner, R. Haight, P. Longo, MARS2: An advanced femtosecond laser mask repair tool. Proc. SPIE **4889**, 457–468 (2002). https://doi.org/10.1117/12.467388
94. R. Haight, P. Longo, A. Wagner, Material processing using femtosecond lasers: repairing patterned photomasks. MRS Bull. **31**, 634–638 (2006). https://doi.org/10.1557/mrs2006.161

95. L. Lazzarini, L. Marchesini, J.F. Asmus, Lasers for cleaning of statuary: Initial results and potentialities. J. Vac. Sci. Technol. **10**, 1039–1043 (1973). https://doi.org/10.1116/1.1318462
96. J.F. Asmus, More light for art conservation. IEEE Circuits Devices Mag. **2**, 6–15 (1986). https://doi.org/10.1109/MCD.1986.6311800
97. J. Schille, L. Schneider, S. Mauersberger, S. Szokup, S. Höhn, J. Pötschke, F. Reiß, E. Leidich, U. Löschner, High-rate laser surface texturing for advanced tribological functionality. Lubricants **8**, 33 (2020). https://doi.org/10.3390/lubricants8030033
98. H.K. Park, C.P. Grigoropoulos, W.P. Leung, A.C. Tam, A practical excimer laser-based cleaning tool for removal of surface contaminants. IEEE Trans. Compon. Packag. Manuf. Technol. Part A **17**, 631–643 (1994). https://doi.org/10.1109/95.335050
99. C.T. Walters, B.E. Campbell, R.J. Hull, Laser cleaning of metal surfaces. Proc. SPIE **3343**, 859 (1998). https://doi.org/10.1117/12.321613
100. L. Urech, T. Lippert, A. Wokaun, S. Martin, H. Mädebach, J. Krüger, Removal of doped poly(methylmetacrylate) from tungsten and titanium substrates by femto- and nanosecond laser cleaning. Appl. Surf. Sci. **252**, 4754–4758 (2006). https://doi.org/10.1016/j.apsusc.2005.07.109
101. N. Maharjan, W. Zhou, H. Zhen, Y. Zhou, N. Wu, Surface cleaning of titanium alloy using femtosecond laser pulses. Lasers Eng. **43**, 223–235 (2019). https://www.oldcitypublishing.com/journals/lie-home/lie-issue-contents/lie-volume-43-number-4-6-2019/lie-43-4-6-p-223-235/
102. A. Tsunemi, A. Endo, D. Ichishima, Paint removal from aluminum and composite substrate of aircraft by laser ablation using TEA CO_2 lasers. Proc. SPIE **3343**, 1018 (1998). https://doi.org/10.1117/12.321539
103. M.K.A.A. Razab, A.M. Noor, M.S. Jaafar, N.H. Abdullah, F.M. Suhaimi, M. Mohamed, N. Adam, N.A.A.N. Yusuf, A review of incorporating Nd:YAG laser cleaning principal in automotive industry. J. Radiat. Res. Appl. Sci. **11**, 393–402 (2018). https://doi.org/10.1016/j.jrras.2018.08.002
104. J.-E. Kim, J.-M. Lee, J.-H. Hyun, J.-H. Jeong, J.-D. Kim, A study on the laser removal of epoxy coatings on SS400 surface by beam scanning patterns. Coatings **11**, 1510 (2021). https://doi.org/10.3390/coatings11121510
105. X. Zhou, K. Imasaki, H. Furukawa, C. Yamanaka, S. Nakai, Experimental study on surface decontamination by laser ablation. J. Laser Appl. **14**, 13–16 (2002). https://doi.org/10.2351/1.1418708
106. T.L. See, Z. Liu, S. Cheetham, S. Dilworth, L. Li, Laser abrading of carbon fibre reinforced composite for improving paint adhesion. Appl. Phys. A **117**, 1045–1054 (2014). https://doi.org/10.1007/s00339-014-8527-8
107. M.I. Cooper, D.C. Emmony, J. Larson, Characterization of laser cleaning of limestone. Opt. Laser Technol. **27**, 69–73 (1995). https://doi.org/10.1016/0030-3992(95)93962-Q
108. K. Liu, E. Garmire, Paint removal using lasers. Appl. Opt. **34**, 4409–4415 (1995). https://doi.org/10.1364/AO.34.004409
109. J. Brand, A. Wain, A.V. Rode, S. Madden, P.L. King, L. Rapp, Femtosecond pulse laser cleaning of spray paint from heritage stone surfaces. Opt. Express **30**, 31122–31135 (2022). https://doi.org/10.1364/OE.468750
110. S. Georgiou, V. Zafiropulos, D. Anglos, C. Balas, V. Tornari, C. Fotakis, Excimer laser restoration of painted artworks: procedures, mechanisms and effects. Appl. Surf. Sci. **127–129**, 738–745 (1998). https://doi.org/10.1016/S0169-4332(97)00734-4
111. W. Kautek, S. Pentzien, P. Rudolph, J. Krüger, E. König, Laser interaction with coated collagen and cellulose fibre composites: fundamentals of laser cleaning of ancient parchment manuscripts and paper. Appl. Surf. Sci. **127–129**, 746–754 (1998). https://doi.org/10.1016/S0169-4332(97)00735-6
112. T.R. Friberg, V. Zafiropulos, M. Kalaitzaki, R. Kowalski, J. Petrakis, C. Fotakis, Excimer laser cleaning of mold-contaminated paper: sterilization and air quality considerations. Laser Med. Sci. **12**, 55–59 (1997). https://doi.org/10.1007/BF02763922
113. J. Kolar, M. Strlič, S. Pentzien, W. Kautek, Near-UV, visible and IR pulsed laser light interaction with cellulose. Appl. Phys. A **71**, 87–90 (2000). https://doi.org/10.1007/PL00021097
114. J. Shepard, C.R.T. Young, D. Parsons-Karavassilis, K. Dowling, A preliminary study into the suitability of femtosecond lasers for the removal of adhesive from canvas paintings. In: *Optics and Lasers in Biomedicine and Culture. Series of the International Society on Optics Within Life Sciences*, ed. by C. Fotakis, T.G. Papazoglou, C. Kalpouzos, Vol. 5 (Springer, Berlin, Heidelberg, 2000), pp. 108 – 114. https://doi.org/10.1007/978-3-642-56965-4_19
115. T. Burmester, M. Meier, H. Haferkamp, S. Barcikowski, J. Bunte, A. Ostendorf, Femtosecond laser cleaning of metallic cultural heritage and antique artworks. Springer Proc. Phys. **100**, 61–69 (2005). https://doi.org/10.1007/3-540-27176-7_8
116. A.V. Rode, D. Freeman, K.G.H. Baldwin, A. Wain, O. Uteza, P. Delaporte, Scanning the laser beam for ultrafast pulse laser cleaning of paint. Appl. Phys. A **93**, 135–129 (2008). https://doi.org/10.1007/s00339-008-4656-2
117. P. Pouli, G. Bounos, S. Georgiou, C. Fotakis, Femtosecond laser cleaning of painted artefacts; is this the way forward? Springer Proc. Phys. **116**, 287–293 (2007). https://doi.org/10.1007/978-3-540-72130-7_33
118. P. Pouli, I.-A. Paun, G. Bounos, S. Georgiou, C. Fotakis, The potential of UV femtosecond laser ablation for varnish removal in the restoration of painted works of art. Appl. Surf. Sci. **254**, 6875–6879 (2008). https://doi.org/10.1016/j.apsusc.2008.04.106
119. S. Gaspard, M. Oujja, P. Moreno, C. Méndez, A. García, C. Domingo, M. Castillejo, Interaction of femtosecond laser pulses with tempera paints. Appl. Surf. Sci. **255**, 2675–2681 (2008). https://doi.org/10.1016/j.apsusc.2008.07.205
120. T. Rivas, A.J. Lopez, A. Ramil, S. Pozo, M.P. Fiorucci, M.E. López de Silanes, A. García, J.R. Vazquez de Aldana, C. Romero, P. Moreno, Comparative study of ornamental granite cleaning using femtosecond and nanosecond pulsed lasers. Appl. Surf. Sci. **278**, 226–233 (2013). https://doi.org/10.1016/j.apsusc.2012.12.038
121. M. Walczak, M. Oujja, L. Crespo-Arcá, A. García, C. Méndez, P. Moreno, C. Domingo, M. Castillejo, Evaluation of femtosecond laser pulse irradiation of ancient parchment. Appl. Surf. Sci. **255**, 3179–3183 (2008). https://doi.org/10.1016/j.apsusc.2008.09.011
122. S. Pentzien, A. Conradi, R. Koter, J. Krüger, Cleaning of artificially soiled paper using nanosecond, picosecond and femtosecond laser pulses. Appl. Phys. A **101**, 441–446 (2010). https://doi.org/10.1007/s00339-010-5809-7
123. T. Ersoy, T. Tunay, M. Uğuryol, G. Mavili, S. Akturk, Femtosecond laser cleaning of historical paper with sizing. J. Cult. Herit. **15**, 258–265 (2014). https://doi.org/10.1016/j.culher.2013.07.002
124. B.A. Schmidt, S. Pentzien, A. Conradi, J. Krüger, Femtosecond and nanosecond laser decontaminations of biocidal-loaded wooden artworks. Appl. Phys. A **123**, 696 (2017). https://doi.org/10.1007/s00339-017-1316-4
125. M. Strlič, J. Kolar, V.-S. Šelih, M. Marinček, Surface modification during Nd:YAG (1064 nm) pulsed laser cleaning of organic fibrous materials. Appl. Surf. Sci. **207**, 236–245 (2003). https://doi.org/10.1016/S0169-4332(02)01371-5
126. P. Pouli, M. Oujja, M. Castillejo, Practical issues in laser cleaning of stone and painted artefacts: optimisation procedures and side effects. Appl. Phys. A **106**, 447–464 (2012). https://doi.org/10.1007/s00339-011-6696-2
127. S. Siano, J. Agresti, I. Cacciari, D. Ciofini, M. Mascalchi, I. Osticioli, A.A. Mencaglia, Laser cleaning in conservation of stone,

metal, and painted artifacts: state of the art and new insights on the use of the Nd:YAG lasers. Appl. Phys. A **106**, 419–446 (2012). https://doi.org/10.1007/s00339-011-6690-8
128. J. Krüger, S. Pentzien, K. von Lerber, Determination of a working range for the laser cleaning of soiled silk. Springer Proc. Phys. **116**, 321–327 (2007). https://doi.org/10.1007/978-3-540-72310-7_37
129. T. Harada, S. Spence, A. Margiolakis, S. Deckoff-Jones, R. Ploeger, A.N. Shugar, J.F. Hamm, K.M. Dani, A.R. Dani, Obtaining cross-sections of paint layers in cultural artifacts using femtosecond pulsed lasers. Materials **10**, 107 (2017). https://doi.org/10.3390/ma10020107
130. Y. Nakai, K. Hattori, A. Okano, N. Itoh, R.F. Haglund Jr., Non-thermal laser sputtering from solid surfaces. Nucl. Instrum. Methods Phys. Res. Sect. B **58**, 452–462 (1991). https://doi.org/10.1016/0168-583X(91)95885-H
131. K. König, A. Ostendorf (Eds.), Special Issue: generation of sub-100 nm structures by nonlinear laser-material interaction. J. Laser Appl., Vol. **24**, Issue 4 (2022) https://lia.scitation.org/toc/jla/24/4
132. N. Hartmann, Nonlinear processing and multiphoton ablation of self-assembled monolayers for application as ultrathin resists and in biochemical sensors. Chapter 6 in *Optically Induced Nanostructures: Biomedical and Technical Applications* ed. by K. König, A. Ostendorf (De Gruyter, Berlin, 2015), pp. 117–139
133. N. Hartmann, Sub-Wavelength Patterning of Self-Assembled Organic Monolayers via Nonlinear Processing with Femtosecond Laser Pulses. Chapter 27 in *Coherence and Ultrashort Laser Emission* ed. by F.J. Duarte (IntechOpen, London, 2010), pp. 629–644 https://doi.org/10.5772/13050
134. S. Franzka, J. Koch, B.N. Chichkov, N. Hartmann, Nonlinear femtosecond laser processing of alkylsiloxane monolayers on surface-oxidized silicon substrates. J. Vac. Sci. Technol. A **28**, 814–817 (2010). https://doi.org/10.1116/1.3281296
135. A. Hervy, L. Gallais, G. Chériaux, D. Mouricaud, Femtosecond laser-induced damage threshold of electron beam deposited dielectrics for 1-m class optics. Opt. Eng. **56**, 011001 (2016). https://doi.org/10.1117/1.OE.56.1.011001
136. C.N. Danson, C. Haefner, J. Bromage, T. Butcher et al., Petawatt and exawatt class lasers worldwide. High Power Laser Sci. Eng. **7**, e54 (2019). https://doi.org/10.1017/hpl.2019.36
137. Lasers and laser-related equipment-determination of laser-induced damage threshold of optical surfaces — Part 1: 1-on-1 test. International Organization for Standardization, Geneva, Switzerland (2000)
138. Lasers and laser-related equipment-determination of laser-induced damage threshold of optical surfaces — Part 2: S-on-1 test. International Organization for Standardization, Geneva, Switzerland (2001)
139. Lasers and laser-related equipment – Test methods for laser-induced damage threshold – Part 1: Definitions and general principles (ISO 21254-1:2011), International Organization for Standardization, Geneva, Switzerland (2011)
140. Lasers and laser-related equipment – Test methods for laser-induced damage threshold – Part 2: Threshold determination (ISO 21254–2:2011), International Organization for Standardization, Geneva, Switzerland (2011)
141. M. Jupé, D. Ristau, Coatings for fs lasers. Chapter 15 in: D. Ristau (Ed.), *Laser-induced Damage in Optical Materials*, 1st edn. (CRC Press/Taylor & Francis Group, Boca Raton, 2015) https://doi.org/10.1201/b17722
142. M. Jupe, M. Lappschies, L. Jensen, K. Starke, D. Ristau, A. Melninkaitis, V. Sirutkaitis, I. Cravetchi, W. Rudolph, Mixed oxide coatings for advanced fs-laser applications. Proc. SPIE **6720**, 67200U (2008). https://doi.org/10.1117/12.753730
143. J. Bohandy, S.F. Kim, F.J. Adrian, Metal deposition from a supported metal film using an excimer laser. J. Appl. Phys. **60**, 1538–1539 (1986). https://doi.org/10.1063/1.337287
144. J. Bohandy, S.F. Kim, F.J. Adrian, A.N. Jette, Metal deposition at 532 nm using a laser transfer technique. J. Appl. Phys. **63**, 1158–1162 (1988). https://doi.org/10.1063/1.340023
145. V. Schultze, M. Wagner, Laser-induced forward transfer of aluminium. Appl. Surf. Sci. **52**, 303–309 (1991). https://doi.org/10.1016/0169-4332(91)90072-R
146. Z. Kántor, Z. Tóth, T. Szörényi, Laser induced forward transfer: the effect of support-film interface and film-to-substrate distance on transfer. Appl. Phys. A **54**, 170–175 (1992). https://doi.org/10.1007/BF00323905
147. I. Zergioti, S. Mailis, N.A. Vainos, P. Papakonstantinou, C. Kalpouzos, C. Grigoropoulous, C. Fotakis, Microdeposition of metal and oxide structures using ultrashort laser pulses. Appl. Phys. A **66**, 579–582 (1998). https://doi.org/10.1007/s003390050717
148. D.P. Banks, C. Grivas, I. Zergioti, R.W. Eason, Ballistic laser-assisted solid transfer (BLAST) from a thin film precursor. Opt. Express **16**, 3249–3254 (2008). https://doi.org/10.1364/OE.16.003249
149. R.J. Baseman, N.M. Froberg, J.C. Andreshak, Z. Schlesinger, Minimum fluence for laser blow-off of thin gold films at 248 and 532 nm. Appl. Phys. Lett. **56**, 1412–1414 (1990). https://doi.org/10.1063/1.102484
150. T. Sano, H. Yamada, T. Nakayama, I. Miyamoto, Experimental investigation of laser induced forward transfer process of metal thin films. Appl. Surf. Sci. **186**, 221–226 (2002). https://doi.org/10.1016/S0169-4332(01)00765-6
151. P. Papakonstantinou, N.A. Vainos, C. Fotakis, Microfabrication by UV femtosecond laser ablation of Pt, Cr and indium oxide thin films. Appl. Surf. Sci. **151**, 159–170 (1999). https://doi.org/10.1016/S0169-4332(99)00299-8
152. Z. Kántor, Z. Tóth, T. Szörényi, A.L. Tóth, Deposition of micrometer-sized tungsten patterns by laser transfer technique. Appl. Phys. Lett. **64**, 3506–3508 (1994). https://doi.org/10.1063/1.111255
153. P. Mogyorósi, T. Szörényi, K. Bali, Z. Tóth, I. Hevesi, Pulsed laser ablative deposition of thin metal films. Appl. Surf. Sci. **36**, 157–163 (1989). https://doi.org/10.1016/0169-4332(89)90909-4
154. M. Springer, J. Düsing, J. Koch, P. Jäschke, S. Kaierle, L. Overmeyer, Laser-induced forward transfer as a potential alternative to pick-and-place technology when assembling semiconductor components. J. Laser Appl. **33**, 042030 (2021). https://doi.org/10.2351/7.0000525
155. J.A. Greer, T.E. Parker, Excimer beam applications—Laser-induced forward transfer of metal oxides to trim the frequency of surface acoustic wave resonator devices. Proc. SPIE **998**, 113 (1988). https://doi.org/10.1117/12.960218
156. I. Zergioti, D.G. Papazoglu, A. Karaiskou, N.A. Vainos, C. Fotakis, Laser microprinting of InO_x active optical structures and time resolved imaging of the transfer process. Appl. Surf. Sci. **197–198**, 868–872 (2002). https://doi.org/10.1016/S0169-4332(02)00440-3
157. S. Chakraborty, H. Sakata, E. Yokoyama, M. Wakaki, D. Chakravorty, Laser-induced forward transfer technique for maskless patterning of amorphous V_2O_5 thin film. Appl. Surf. Sci. **254**, 638–643 (2007). https://doi.org/10.1016/j.apsusc.2007.06.066
158. A. Klini, A. Mourka, V. Dinca, C. Fotakis, F. Claeyssens, ZnO nanorod micropatterning via laser-induced forward transfer. Appl. Phys. A **87**, 17–22 (2007). https://doi.org/10.1007/s00339-006-3811-x
159. E. Fogarassy, C. Fuchs, F. Kerherve, G. Hauchecorne, J. Perrière, Laser-induced forward transfer: A new approach for the

deposition of high T_c superconducting thin films. J. Mater. Res. **4**, 1082–1086 (1989). https://doi.org/10.1557/JMR.1989.1082
160. P. Delaporte, A. Ainsebaa, A.-P. Alloncle, M. Benetti, C. Boutopoulos, D. Cannata, F. Di Pietrantonio, V. Dinca, M. Dinescu, J. Dutroncy, R. Eason, M. Feinäugle, J.-M. Fernandez-Pradas, A. Grisel, K. Kaur, U. Lehmann, T. Lippert, C. Loussert, M. Makrygianni, I. Manfredonia, T. Mattle, J.-L. Morenza, M. Nagel, F. Nüesch, A. Palla-Papavlu, L. Rapp, N. Rizvi, G. Rodio, S. Sanaur, P. Serra, J. Shaw-Stewart, C.L. Sones, E. Verona, I. Zergioti, Applications of laser printing for organic electronics. Proc. SPIE **8607**, 86070Z (2013). https://doi.org/10.1117/12.2004062
161. L. Rapp, C. Constantinescu, Y. Larmande, A.K. Diallo, C. Videlot-Ackermann, P. Delaporte, A.P. Alloncle, Functional multilayered capacitor pixels printed by picosecond laser-induced forward transfer using a smart beam shaping technique. Sens. Actuators A **224**, 111–118 (2015). https://doi.org/10.1016/j.sna.2015.01.020
162. J.R.H. Shaw-Stewart, T. Mattle, T.K. Lippert, M. Nagel, F.A. Nüesch, A. Wokaun, The fabrication of small molecule organic light-emitting diode pixels by laser-induced forward transfer. J. Appl. Phys. **113**, 043104 (2013). https://doi.org/10.1063/1.4788710
163. B. Hopp, T. Smausz, N. Kresz, N. Barna, Z. Bor, L. Kolozsvári, D.B. Chrisey, A. Szabó, A. Nógrádi, Survival and proliferative ability of various living cell types after laser-induced forward transfer. Tissue Eng. **11**, 1817–1823 (2005). https://doi.org/10.1089/ten.2005.11.1817
164. A. Doraiswamy, R.J. Narayan, T. Lippert, L. Urech, A. Wokaun, M. Nagel, B. Hopp, M. Dinescu, R. Modi, R.C.Y. Auyeung, D.B. Chrisey, Excimer laser forward transfer of mammalian cells using a novel triazene absorbing layer. Appl. Surf. Sci. **252**, 4743–4747 (2006). https://doi.org/10.1016/j.apsusc.2005.07.166
165. A. Karaiskou, I. Zergioti, C. Fotakis, M. Kapsetaki, D. Kafetzopoulos, Microfabrication of biomaterials by the sub-ps laser-induced forward transfer process. Appl. Surf. Sci. **208–209**, 245–249 (2003). https://doi.org/10.1016/S0169-4332(02)01396-X
166. P. Serra, M. Colina, J.M. Fernandez-Paras, L. Sevilla, J.L. Morenza, Preparation of functional DNA microarrays through laser-induced forward transfer. Appl. Phys. Lett. **85**, 1639–1641 (2004). https://doi.org/10.1063/1.1787614
167. I. Zergioti, A. Karaiskou, D.G. Papazoglou, C. Fotakis, M. Kapsetaki, D. Kafetzopoulos, Femtosecond laser microprinting of biomaterials. Appl. Phys. Lett. **86**, 163902 (2005). https://doi.org/10.1063/1.1906325
168. V. Dinca, A. Ranella, M. Farsari, D. Kafetzopoulous, M. Dinescu, A. Popescu, C. Fotakis, Quantification of the activity of biomolecules in microarrays obtained by direct laser transfer. Biomed. Microdevices **10**, 719–725 (2008). https://doi.org/10.1007/s10544-008-9183-6
169. R. Bähnisch, W. Groß, A. Menschig, Single-shot, high repetition rate metallic pattern transfer. Microelectron. Eng. **50**, 541–546 (2000). https://doi.org/10.1016/S0167-9317(99)00325-1
170. P. Serra, J.M. Fernandez-Pradaz, M. Colina, M. Duocastella, J. Dominguez, J.L. Morenza, Laser-induced forward transfer: a direct-writing technique for biosensors preparation. J. Laser Micro Nanoeng. **1**, 236–242 (2006). https://doi.org/10.2961/jlmn.2006.03.0017
171. C.B. Arnold, P. Serra, A. Piqué, Laser direct-write techniques for printing of complex materials. MRS Bull. **32**, 23–31 (2007). https://doi.org/10.1557/mrs2007.11
172. M. Nagel, T. Lippert, Laser-induced forward transfer for the fabrication of devices, in *Nanomaterials; processing and characterization with lasers*, ed. by H. Zeng, C. Guo, W. Cai, S.C. Singh (Wiley, Weinheim, 2012), pp. 255 – 316 https://doi.org/10.1002/9783527646821.ch5
173. P. Delaporte, A.-P. Alloncle, Laser-induced forward transfer: A high resolution additive manufacturing technology. Opt. Laser Technol. **78**, 33–41 (2016). https://doi.org/10.1016/j.optlastec.2015.09.022
174. P. Serra, A. Piqué, Laser-induced forward transfer: Fundamentals and applications. Adv. Mater. Technol. **4**, 1800099 (2019). https://doi.org/10.1002/admt.201800099
175. A. Piqué, K.M. Charipar, Laser-induced forward transfer applications in micro-engineering, in *Handbook of Laser Micro- and Nano-Engineering*, ed. by K. Sugioka (Springer, Cham, 2021), pp. 1325 – 1359 https://doi.org/10.1007/978-3-030-63647-0_26
176. M. Paire, A. Shams, L. Lombez, N. Péré-Laperne, S. Collin, J.-L. Pelouard, J.-F. Guillemoles, D. Lincot, Resistive and thermal scale effects for Cu(In, Ga)Se_2 polycrystalline thin film microcells under concentration. Energy Environ. Sci. **4**, 4972–4977 (2011). https://doi.org/10.1039/C1EE01661J
177. S. Andree, B. Heidmann, F. Ringleb, K. Eylers, J. Bonse, T. Boeck, M. Schmid, J. Krüger, Femtosecond laser pulses for photovoltaic bottom-up strategies. 10. Mittweidaer Lasertagung, 16.-17. November 2017, Scientific Reports No. 2, 1–4 (2017)
178. F. Ringleb, K. Eylers, T. Teubner, T. Boeck, C. Symietz, J. Bonse, S. Andree, J. Krüger, B. Heidmann, M. Schmid, M. Lux-Steiner, Regularly arranged indium islands on glass/molybdenum substrates upon femtosecond laser and physical vapor deposition processing. Appl. Phys. Lett. **108**, 111904 (2016). https://doi.org/10.1063/1.4943794
179. F. Ringleb, K. Eylers, T. Teubner, H.-P. Schramm, C. Symietz, J. Bonse, S. Andree, B. Heidmann, M. Schmid, J. Krüger, T. Boeck, Growth and shape of indium islands on molybdenum at micro-roughened spots created by femtosecond laser pulses. Appl. Surf. Sci. **418**, 548–553 (2017). https://doi.org/10.1016/j.apsusc.2016.11.135
180. S. Andree, B. Heidmann, F. Ringleb, K. Eylers, J. Bonse, T. Boeck, M. Schmid, J. Krüger, Production of precursors for micro-concentrator solar cells by femtosecond laser-induced forward transfer. Appl. Phys. A **123**, 670 (2017). https://doi.org/10.1007/s00339-017-1282-x
181. M. Schmid, B. Heidmann, F. Ringleb, K. Eylers, O. Ernst, S. Andree, J. Bonse, T. Boeck, J. Krüger, Locally grown Cu(In, Ga)Se_2 micro islands for concentrator solar cells. Proc. SPIE **10527**, 1052707 (2018). https://doi.org/10.1117/12.2288253
182. B. Heidmann, S. Andree, S. Levcenko, T. Unold, D. Abou-Ras, N. Schäfer, J. Bonse, J. Krüger, M. Schmid, Fabrication of regularly arranged chalcopyrite micro solar cells via femtosecond laser-induced forward transfer for concentrator application. ACS Appl. Energy Mater. **1**, 27–31 (2018). https://doi.org/10.1021/acsaem.7b00028
183. F. Ringleb, S. Andree, B. Heidmann, J. Bonse, K. Eylers, O. Ernst, T. Boeck, M. Schmid, J. Krüger, Femtosecond laser-assisted fabrication of chalcopyrite micro-concentrator photovoltaics. Beilstein J. Nanotechn. **9**, 3025–3038 (2018). https://doi.org/10.3762/bjnano.9.281
184. F. Brech, L. Cross, Optical microemission stimulated by a ruby maser. Appl. Spectrosc. **16**, 59–63 (1962).
185. R.E. Russo, X. Mao, H. Liu, J. Gonzalez, S.S. Mao, Laser ablation in analytical chemistry—a review. Talanta **57**, 425–451 (2002). https://doi.org/10.1016/s0039-9140(02)00053-x
186. R. Hergenröder, O. Samek, V. Hommes, Femtosecond laser ablation elemental mass spectrometry. Mass Spectrom. Rev. **25**, 551–572 (2006). https://doi.org/10.1002/mas.20077
187. R.E. Russo, T.W. Suen, A.A. Bol'shakov, J. Yoo, O. Sorkhabi, X. Mao, J. Gonzalez, D. Oropeza, V. Zorba, Laser plasma spectrochemistry. J. Anal. At. Spectrom. **26**, 1596 (2011). https://doi.org/10.1039/C1JA10107B
188. M. Tulej, N.F.W. Ligterink, C. de Koning, V. Grimaudo, R. Lukmanov, P. Keresztes Schmidt, A. Riedo, P. Wurz, Current

progress in femtosecond laser ablation/ionisation time-of-flight mass spectrometry. Appl. Sci. **11**, 2562 (2021). https://doi.org/10.3390/app11062562
189. S.S. Harilal, M.C. Phillips, D.H. Froula, K.K. Anoop, R.C. Issac, F. N. Beg, Optical diagnostics of laser-produced plasmas. Rev. Mod. Phys. **94**, 035002 (2022). https://doi.org/10.1103/RevModPhys.94.035002
190. V. Margetic, K. Niemax, R. Hergenröder, Application of femtosecond laser ablation time-of-flight mass spectrometry to in-depth multilayer analysis. Anal. Chem. **75**, 3103–3107 (2003). https://doi.org/10.1021/ac020791i
191. J. Pisonero, D. Günther, Femtosecond laser ablation inductively coupled plasma mass spectrometry: fundamentals and capabilities for depth profiling analysis. Mass Spectrom. Rev. **27**, 609–623 (2008). https://doi.org/10.1002/mas.20180
192. J. Bonse, J. Krüger, S. Höhm, A. Rosenfeld, Femtosecond laser-induced periodic surface structures. J. Laser Appl. **24**, 042006 (2012). https://doi.org/10.2351/1.4712658
193. E.L. Gurevich, R. Hergenröder, Femtosecond laser-induced breakdown spectroscopy: Physics, applications, and perspectives. Appl. Spectrosc. **61**, 233A–242A (2007). https://opg.optica.org/as/abstract.cfm?uri=as-61-10-233A
194. T.A. Labutin, V.N. Lednev, A.A. Ilyin, A.M. Popov, Femtosecond laser-induced breakdown spectroscopy. J. Anal. At. Spectrom. **31**, 90–118 (2016). https://doi.org/10.1039/C5JA00301F
195. V. Margetic, A. Pakulev, A. Stockhaus, M. Bolshov, K. Niemax, R. Hergenröder, A comparison of nanosecond and femtosecond laser-induced plasma spectroscopy of brass samples. Spectrochim. Acta B **55**, 1771–1785 (2000). https://doi.org/10.1016/S0584-8547(00)00275-5
196. V. Margetic, K. Niemax, R. Hergenröder, A study of non-linear calibration graphs for brass with femtosecond laser-induced breakdown spectroscopy. Spectrochim. Acta B **56**, 1003–1010 (2001). https://doi.org/10.1016/S0584-8547(01)00189-6
197. V. Margetic, M. Bolshov, A. Stockhaus, K. Niemax, R. Hergenröder, Depth profiling of multi-layer samples using femtosecond laser ablation. J. Anal. At. Spectrom. **16**, 616–621 (2001). https://doi.org/10.1039/B100016K
198. S.M. Angel, D.N. Stratis, K.L. Eland, T. Lai, M.A. Berg, D.M. Gold, LIBS using dual- and ultra-short laser pulses. Fresenius J. Anal. Chem. **369**, 320–327 (2001). https://doi.org/10.1007/s002160000656
199. B. Le Drogoff, J. Margot, M. Chaker, M. Sabsabi, O. Barthel'emy, T.W. Johnston, S. Laville, F. Vidal, Y. von Kaenel, Temporal characterization of femtosecond laser pulses induced plasma for spectrochemical analysis of aluminum alloys. Spectrochim. Acta B **56**, 987–1002 (2001). https://doi.org/10.1016/S0584-8547(01)00187-2
200. J. Scaffidi, J. Pender, W. Pearman, S.R. Goode, B.W. Colston, J.C. Carter, S.M. Angel, Dual-pulse laser-induced breakdown spectroscopy with combinations of femtosecond and nanosecond laser pulses. Appl. Opt. **42**, 6099–6106 (2003). https://doi.org/10.1364/AO.42.006099
201. R. Wechsung, F. Hillenkamp, R. Kaufmann, R. Nitsche, H. Vogt, Laser-microprobe-mass-analyzer LAMMA—new analysis method for research and technology. Mikroskopie **34**, 47–54 (1978).
202. Y. Cui, J.F. Moore, S. Milasinovic, Y.M. Liu, R.J. Gordon, L. Hanley, Depth profiling and imaging capabilities of an ultrashort pulse laser ablation time of flight mass spectrometer. Rev. Sci. Instrum. **83**, 093702 (2012). https://doi.org/10.1063/1.4750974
203. V. Grimaudo, M. Tulej, A. Riedo, R. Lukmanov, N.F. Ligterink, C. De Koning, P. Wurz, UV post-ionization laser ablation ionization mass spectrometry for improved nm-depth profiling resolution on Cr/Ni reference standard. Rapid Commun. Mass Spectrom. **34**, e8803 (2020). https://doi.org/10.1002/rcm.8803
204. R.E. Russo, X. Mao, J.J. Gonzalez, S.S. Mao, Femtosecond laser ablation ICP-MS. J. Anal. At. Spectrom. **17**, 1072–1075 (2002). https://doi.org/10.1039/B202044K
205. F. Poitrasson, F.-X. D'Abzac, Femtosecond laser ablation inductively coupled plasma source mass spectrometry for elemental and isotopic analysis: Are ultrafast lasers worthwhile? J. Anal. At. Spectrom. **32**, 1075–1091 (2017). https://doi.org/10.1039/C7JA00084G
206. F. Poitrasson, X. Mao, S.S. Mao, R. Freydier, R.E. Russo, Comparison of ultraviolet femtosecond and nanosecond laser ablation inductively coupled plasma mass spectrometry analysis in glass, monazite, and zircon. Anal. Chem. **75**, 6184–6190 (2003). https://doi.org/10.1021/ac034680a
207. D. Käser, L. Hendriks, J. Koch, D. Günther, Depth profile analyses with sub 100-nm depth resolution of a metal thin film by femtosecond—laser ablation—inductively coupled plasma—time-of-flight mass spectrometry. Spectrochim. Acta Part B **149**, 176–183 (2018). https://doi.org/10.1016/j.sab.2018.08.002
208. I. Horn, F. von Blanckenburg, Investigation on elemental and isotopic fractionation during 196 nm femtosecond laser ablation multiple collector inductively coupled plasma mass spectrometry. Spectrochim. Acta Part B **62**, 410–422 (2007). https://doi.org/10.1016/j.sab.2007.03.034